UNIVERSITY OF SOUTHAMPTON

Domain Transformations for Optical Telecommunications Signals

by

Trina Tsao-Tin Ng

A thesis submitted for the degree of Doctor of Philosophy

in the
FACULTY OF ENGINEERING, SCIENCE AND MATHEMATICS
Optoelectronics Research Centre

February 2010

UNIVERSITY OF SOUTHAMPTON

ABSTRACT

FACULTY OF ENGINEERING, SCIENCE AND MATHEMATICS
OPTOELECTRONICS RESEARCH CENTRE

Doctor of Philosophy

Domain Transformations for Optical Telecommunications Signals

by Trina Tsao-Tin Ng

In this thesis, the transformation of optical telecommunication signal waveforms between the temporal and spectral domains is investigated. Temporal optical Fourier transformations (TOFTs) are presented with the primary aim of mitigating distortions in high repetition rate telecommunication signals, by transferring them from the temporal domain into the frequency domain. Development of TOFT is extended to aid their suitability for other applications also.

The TOFT is based on inducing cross-phase modulation on the signal to be transformed, using shaped parabolic pulses as the pump. To demonstrate the technique, various methods of generating parabolic pulses are investigated and considered for their suitability for TOFTs. Firstly, parabolic pulses are generated in a nonlinear fashion exploiting their natural evolution in a normally dispersive fibre. Compensation is performed on timing jitter signals using this method. In another configuration, parabolic pulses are generated with a superstructured fibre Bragg grating. The passive nature and the chirp free parabolics generated by the grating enabled greater flexibility in the experimental parameters thus improving the fidelity of the TOFT. Compensation of pulses distorted by second and third order dispersion is demonstrated.

Unexpected results in the first two TOFT experiments led to further analysis and the derivation of the conditions for a complete TOFT. Sophisticated reconfigurable filters are used to convert an optical frequency comb (OFC) into one or more simultaneous pulse sources, each with a configurable shape and phase profile. Pulses generated using the OFC and reconfigurable filter are used to experimentally verify the new theory.

The thesis also includes a presentation of a linear frequency resolved optical gating technique. The versatility of the technique was demonstrated through the characterisation of many of the pulses generated in this thesis, providing insight to their time-frequency domain relationships.

Contents

List of Figures

List of Tables

Declaration of Authorship

I, Trina Tsao-Tin Ng

declare that the thesis entitled:

Domain Transformations for Telecommunications Applications

and the work presented in the thesis are both my own, and have been generated by me as the result of my own original research. I confirm that:

- this work was done wholly or mainly while in candidature for a research degree at this University;
- where any part of this thesis has previously been submitted for a degree or any other qualification at this University or any other institution, this has been clearly stated;
- where I have consulted the published work of others, this is always clearly attributed;
- where I have quoted from the work of others, the source is always given. With the exception of such quotations, this thesis is entirely my own work;
- I have acknowledged all main sources of help;
- where the thesis is based on work done by myself jointly with others, I have made clear exactly what was done by others and what I have contributed myself;
- parts of this work have been published as: [See *List of Publications*].

Trina Tsao-Tin Ng February 2010

Abbreviations

CW	Continuous wave
DCF	Dispersion compensating fibre
DFB	Distributed feedback
DFG	Difference frequency generation
DPSK	Differential phase-shift keying
EAM	Electroabsorption modulator
EDFA	Erbium doped fibre amplifier
EOM	Electro-optic modulator
FBG	Fibre Bragg grating
FP-EOM	Fabry-Perot electro-optic modulator
FROG	Frequency resolved optical gating
FWHM	Full width at half maximum
FWM	four wave mixing
GSL	Gain switched laser
GVD	Group velocity dispersion
HNLF	Highly nonlinear fibre
LCoS	Liquid crystal on silicon
L-FROG	Linear frequency resolved gating technique
MLL	Mode locked laser
MZI	Mach-Zehnder interferometer
MZM	Mach-Zender modulator
NOLM	Nonlinear optical loop mirror
O-E-O	Optical electrical optical
OFC	Optical frequency comb
OFCG	Optical frequency comb generator
OMUX	Optical multiplexer

OSA	Optical spectrum analyzer
OTDM	Optical time division multiplexing
PMD	Polarization mode dispersion
PRBS	Pseudo-random bit sequence
RZ	Return to zero
SFG	Sum frequency generation
SHG	Second harmonic generation
SMF	Single mode fibre
SPIDER	Spectral phase interferometry for direct electric-field reconstruction
SPM	Self-phase modulation
SOA	Semiconductor optical amplifiers
SSFBG	Superstructured fibre Bragg grating
TOD	Third order dispersion
TOFT	Temporal optical Fourier transform
WDM	Wavelength division multiplexing
XGM	Cross-gain modulation
XPM	Cross-phase modulation

Acknowledgements

It's been a long journey, but one which has taught me something every step of the way. Although I am deeply grateful to all the people who have helped and accompanied me along the way, I will probably never be able to thank some of them enough.

First and foremost, I want to thank my supervisors Dr. Periklis Petropoulos and Prof. David Richardson. Thank you Periklis for having been there throughout offering me guidance, encouragement, a lot of patience and sometimes to firmly prod me into action. Although I have seen Dave sparingly in these years, he has always found time to talk to me when I knocked on his door and discussions with him have always been insightful and frequently inspiring.

The other person who has had the greatest influence on my PhD is my friend, colleague and mentor Francesca Parmigiani. For all the lab know-how and assistance, the honest opinions, the questions I was too scared to ask other people and the wealth of general advice she gave me, I thank her a thousand times over.

I also want to thank to Dr. Morten Ibsen who made the gratings for me, and the many people who have shared their knowledge, wisdom and sometimes equipment with me. These include but not limited to Dr. Neil Broderick, Dr. Radan Slavik, Dr. Andrew Ellis, Dr. James Gates, Dr. Cesar Jauregui, Dr. Michaël Roelens and Dr. Symeon Asimakis. Thanks also to Eve Smith, Tanya Morrow, Kevin Sumner and Marta Betran for all their administrative help and for helping me to stay in the country and stay fed.

However it hasn't all been about work. A huge thanks to Angela Camerlingo, Laura Lagonigro, Adriana Salgado, Christian Vollmert, Hazel Hung, James Bateman, Dave Banks, the "lunch crowd" and all the other friends I have made here. You've kept me going in the hard times and made the journey so much fun that I actually miss Southampton!

Finally, I would like to thank Joel Thakker for all the love and support he has given me and all the patience it must be taking to put up with me as I tie up the last of my student days (maybe!).

“Experience is a grindstone;
and it is lucky for us, if we can get brightened by it,
and not ground”

- Josh Billings -

To my Mum and Dad

Chapter 1

Introduction

Optical networks have revolutionized modern communications enabling massive amounts of data to be rapidly transmitted around the globe. As demand has increased, so has the transmission capacity of optical networks bringing “commercial” data rates from 2.5 Gb/s to 40 Gb/s in just 6 years [1]. This has largely been possible due to the development of low loss silica fibres [2], the Erbium doped fibre amplifier (EDFA) [3] and wavelength division multiplexing (WDM) [4]. EDFA’s provide effective and cheap amplification, which coupled with low loss fibres increases the distance that optical signals can be transmitted without regeneration, thus making optical transmission economical. Meanwhile, WDM has greatly increased the carrying capacity of optical networks by spectrally multiplexing together temporally encoded light and thus using more of the available bandwidth. However to facilitate this push for higher capacity, it is not enough to just maximise bandwidth, one also has to manage it. Increasing the signal repetition rate for telecommunications systems necessarily reduces the degredation which can be tolerated in the data. Thus to maintain signal quality, strict control of optical signal propagation and evolution during transmission is becoming ever more important.

To efficiently manage these high repetition rate signals, signal processing and regeneration has been extensively researched through many approaches. Traditionally it has been optical-electronic-optical (O-E-O) techniques, where the optical signal is detected, processed electronically and then retransmitted, which have been preferred for their lower cost. Being able to process a signal electronically comes with all the benefits of using a mature technology, such as the ability to perform sophisticated processes in small, mass producible modules which ultimately makes signal processors cheaper. However, there is an intrinsic impracticality with using electronics to process optical signals. Optical bandwidths far exceed those available from electronics meaning that bandwidth optimising transmission techniques such as WDM and optical time division multiplexing (OTDM) must constantly be multiplexed and demultiplexed to enable O-E-O to take place. Indeed, although current O-E-O regenerators (or repeaters) are able to perform 40 Gb/s retiming and reshaping electronically and use forward-error-correction to improve performance [5], the increased cost of requiring 40 Gb/s detectors, electronics and modulator components render these modules uneconomical when compared to their 10 Gb/s predecessors [6]. Consequently, state-of-the-art repeater technology are increasing incorporating more optics [7].

Alternatively, all-optical signal processing techniques [8–15] eliminate the need for O-E-O and offer the possibility of high repetition rate, multi-wavelength regeneration without the need to demultiplex signals. If all-optical processing could be developed, it could become more economical to install just a small number of optical regenerators over numerous electronic ones. As optical capacities increase, it is essential that corresponding all-optical technologies are developed to meet this eventuality.

Among the various functions required to effectively process communication signals, the capability to transform a signal from one form to another can beneficially be employed in several applications. Fourier transforms are routinely used throughout the sciences, from mathematics and physics to their multitude of applications within engineering and even economics. Fourier transforms provide gateways between linked domains (eg. frequency-time, frequency-space) giving a new perspective though which to consider any given pattern of behaviour. Knowledge of a signal's phase profile is thus important in linking the intensity profiles of different domains. The reverse is also true. Knowing about the temporal and spectral intensity of a signal we can deduce the phase relationships in the signal. In electronics, the phase of a signal is easily detected and performs an important part in the processing of electrical signals. But despite the example set by electronic processing, optical signal processing has until recently often neglected to use phase information. The reason for this is that the much shorter wavelengths of optical signals make direct phase detection incredibly difficult. Instead, techniques have been developed to exploit the phase link between the temporal and spectral domains to deduce signal phases. The frequency resolved optical gating (FROG) technique of pulse characterization is probably the most widely used of these techniques [16]. By measuring optical signals in multiple domains, it can provide a complete picture of a signal's characteristics and thus lend information not only to the current state of the measured pulse but also to how it will evolve in propagation.

But Fourier transforms can have a greater role in signal processing than just in pulse characterization. Linked domains means that functions which are too difficult to carry out in one domain can often be applied in another to achieve a desired effect. Spectral noise filtering and spectral pulse shaping are prime examples of this [17]. Further, the ability to *move* data between domains would present a gateway to achieving a whole host of new signal processing functions that exploit these relationships.

In recent years, M. Nakazawa *et al.* have proposed and demonstrated the use of time-domain optical Fourier transformations as a method of signal regeneration in itself. Nakazawa's device is based on the premise that many distortions frequently suffered by telecommunications signals such as dispersion, timing jitter and polarisation mode dispersion, do not effect the signal's spectral envelope. By performing a Fourier transform on the signal, this un-distorted spectral envelope is transferred into the temporal domain thus replacing the distorted temporal pulse with a clean one. Temporal optical Fourier transforms (TOFT) have since attracted a lot of attention for their ability to simultaneously mitigate multiple distortions in signals without prior knowledge of the distortion suffered. The technique however, does not come without its own drawbacks which (among others to be discussed later in the thesis) includes the limited time window over which it can operate. Although some of these drawbacks are intrinsic to the TOFT concept, others can be potentially alleviated through better understanding of TOFTs and improved experimental implementation.

The work described in this thesis focuses on the transformation of optical signals between the temporal and spectral domains. It is primarily motivated by Nakazawa's TOFT-based distortion compensator, but in the course of developing it, expanded to consider the time-frequency relationship more generally. That is, the work presented focusses not only on the regenerative capability of the TOFT, but also on improving the fidelity of the transformation itself. Greater fidelity of the TOFT was achieved in two ways. In the first instance, an improved time lens with which to obtain the TOFT was developed. In this work we have used cross-phase modulation (XPM) with parabolic pulses to create the time lens, a method motivated by Refs [18] and [19]. The

XPM-based time lenses were refined by investigating several solutions for generating high quality parabolic pulses, such as using sophisticated spectral shaping techniques. These parabolic pulses enabled the demonstration of TOFT-based compensation of timing jitter and dispersion in 10 Gb/s optical signals. The development of the XPM-based time lens was complemented by a theoretical study of the TOFT process. By deriving the occurrence of TOFT analytically, greater understanding of the conditions required to maintain phase preservation in the TOFT process was obtained. Coupled with the improved time lens, we were able to demonstrate a true TOFT complete in both the time and frequency domains, and with greater fidelity than previously demonstrated in compensation-only schemes. A significant part of this work is also centred on a linear form of the FROG pulse characterization technique (L-FROG). This has proven to be an invaluable tool in understanding the relationship between the temporal and spectral domains of the signals I have been working with, including but not limited to the parabolic pulses mentioned above.

This thesis is not presented chronologically, but structured as a journey. It describes the journey of my investigations into performing a perfect TOFT by using XPM with parabolic pulses, from my study of the underlying theory to its implementation and application in high repetition rate telecommunications experiments.

Outline

Chapter 2 provides the background and setting to the main thrust of this thesis. It begins with the history of investigations into the dual natures of time and space. The analogous way in which light behaviour can be viewed in these two domains allows many of the concepts and tools that have been long familiar in the spatial domain to be borrowed for use in the time domain. This leads to the concept of the time lens through which we hope to achieve a TOFT. The theory of TOFTs is developed here and the conditions under which it can be achieved is discussed. The nonlinear processes in fibres are also detailed with particular attention to XPM which is used throughout this work as a method of implementing a time lens.

Chapter 3 regards pulse characterization work performed with the L-FROG technique. The technique is a variation of the commonly used FROG but addresses some of the short-comings of the FROG technique and improves its suitability for low peak power telecommunications signals. The chapter begins with a review of earlier pulse characterization techniques, such as the autocorrelator and the FROG and then covers the operational theory behind the L-FROG. Finally, it presents two experiments which demonstrate the wide applicability of L-FROG characterisations.

The next two chapters apply the TOFT technique to distorted telecommunications signals. The implementation of the TOFT differs in the two chapters, demonstrating two methods of generating the parabolic pulses that are responsible for providing the time lens.

Chapter 4 documents the application of nonlinearly generated parabolic pulses to time lensing. Parabolic pulses are generated from Gaussian pulses through their nonlinear evolution in anomalously dispersive fibre. The parameters which govern the evolution of the pulses into a parabolic shape are discussed with relation to its use as a time lens. The nonlinearly generated parabolic pulses were used to perform TOFTs on signals with severe timing jitter. The swapping of temporal and spectral domains by the TOFT is shown to reduce the timing jitter in the signal.

Superstructured fibre Bragg gratings (SSFBG) were used to generate the parabolic pulses in Chapter 5. These gratings, were used to spectrally shape short sech^2 pulses into good quality parabolic pulses. The parabolic pulses generated by these gratings were used to demonstrate the compensation of second and third order dispersion by using TOFTs.

In Chapter 6 we take a break from TOFTs to consider a new and very flexible way of generating the pulses that we want. These are made using a very stable and broadband optical frequency comb (OFC) which is spectrally carved to form the desired pulses. The generation of the optical frequency comb itself gives rise to some very interesting characteristics, which are investigated in this section. We filter the OFC using two types of tunable filter. The first is a diffraction grating filter which is independently tuneable in both wavelength and bandwidth. The second is based on liquid crystal phase shifters and allows for the spectral phase and intensity to be arbitrarily and dynamically defined by the user [20]. We look at some of the pulse options presented to us by these filters and how the latter can be used to help improve the TOFT.

In the final experimental chapter, Chapter 7, we review the theoretical background to TOFTs which was derived in Chapter 2. The theory is revised to address some of the observations made in Chapters 4 and 5. A greater understanding of TOFT behaviour is attained in this chapter by mapping out a dispersion space of outcomes representing potential perturbations in the TOFT relationship. We also explore the limitations in the experimental execution of the TOFT. These relationships and our revised analysis of TOFTs are verified experimentally.

Chapter 8 concludes this thesis with a summary of the main findings of this work and a discussion of further investigations that this work could lead to.

Bibliography

[1] G. P. Agrawal. *Fiber-Optic Communications Systems.* Microwave and Optical Engineering. John Wiley and Sons, second edition, 1997.

[2] Y. Chigusa, Y. Yamamoto, T. Yokokawa, T. Sasaki, T. Taru, M. Hirano, M. Kakui, M. Onishi, and E. Sasaoka. Low-loss pure-silica-core fibers and their possible impact on transmission systems. *Journal Of Lightwave Technology*, 23(11):3541–3550, 2005.

[3] R. J. Mears, L. Reekie, L. M. Jauncey, and D. N. Payne. Low noise erbium doped fibre amplifier operating at 1.54 mm. *Electronics Letters*, 23:1026, 1987.

[4] S. S. Wagner and H. Kobrinski. Wdm Applications In Broad-Band Telecommunication Networks. *IEEE Communications Magazine*, 27(3):22–30, 1989.

[5] http://www.avvionetworks.com/model_A1020.htm.

[6] CIP Technologies. Impact of Low Cost All-optical Regenerators in High-speed Optical Networks. (http://www.ciphotonics.com/PDFs_Jan08 /Regeneration_White_Paper_v3.pdf), 2008.

[7] http://www.infinera.com/technology/overview.html.

[8] M. Akbulut, A. M. Weiner, and P. J. Miller. Wideband all-order polarisation mode dispersion compensation via pulse shaping. *Optics Letters*, 30(20):2691, 2005.

[9] F. Parmigiani, P. Petropoulos, M. Ibsen, and D. J. Richardson. All-optical pulse reshaping and retiming systems incorporating pulse shaping fibre Bragg gratings. *Journal Of Lightwave Technology*, 24(1):357–364, 2006.

[10] M. Vasilyev and T. I. Lakoba. All-optical multichannel 2R regeneration in a finer-based device. *Optics Letters*, 30(12):1458–1460, 2005.

[11] N. Chi, L. Xu, K. S. Berg, T. Tonkle, and P. Jeppsen. All-optical wavelength conversion and multichannel 2R regeneration based on highly nonlinear dispersion-imbalanced loop mirror. *IEEE Photonics Technology Letters*, 14(11):1581–1583, 2002.

[12] J. Susuki, T. Tanemura, and K. Kikuchi. All-optical regenerator based on XPM-induced wavelength shift in highly-nonlinear fiber at 40 Gb/s. In *Conference on Lasers and Elctro-Optics (CLEO)*, page CMQ6, 2005.

[13] K. Inoue. Suppression of level fluctuation without extinction ratio degradation based on output saturation on higher order optical parametric interaction in fibre. *IEEE Photonics Technology Letters*, 13(4):338–340, 2001.

[14] E. Ciaramella and S. Trillo. All-optical signal rechaping via four-wave mixing in optical fibres. *IEEE Photonics Technology Letters*, 12(7):849–851, 2000.

[15] M. Rochette, J. N. Kutz, J. L. Blows, J. T. Mok, and B. J. Eggleton. Bit-error-rate improvelment with 2R optical regenerators. *IEEE Photonics Technology Letters*, 17(4):908–910, 2005.

[16] R. Trebino. *Frequency-Resolved Optical Gating: The Measurement of Ultrashort Laser Pulses.* Kluwer Acedemic Publishers, 2002.

[17] P. Petropoulos, M. Ibsen, A. D. Ellis, and D. J. Richardson. Rectangular pulse generation based on pulse reshaping using a superstructured fiber Bragg grating. *Journal Of Lightwave Technology*, 19(5):746, 2001.

[18] M. Nakazawa, T. Hirooka, F. Futami, and S. Watanabe. Ideal distortion-free transmission using optical Fourier tranformation and Fourier transform-limited optical pulses. *IEEE Photonics Technology Letters*, 16(4):1059–1061, 2004.

[19] F. Parmigiani, P. Petropoulos, M. Ibsen, and D. J. Richardson. Pulse retiming based on XPM using parabolic pulses formed in a fiber Bragg grating. *IEEE Photonics Technology Letters*, 18(7):829–831, 2006.

[20] M. A. F. Roelens, S. Frisken, J. A. Bolger, D. Abakoumov, G. Baxter, S. Poole, and B. J. Eggleton. Dispersion trimming in a reconfigurable wavelength selective switch. *Journal Of Lightwave Technology*, 26(1):73–78, 2008.

Chapter 2

Introduction to Temporal Optical Fourier Transforms

This chapter concerns the background information leading to the development of a linear distortion compensator based on temporal optical Fourier transforms (TOFT). A TOFT causes the temporal and spectral envelopes of a signal to swap such that its spectral profile is transferred to the temporal domain and vice versa. Thus, a signal with a pulse like spectral envelope such as a Gaussian or sech^2 can restore its original shape by taking on the shape of its spectrum which is unchanged by linear distortions. We begin by reviewing the history of TOFT from initial investigations of the phenomenon to its recent applications. The mathematical theory behind TOFTs is developed giving us insight to the conditions under which we expect it to occur and how the TOFT can be optimised. Having established the theoretical grounding to TOFT, we consider the requirements for its experimental implementation. In aid of this, the latter part of this chapter overviews some of the implementations of time lenses and the nonlinear processes that enable some of them. The $\chi^{(3)}$ nonlinear processes that occur in optical fibres such as self-phase modulation (SPM), cross-phase modulation (XPM) and four-wave mixing (FWM) are especially highlighted for their relevance to our application. The review of these processes allows for understanding of how we can design experiments to maximise the desired nonlinear effects while minimising the undesired nonlinear effects.

2.1 Space-Time Duality

Optical Fourier transformation is not a new concept. It has long been observed in Gaussian optics that a beam focussed through a lens forms a diffraction pattern in the

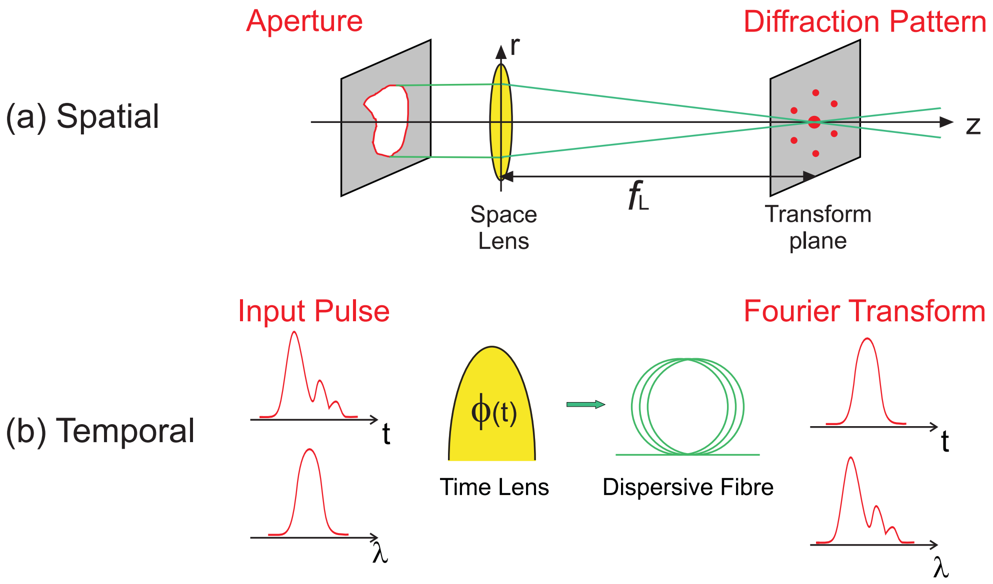

FIGURE 2.1: Space-time duality allows for an analogy to be drawn between spatial optical Fourier transforms which give diffraction patterns and temporal optical Fourier transforms.

focal plane, as shown in Fig. 2.1(a) [1]. Diffraction patterns give the Fourier transform of the aperture placed before the lens, or in the absence of one, the lens' own pupil function. The size of the diffraction pattern is controlled by changing the curvature and focal length of the lens which define its numerical aperture. Understanding diffraction patterns has enabled advances in signal processing in Gaussian optics, such as the use of matched filtering to enable character recognition [1]. Fig. 2.2 shows the principle of using a spatial matched filter in a $4f$ correlator. A beam reflected off the target character $f(x, y)$ at one focal length from lens 1 will form its Fourier transform $F(k_x, k_y)$ at the

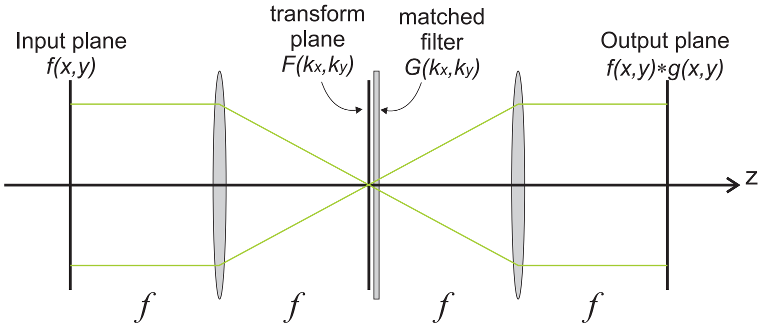

FIGURE 2.2: Spatial matched filtering can be applied with a $4f$ correlator. Multiplication of the beam's Fourier transform $F(k_x, k_y)$ with the Fourier transform of the shape to match $G(k_x, k_y)$ with a mask is equivalent to the correlation of the beam $f(x, y)$ and the desired shape $g(x, y)$. Only if f and g are the same, will the filter be matched and give a high intensity peak.

back focal plane of the lens. A mask $G(k_x, k_y)$ which is the Fourier transform of the shape to match $g(x, y)$ can be placed in this plane to spectrally multiply with F. This is the equivalent of applying a cross-correlation between f and g. In most cases this would yield a noisy output, however if the character and mask match ($f = g$), the cross-correlation will give a high intensity peak in its centre signalling the match.

In 1968, A. Papoulis noted in his book "Systems and Transforms in Optics" that an analogy could be drawn between optical plane propagation and passing electrical signals in time [2]. He used this to consider a range of electronic systems which through mimicking optical systems would be able to perform various signal processing functions. His comparison to electrical rather than optical signals is not surprising since mode-locked lasers and the ability to generate short optical pulses was still a new technology at the time. The connection with optical pulses in time was noted instead by Akhmanov *et al.* that same year [3]. Akhmanov highlighted this interesting analogy while studying the nonlinear optical effects recently exposed by the arrival of mode-locked lasers which enabled pulses to have higher peak powers. However even at this point, the spatial spread of the beams in question meant that not much would be made of his observation in optics. It was not until 1981 after single mode fibres became available and signal propagation could effectively be described as one dimensional, that the concept was revived again by T. and J. Jannson [4]. Jannson and Jannson considered the propagation of pulses in highly dispersive fibre in analogy to Fresnel diffraction. As Papoulis had done, Jannson naturally developed his theory to include other optical processes from which analogies could be drawn, such as optical Fourier transforms. By using an input with a quadratic phase modulation, a real-time Fourier transform could be obtained at a specific focal (dispersive) length after the modulation [5], as shown in Fig. 2.1(b). The focal length through which the signal needed to propagate, was dependent on the dispersion experienced by the signal through that propagation. However at this time Jannson noted that they were unable to generate a stable quadratic phase modulation, and any near-quadratic phase modulation would have such a low chirping ability to require the focal length to be very large.

Kolner followed in 1989, comparing Jannson's quadratic phase modulation to a classical lens and calling it a *time lens* [6]. That is, instead of having the spatial phase modulation

$$\phi(x, y) = \frac{k(x^2 + y^2)}{2f_L}$$

where f_L is the focal length and k is constant, he made the temporal analogy

$$\phi(T) = \frac{\omega_0 T^2}{2 f_T} \tag{2.1}$$

where f_T is now the *focal time* equivalent to the temporal focal distance described by Jannson. Theoretically, Kolner applied the time lens to a temporal imaging system by adding a dispersive element (a length of fibre) before the time lens. This enabled him to obtain a scaled image of the input instead of its Fourier transform. As in spatial imaging, the scaling factor is adjustable by the parameters of the lens and the focal time preceding and following it. A careful choice of parameters can therefore yield pulse compression or stretching. Technology had finally started to catch up to the time-space duality theories in this period causing a revival of interest. Time-space duality began to be regarded for its potential in optical signal processing and while Kolner continued to apply the time lens to imaging [6], Kauffman *et al.* had also begun to demonstrate its Fourier transform applications such as timing jitter compensation [7, 8]. Use of electro-optic modulators also enabled other instruments to be created from the time-space analogy such as time prisms. The concept of the prism pair analogy is shown in Fig. 2.3. Time prisms (like spatial prisms) apply a linear phase ramp across the pulse thus frequency shifting the pulse. To achieve a time prism, the linear portion of the sinusoidal phase modulation is used and given appropriate temporal alignment, the pulse can be chosen to be upshifted or downshifted in frequency [10]. Such time prism pairs have applications in technologies

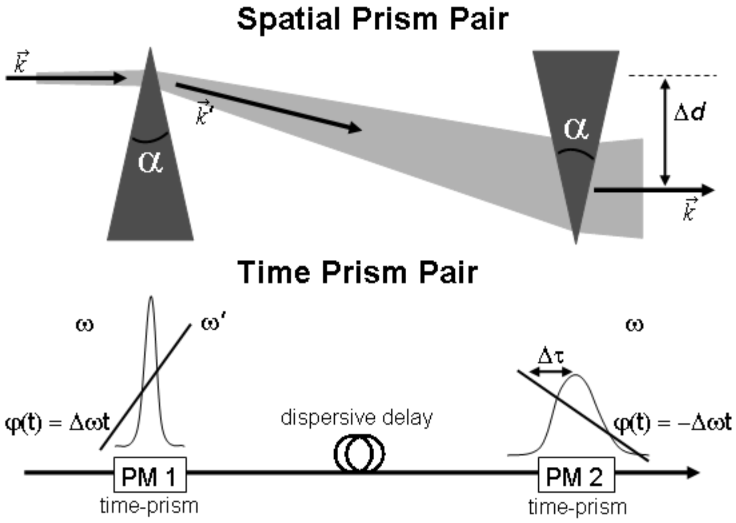

FIGURE 2.3: Prism pairs in space (time) can be used to displace optical pulse in space (time). (Edited from figure in [9])

requiring optical delay lines, just as spatial prism pairs can be used to offset a pulse in space.

These concepts of space-time duality were formalized by Kolner in 1994, with particular focus on the use of electro-optic modulators in temporal imaging [11]. Since then, investigations into applications of the space-time duality have dramatically increased [9]. In the simplest configuration, Muriel *et al.* demonstrated a TOFT without the use of a time lens, but instead based their transformer on the analogy with Fraunhofer diffraction [12, 13]. The large dispersion required to enter this regime is applied with a linearly chirped fibre grating after which the highly dispersed signal will have taken the form of its spectral profile. However, while this scheme is attractive in its passive simplicity and robustness, it produced output pulses which were significantly wider than their inputs making it unsuitable for the applications we will discuss below. In Ref [12] the authors did not suggest an application for the transform and noted that the device was restricted to use with transform limited pulses only.

2.2 Applications of Space-Time Duality

As with the earlier work, more recent space-time duality based schemes also address the applications of pulse compression, pulse characterisation and signal regeneration. Pulse compression is achieved through temporal imaging using one time lens as Kolner had done [11] or with two time lenses in a telescopic configuration [14]. The telescopic configuration, as illustrated with the spatial analogy in Fig. 2.4, uses time lenses of differing chirp to achieve time scaling by transforming the waveform through the spectral domain, and then transforming it back with a different scaling factor. When applied with matching dispersions, this method has the advantage of producing a scaled output

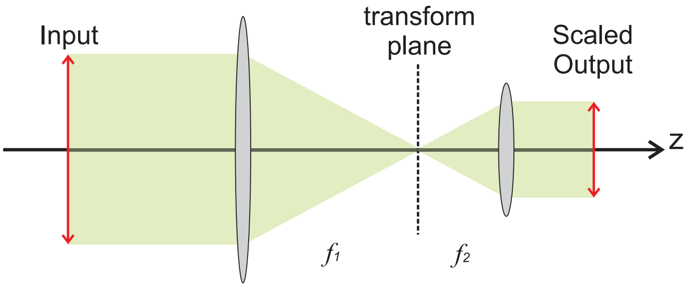

FIGURE 2.4: Two different lenses are used at the correct separation such that a waveform is scaled by the ratio of the focal lengths.

which preserves the phase information of the input, a quality which is not achieved using the single lens. The issue of phase preservation is one which we will encounter again later in this thesis (Sections 2.4 and 7.1). In Ref [14] Foster *et al.* demonstrated also, that the telescopic signal compression technique was suitable for compression of not only pulses, but entire data packets.

Signal characterisation of ultrashort pulses using space-time analogies is usually achieved in one of two regimes. In the first instance, both of the imaging techniques used to compress pulses in the previous paragraph can also be used in reverse to expand the signal. The idea is that by expanding short signals drastically, they can be more easily and more accurately detected on slow electronic detectors [15]. Signal characterisation can also be achieved using time lenses in a TOFT configuration. Rather than expanding the signal, it is Fourier transformed such that its temporal form resides in the spectral domain. This enables the signal waveform to be viewed using a spectrometer thus completely eliminating the need for electronics with fast response times [8, 16, 17].

This brings us to the family of applications that is of greatest interest to this thesis, that is signal regeneration. The principle behind using space-time analogies to achieve signal regeneration rests on the premise that many common impairments to optical pulses are linear in nature and do not alter the spectral content of the pulse. In addition, since common RZ pulse shapes such as Gaussian and sech^2 have spectra of the same form (i.e. Gaussian and sech^2 respectively), the preserved spectral form of the signals can be used to replace the distorted temporal signals when a TOFT is performed. Although this application was only investigated sparingly early on [7], the increasing capacity of optical networks and increasing importance of all-optical processing has brought it to the fore in the last decade. Romagnoli *et al.* used this type of TOFT compensation scheme to demonstrate mitigation of polarisation mode dispersion (PMD) in 10 Gb/s signals [18]. Timing jitter compensation similar in concept to Kauffman's, was also demonstrated by Jiang *et al.* [19] and by Parmigiani *et al.* [20], even if neither of these works mentioned their correlation to space-time duality. However, it is Nakzawa and Hirooka *et al.* who have led much of the literature in this application [21–32]. Although the nature of TOFT compensation enables it to be relatively indifferent to the type of (spectrum-preserving) linear distortion suffered by the signal, Nakazawa and Hirooka's work has mainly focussed on the mitigation of dispersion in transmission systems. As such, these works have brought space-time duality truly to telecommunications by demonstrating their compensator's performance in transmission experiments. From reporting mitigation of a 10 Gb/s signal after 197 km transmission length in 2004 [21], they have scaled their device's performance to enable compensation of 160 Gb/s transmission over 600 km in 2006 [22]. Furthermore, they have shown that TOFT compensation devices can be applied to advanced transmission formats such as differential phase shift keyed (DPSK) signals [23–25].

All of the applications above use time lenses in either an imaging or Fourier transform configuration to manipulate the signals. The difference being the number of lenses and amount of dispersion before and after each lens. Since dispersion is fairly easy to come by in fibre, the question falls as to how the time lensing action is achieved. This incidently, is sometimes the most interesting aspect of some of the mentioned works. We will look more closely at the technologies which enable time lensing next.

2.3 Implementation of Time Lenses

The greatest challenge in performing a TOFT or temporal imaging is the difficulty in implementing a time lens. Unlike its spatial counterpart which can be fashioned from transparent materials, the temporal domain is somewhat less tangible. Most importantly, whatever component or process is used to implement the time lens must be time varying and synchronised with the signal such that the phase shift $\phi(T)$ imposed would be parabolic in the reference frame of the signal. In this section, we review some of the ways in which time lenses have been implemented in experiment.

2.3.1 Linear Time Lenses

The first practical implementation of a time lens was presented by Godil *et al.* who modulated a lithium-niobate crystal ($\mathrm{LiNbO_3}$) in a microwave waveguide to create an electro-optical phase modulator [33]. A schematic of Godil's phase modulator is shown in Fig. 2.5. The microwaves sustained in the waveguide gave the crystal a refractive index that varied with time. By synchronising the modulation with the optical signal, a sinusoidal phase shift is applied to the signal which will be parabolic-like near its crests and troughs, thus acting like a time lens. The modulator was placed in a non-resonant cavity such that it would make 24 passes through the cavity, providing constructive

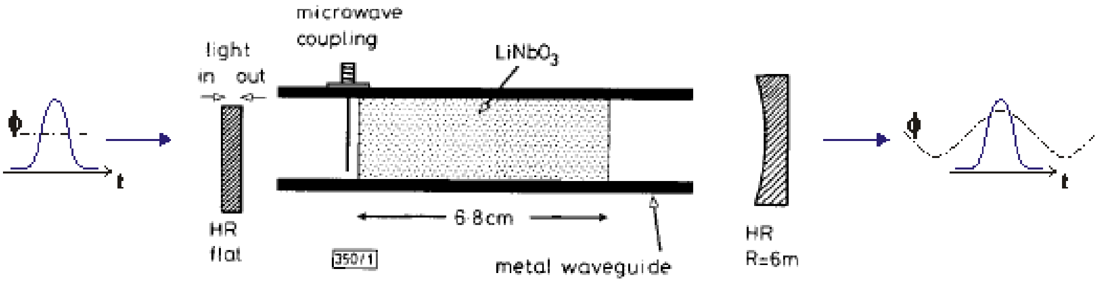

Figure 2.5: Cross section of Godil's multipass microwave optical modulator. A time varying phase shift is induced as the refractive index of the LiNbO$_3$ is modulated by a RF signal. Parts of this figure are obtained from [7]

modulation with each pass before exiting. The sinusoidal phase modulation imparted by the modulator was parabolic enough around its crest to act as a time lens while the multiple passes through the modulator provided enough phase shift to allow Godil to generate pulses from CW light (temporal focussing). Synchronised phase modulators such as Godil's (typically no longer multipass) have been the most common implementation of time lenses due to their simplicity in application [8, 11, 18, 21]. However, while phase modulators are simple to implement and synchronise, the sinusoid is only quadratic-like in a small window of time around its crest. The time lens can therefore only operate within that time window, limiting its applicability to signals with low duty cycles. Furthermore, phase modulators are also limited in the amount of phase shift they are able to induce, limiting the transform quality for signals with high spectral content, as we will see in Eqn. 2.23.

2.3.2 Nonlinear Time Lenses

Alternatively, nonlinear processes such as sum-frequency generation (SFG), cross-phase modulation (XPM) or four-wave mixing (FWM) have also been used to implement time lenses. To understand how each of these are able to impart a quadratic phase shift, let us consider what causes the nonlinear behaviour of light in dielectric media. The $\chi^{(2)}$ nonlinearity responsible for SFG and the $\chi^{(3)}$ nonlinearity responsible for XPM and FWM both arise from the polarization equation given by [34]

$$P_i = \epsilon_0 \left(\sum_j \chi_{ij}^{(1)} E_j + \sum_{jk} \chi_{ijk}^{(2)} E_j E_k + \sum_{jkl} \chi_{ijkl}^{(3)} E_j E_k E_l + \cdots \right) \tag{2.2}$$

where $\chi^{(i)}$ is the i^{th} order susceptibility and is an $(i+1)^{th}$ rank tensor. Eqn. 2.2 relates the i^{th} component of the polarization to the components of the electric field, thus describing the effect of an electric field on the medium in which it propagates. The linear portion, $\chi^{(1)}$, is related to the linear refractive index, n_0, of the medium. For example in a linear isotropic media, $n_0^2 = 1 + \chi_{11}^{(1)}$. When the intensity of the electric field is low, the system is generally linear and this term dominates.

If the intensity of the electric field is increased beyond the linear region, the second order nonlinearity, $\chi^{(2)}$, starts to become significant and Eqn. 2.2 can now be rewritten as

$$\mathbf{P} = \mathbf{P}_L + \mathbf{P}_{NL}, \tag{2.3}$$

where $\mathbf{P}_L = \epsilon_0 \chi^{(1)} \mathbf{E}$ and $\mathbf{P}_{NL} = \epsilon_0 \chi^{(2)} \mathbf{E}^2$ are the linear and nonlinear parts of the polarization respectively. The higher order nonlinear terms have been omitted here due to the dominance of $\chi^{(2)}$. We can then see the effect of the nonlinearity in $\mathbf{P}_{NL}$ by expressing the electric field as a sum of waves [35]

$$\mathbf{E}(\mathbf{r}, t) = \sum_n \mathbf{A}_n e^{i(\mathbf{k}_n \cdot \mathbf{r} - \omega_n t)} + c.c., \tag{2.4}$$

where $\mathbf{A}_n$ is the slowly varying amplitude of the n^{th} wave with carrier frequency ω_0, wave vector $\mathbf{k}_n$ and $c.c.$ denotes the complex conjugate. That is by substituting Eqn. 2.4 into $\mathbf{P}_{NL}$, we find that for two input waves ω_s for the signal and ω_p for the pump we obtain

$$\begin{aligned}
\mathbf{P}_{NL} &\propto ((\mathbf{A}_p e^{i(\mathbf{k}_p \cdot \mathbf{r} - \omega_p t)} + \mathbf{A}_s e^{i(\mathbf{k}_s \cdot \mathbf{r} - \omega_s t)}) + c.c.)^2 \\
&= \underline{((\mathbf{A}_p^2 e^{2i(\mathbf{k}_p \cdot \mathbf{r} - \omega_p t)} + \mathbf{A}_s^2 e^{2i(\mathbf{k}_s \cdot \mathbf{r} - \omega_s t)}) + c.c.)} + \mathbf{A}_p \mathbf{A}_p^* + \mathbf{A}_s \mathbf{A}_s^* \\
&\quad + 2\underline{((\mathbf{A}_p \mathbf{A}_s e^{i((\mathbf{k}_p + \mathbf{k}_s) \cdot \mathbf{r} - (\omega_p + \omega_s) t)} + \mathbf{A}_p \mathbf{A}_s^* e^{i((\mathbf{k}_p - \mathbf{k}_s) \cdot \mathbf{r} - (\omega_p - \omega_s) t)}) + c.c.)}
\end{aligned} \tag{2.5}$$

We can see that the first two terms (solid underline) are oscillating in $2\omega_p$ and $2\omega_s$ respectively, showing that they are at twice their original frequencies. Hence these terms describe the second harmonic generation (SHG) process. The last two terms (dashed underline) are oscillating at $\omega_p + \omega_s$ and $\omega_p - \omega_s$ respectively and are thus the terms describing sum frequency generation (SFG) and difference frequency generation (DFG) respectively. The remaining terms are DC terms and are of no interest to us. Note that the SFG and DFG terms are created in the directions $(\mathbf{k}_p + \mathbf{k}_s)$ and $(\mathbf{k}_p - \mathbf{k}_s)$ respectively. This directionality can be used to separate the terms desired for use from the undesired terms.

A scheme using these relationships to implement a time lens was demonstrated by Bennett and Kolner to demonstrate the use of temporal imaging in signal characterisation [15]. The test signal was a 4-bit, 100 Gb/s data packet of 2.1 ps pulses. Both the signal and the pump were generated in a Nd:YAG laser and spectrally broadened, although the signal was also patterned and compressed. To induce the $\chi^{(2)}$ nonlinearity, they combined the compressed signal with the strongly dispersed pump in a 500 μm thick lithium iodate ($LiIO_3$) crystal. Since they were operating in the degenerate case when $\omega_p = \omega_s$, the DFG product could be neglected and the remaining three terms were separated by setting the two waves to approach the crystal at opposing angles, as shown in Fig. 2.6. Only the SFG term which had contributions from both the incoming waves will not emerge from the crystal at an angle and can be selected with an aperture and measured. The measured SFG term is thus a sum of the characteristics of its parents and the linear chirp of the pump is imparted onto the signal. Since the pump is strongly dispersed and broadened, its intensity will be slowly varying with respect to the signal pulse and have little effect on the shape of the output.

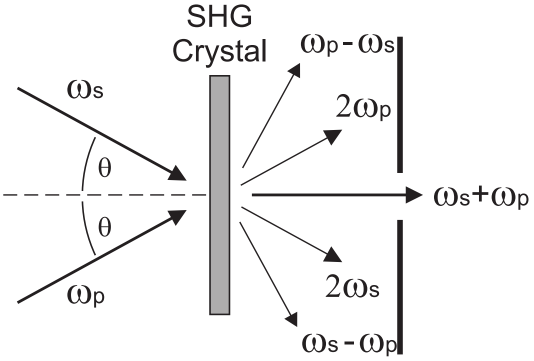

Figure 2.6: Two waves combine in a $\chi^{(2)}$ crystal to form SHG, SFG and DFG products. The SFG product can be selected by an aperture.

However there are several drawbacks to using SFG as a time lens, especially in the context of signal processing for telecommunication systems. Firstly, SFG necessarily places the desired signal at a wavelength very far from the signal's original wavelength which is often practically inconvenient for further use or processing. Although the large wavelength shift can be reduced to some degree by using DFG [36], the high intensities normally required of the signal to achieve SFG and DFG are problematic for many applications including telecommunications which normally use low intensity signals to minimise undesirable nonlinear effects in transmission. Finally and most importantly, in all media with inversion symmetry, such as silica, we require that electric fields pointing in opposite directions will induce equal and opposite reactions in the medium. That is

$$\mathbf{P}(-\mathbf{E}) = -\mathbf{P}(\mathbf{E}).$$

Therefore in optical fibres, the polarization equation must be an odd function, making the $\chi^{(2)}$ nonlinearity neccessarily zero. Therefore, the implementation of SFG and DFG time lenses usually takes place in nonlinear crystals exhibiting second order nonlinearities, making incorporation of the device into fibre systems cumbersome.

2.3.3 Time Lenses in Optical Fibres

If we want time lenses that are implemented in optical fibres for easy integration, we must consider $\chi^{(2)} = 0$. Our attention then falls to the $\chi^{(3)}$ nonlinearity which is the dominating nonlinear term in silica optical fibres. FWM and XPM are some of the effects induced by the $\chi^{(3)}$ nonlinearity. Looking back at Eqn 2.3, we must now have $\mathbf{P}_{NL} = \epsilon_0 \chi^{(3)} \mathbf{E}^3$ as the dominating nonlinear part. Additionally, because we now assume one dimensional propagation in single mode fibre, we can remove the spatial dependence of the electric field in Eqn. 2.4 and simplify it to $E(z,t) = A(z,t)e^{i(kz-\omega t)} + c.c.$. We can now substitute these into the wave equation given by

$$\nabla^2 \mathbf{E} - \frac{1}{c^2}\frac{\partial^2 \mathbf{E}}{\partial t^2} = \mu_0 \frac{\partial^2 \mathbf{P}}{\partial t^2} \tag{2.6}$$

to obtain the nonlinear Schrödinger equation [34]

$$i\frac{\partial A}{\partial z} = -i\frac{\alpha}{2}A - i\beta_1\frac{\partial A}{\partial t} + \frac{\beta_2}{2}\frac{\partial^2 A}{\partial t^2} - \gamma|A|^2 A \tag{2.7}$$

where α is the linear loss, and $\beta_{1,2}$ arise from the coefficients of the propagation constant

$$k(\omega) = \beta_0 + \beta_1\omega + \frac{1}{2}\beta_2\omega^2 + \frac{1}{6}\beta_3\omega^3 + ...$$

when Taylor expanded around ω_0. Then for three input waves ω_p, ω_s and ω_i into a fibre, we can express them together as

$$A = \sum_{n=1}^{N} A_n(z)e^{i((k_n-k_0)z-(\omega_n-\omega_0)t)}$$

and substitute it into Eqn 2.7 to derive the how the waves mix as they propagate along the fibre (similarly to Eqn 2.5). By separating the mixing terms with respect to their frequencies, we can then obtain three coupled equations, each describing the growth of one of the waves. These are

$$\begin{aligned}\frac{dA_s}{dz} &= -i\gamma\{A_s|A_s|^2 + 2A_s(|A_p|^2 + |A_i|^2) + A_p^2 A_i^* e^{i(2k_p - k_s - k_i)z}\} && (2.8)\\ \frac{dA_p}{dz} &= -i\gamma\{A_p|A_p|^2 + 2A_p(|A_i|^2 + |A_s|^2) + A_i A_s A_p^* e^{i(k_s + k_i - 2k_p)z}\} && (2.9)\\ \frac{dA_i}{dz} &= -i\gamma\{A_i|A_i|^2 + 2A_i(|A_p|^2 + |A_s|^2) + A_p^2 A_s^* e^{i(2k_p - k_s - k_i)z}\} && (2.10)\end{aligned}$$

Considering the first equation governing the signal (Eqn. 2.8) we can see that it contains a term in $|A_s|^2$, a term in $|A_p|^2$ and a mixed term. Since we have actually only input the signal and pump waves, the term in $|A_i|^2$ is small and can be disregarded. To see how the first term affects the signal, we momentarily look at it in isolation. That is, we have

$$\frac{dA_s}{dz} = -i\gamma|A_s|^2 A_s \tag{2.11}$$

which is an ordinary differential equation with the solution

$$A_s = A_0 \mathrm{e}^{-i\gamma|A_s|^2 z} = A_0 \mathrm{e}^{-i\phi_s} \tag{2.12}$$

We can see then that this first term describes the dependence of the signal phase on its own intensity or self-phase modulation (SPM). Similarly, the second term can be isolated to give the solution

$$A_s = A_0 \mathrm{e}^{-2i\gamma|A_p|^2 z} = A_0 \mathrm{e}^{-i\phi_s} \tag{2.13}$$

describing the dependence of the signal phase on the pump's intensity or cross-phase modulation (XPM). The final term is a mixed term arising from FWM and describes the amplification of the signal by the annihilation of two pump photons to create a signal and idler photon. That is, $2\omega_p \rightarrow \omega_s + \omega_i$. Similar elements can also be seen in the equations governing the pump and idler waves.

FWM time lens

The FWM process has been used to implement time lensing in a fashion very similar to the SFG time lenses. A linearly chirped and broadened pump pulse is coupled with the target signal in a nonlinear medium to generate an idler as described by Eqn 2.10. The

FWM term in this expression shows that if the pump and signal are efficiently phase matched, then the growth of the new idler wave will be related to the pump and signal by the relationship $A_i \propto A_p^2 A_s^*$. As a result, the idler phase will be given by the phase of the input signal minus twice the pump's phase, which for the linearly chirped pump is quadratic. If the pump is also significantly broadened, then its amplitude will be slowly varying with respect to the signal pulse leaving the idler essentially a replica of the signal with only the extra quadratic phase added. The idler can then be filtered out and used as a wavelength converted signal. The FWM time lens has been demonstrated by Foster *et al.* on a 1 cm long embedded silicon-on-insulator nanowaveguide [37]. The group had previously demonstrated other FWM devices in these silicon waveguides such as wavelength conversion and parametric amplification [38, 39]. The silicon waveguide is pumped with a pump pulse dispersed to twice the desired focal time of the time lens, which can then be used in many of the applications previously described. So far, pulse characterisation with both the pulse expansion and TOFT methods have been reported [17, 37], as well as data packet compression for up to 270 Gb/s transmission in a telescopic configuration [14]. In addition, FWM has the benefit of involving wavelengths over a far narrower spectral range than SFG and also a much lower signal power. These qualities recommend the FWM time lens above the SFG approach. However, both these processes still put the output pulse at a different wavelength to the original which can be undesirable.

XPM time lens

This brings us to XPM. We saw from Eqn 2.13 that XPM creates the phase shift not from the strong pump's phase profile (as was the case with SFG and FWM), but from its *intensity* profile onto the weaker signal. Furthermore, the phase is created directly rather than being incorporated into the generation of a new wave, thus it preserves the signal's input wavelength. By observation of Eqn. 2.9, we can see that if the intensity of the signal is high, the reverse can also occur and both wavelengths can also undergo SPM. To get a good parabolic phase shift, these latter effects of reverse XPM and of SPM are undesired and can be avoided by keeping the intensity of the target signal low. XPM was used by Mouradian *et al.* to implement a time lens for application to pulse characterisation by TOFT [16]. The XPM was induced in a nonlinear single mode fibre by a Gaussian pump pulse, which was amplified up to a peak power of 1 kW. Like the

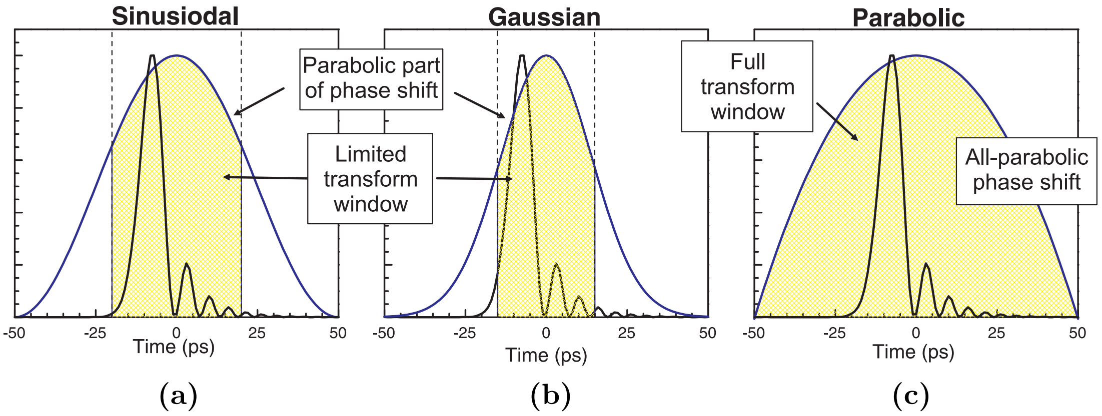

FIGURE 2.7: Usable duty cycles over which (a) a sinusoid, (b) a Gaussian and (c) a parabolic can induce a parabolic phase shift.

sinusoid, the Gaussian shape is parabolic-like in the region around its peak and thus can be used to apply a parabolic phase shift for time lensing. By having such a high peak power, the pump shape is steepened which in turn increases the chirp applied to the signal. This simultaneously highlights one of the benefits and also one of the drawbacks of using XPM compared to the other methods. While it is beneficial to be able to tune the chirp of the time lens through simple amplification and without sacrificing any of the duty cycle, the requirement for high power in itself is not desirable nor are the other nonlinear effects it induces such as SPM. Note that the duty cycle here refers to the percentage of the pump period which can be used for time lensing, and should not be confused with the duty cycle of the signal which refers to the percentage of the signal period which is occupied by the signal pulse (FWHM).

All the time lenses mentioned so far have a common downside. The large dispersion required by the pump in the SFG and FWM schemes and the limited parabolic-like region of Gaussians means that like the phase modulator, only signals with low duty cycles are appropriate for these time lenses. The applicability of time lenses would be far greater if a parabolic phase shift could be applied to the signal pulse that could cover a greater portion of its duty cycle as shown in Fig. 2.7. The extended coverage is especially important for telecommunications systems in which high duty cycles are essential for maximising the capacity of each channel. One method to achieve the parabolic phase shift, as suggested by M. Nakazawa, is to generate a time lens by using XPM with a parabolic pulse [32]. As with Mouridian's scheme mentioned above, the intensity of the pump pulse would be imparted onto the signal without generation of another wave. But the parabolic profile of the pump pulse in this case would extend over all or almost all of the entire period of the signal pulse and thus enable the time lens to operate over the entire time slot. As well as catering to the higher duty cycles of telecoms signals, the wider time window would also increase the time lens' capability to regenerate greater distortions in a data signal.

Parabolic pulses have recently received a lot of attention for the linear chirp they can impart through nonlinear effects. This has various applications in pulse amplification [40], supercontiuum generation [41] and optical signal processing [20]. In this latter reference, Parmigiani *et al.* have used XPM with parabolic pulses to demonstrate a timing jitter compensator, similar in concept to the one previously presented by Jiang *et al.* [19]. Although not explicitly discussed as a TOFT, Parmigiani showed that a linear chirp imposed though XPM with a parabolic pulse and followed with dispersion could be used to mitigate timing jitter in a 10 Gb/s data stream. Furthermore, the steep sides of her parabolic pulses made them suitable for multiplexing up to higher bit rates and thus potentially useful for high duty cycle, high repetition rate telecommunications signals. However despite the many benefits of parabolic pulse time lenses, this technique has so far not been well investigated due to the difficulty in generating suitable parabolic pulses.

2.3.4 Summary of Time Lensing Techniques

I have reviewed in this section the wide variety of techniques that have been previously used to implement time lenses. A summary of the main types of time lenses is given in Fig 2.1 along with a breakdown of their main advantages (green) and disadvantages (red). In particular the characteristics which are of relevance to telecommunications systems have been considered. It can be seen that each of the time lensing methods listed have characteristics which make them suitable for a particular application. While the large majority of research in this area has used the electro-optic phase modulator for its simplicity, optical signal processing would ultimately benefit from the high duty cycle of using XPM with parabolic pulses. This is the only method shown that could potentially be used with high repetition rate telecommunications signals *without* the need for demultiplexing, which is one of the main motivations for developing all-optical signal processing. However as stated above, much of the challenge in implementing this technique is in generating parabolic pulses with which XPM time lenses can be induced.

Linearity	Method	Fiber?	Chirp	Power Needed	Duty Cycle	λ-shift	Other Comments	Reference
Linear	EO phase modulation	yes	limited	low	low	none	Direct, robust	most
$\chi^{(2)}$	SFG with chirped pump	no	$\propto$ pump bandwidth	high	very low	large		[15] [42]
$\chi^{(3)}$	FWM with chirped pump	yes	$\propto$ pump bandwidth	low signal high pump	very low	small		[17] [14] [37]
	XPM with Gaussian pump	yes	$\propto$ pump power	low signal high pump	low	none		[16]
	XPM with parabolic pump	yes	$\propto$ pump power	low signal high pump	high	none	Parabolic pulses difficult to generate	[28] [20] [43]

TABLE 2.1: Summary of time lensing techniques

In this thesis, I use three different ways of generating parabolic pulses and use them as time lenses to demonstrate TOFTs. In the first scheme described in Chapter 4, parabolic pulses are generated nonlinearly through propagation in normally dispersive fibre. This is the most widely known method of generating parabolic pulses and depends on the natural evolution of Gaussian pulses in such media. The balance between dispersion and SPM is crucial here to the development of an accurate parabolic shape. However due to the constraints of the parabolic generation process, we found that this method was not ideal for time lensing which had different power and dispersion requirements. In Chapter 5 we try a different approach and generate parabolic pulses by using a superstructured fibre Bragg grating (SSFBG). SSFBGs have modulated intensity envelopes was well as the rapid refractive index modulation of normal Bragg gratings. They can be designed to perform pulse shaping, by changing the phase and intensity of the spectral content of the signal [44]. Using such a grating, Parmigiani *et. al.* were able to demonstrate the generation of 10 ps wide parabolic pulses at 10 GHz [20]. While these parabolic pulses are not wide enough to cover the entire period of the signal, we demonstrate in Chapter 5 that they are indeed suitable for time lensing and TOFT. In our final demonstration in Chapter 7, parabolic pulses were generated using a newly available programmable spectral filter. The flexibility of the filter makes it a valuable experimental tool, especially when coupled with the optical frequency comb source described in Chapter 6. The combination of the programmable filter and the frequency comb allows for a flexible and stable experimental setup with which we can further explore the behaviour of pulses propagating through a time lens.

2.4 Temporal Optical Fourier Transforms

Having reviewed space-time duality and the implementation of time lenses, we consider now the specific case of TOFTs. To thoroughly understand the theory underpinning TOFTs we begin by inspecting the processes applied to the input signal to achieve the transform. That is, the effect of a time lens followed by a dispersive element. Let us consider then an arbitrary input pulse $A_{in}(T)$, where $T = t - \beta_1 z$ is the time variable shifted to be in the reference frame of the initial pulse. The application of a time lens as defined in Eqn 2.1 and the dispersion following it can be expressed as the operators

$$H(T) = \exp\left[i\frac{\omega_0 T^2}{2f_T}\right] \qquad \text{and} \qquad G(\omega) = \exp\left[i\frac{\xi}{2}\omega^2\right] \tag{2.14}$$

respectively, where $\xi = \beta_2 z$. Thus the signal pulse after the dispersive medium would have the form

$$A_{out}(T) = F^{-1}\{F\{A_{in}(T)H(T)\}G(\omega)\}. \tag{2.15}$$

Using the convolution theorem [45], Eqn. 2.15 can be simplified to

$$A_{out}(T) = (A_{in}(T)H(T)) * G(T) = \int_{-\infty}^{\infty} A_{in}(T')H(T')G(T-T')dT'. \tag{2.16}$$

where $G(T)$ is the time domain form of the dispersion operator $G(\omega)$ given by

$$G(T) = F^{-1}\{G(\omega)\} = \frac{1}{\sqrt{2\pi i\xi}}\exp\left[i\frac{T^2}{2\xi}\right]. \tag{2.17}$$

The operators $H(T)$ and $G(T)$ can then be substituted into Eqn. 2.16 to obtain

$$\begin{aligned} A_{out}(T) &= \int_{-\infty}^{\infty} A_{in}(T')\exp\left[i\frac{\omega_0}{2f_T}T'^2\right]\frac{1}{\sqrt{2\pi i\xi}}\exp\left[i\frac{(T-T')^2}{2\xi}\right]dT' \\ &= \frac{1}{\sqrt{2\pi i\xi}}\exp\left[i\frac{T^2}{2\xi}\right]\int_{-\infty}^{\infty} A_{in}(T')\exp\left[i\left(\frac{\omega_0 T'^2}{2f_T} + \frac{T'^2 - 2TT'}{2\xi}\right)\right]dT', \end{aligned}$$

which can then be written in the form

$$A_{out}(T) = \frac{1}{\sqrt{2\pi i\xi}}\exp\left[i\frac{T^2}{2\xi}\right]\int_{-\infty}^{\infty} A_{in}(T')\exp\left[i\left(\frac{\omega_0}{2f_T} + \frac{1}{2\xi}\right)T'^2\right]\exp\left[-i\left(\frac{T}{\xi}\right)T'\right]dT'. \tag{2.18}$$

Thus if we let

$$\omega = \frac{T}{\xi}, \tag{2.19}$$

the output waveform can be seen to resemble the Fourier transform of the input waveform with a chirp. Eqn. 2.19 defines the transform scaling that would apply to transfer the spectrum into the time domain. For example, the temporal width of the resulting field will be given by $\Delta\tau_0 = \Delta\omega\xi$, where $\Delta\omega$ is the spectral width of the initial pulse.

Secondly to preserve the initial spectral shape, we require the phase shift in T'^2 to be equal to zero. Noting that $\frac{d^2\phi}{dT^2} = \frac{\omega_0}{f_T}$, we obtain the condition

$$K = -\frac{\partial^2\phi}{\partial T^2} = \frac{1}{\xi} \tag{2.20}$$

where K is the chirp rate associated with the phase shift. When the required conditions hold, the output waveform becomes

$$A_{out}(T) = \frac{1}{\sqrt{2\pi i\xi}}A_{in}(\omega = T/\xi)\exp\left[i\frac{T^2}{2\xi}\right] \tag{2.21}$$

Even so, it can be seen that Eqn. 2.21 is not a perfect scaled Fourier transform of the input. The residual phase term means that even when the above conditions are met, a Fourier transform is only obtained in the temporal domain and not in the spectral domain. Instead if we follow the same process as above and apply the same conditions, we obtain for the output spectrum

$$A_{out}(\omega) = \sqrt{\frac{\xi}{2\pi i}} \int_{-\infty}^{\infty} A_{in}(\omega')\text{exp}\left[i\frac{\omega'^2}{2K}\right]\exp\left[-i(\tau = \omega\xi)\omega'\right] d\omega'. \tag{2.22}$$

Thus, to also obtain a Fourier transform in the spectral domain, we require the residual phase term to be negligible. That is,

$$|K| >> \omega^2. \tag{2.23}$$

This shows that we need to induce a greater chirp to properly Fourier transform pulses with a high spectral content. This can be clearly seen in the examples shown in Figs. 2.8 and 2.9. Fig. 2.8 shows the numerical simulation of TOFT being applied with a parabolic phase shift to a double peaked Gaussian pulse when $K = -1.48$ ps^{-2}. Fig. 2.9 shows the numerical simulation now being applied to a square pulse. It can be seen that although the two pulses have similar peak powers and pulse widths, the high spectral content of the square pulse renders the Fourier transform in the frequency domain quite poor. By contrast, the Fourier transform in the temporal domains are both very good since the temporal waveform is unaffected by the residual phase term.

We can find the relationship between the parabolic pump pulse and the signal phase by first defining the profile of the parabolic pump pulse as

$$|A_p(0,\tau)|^2 = P_p\left[1 - \left(\frac{\sqrt{2}\tau}{\tau_w}\right)^2\right] \tag{2.24}$$

with P_p being the peak power of the parabolic pulse and τ_w its full width at half maximum (FWHM). Note that this is only valid for $-\sqrt{2}\tau_w < \tau < \sqrt{2}\tau_w$, since the pump power must be zero elsewhere. XPM of this pump with the signal pulse $A_{in}(T)$ will cause it to gain a phase shift given by [34]

$$\phi(\tau) = \gamma\left(L|A_{in}(T)|^2 + 2\int_0^L |A_p(0,\tau - z\mathrm{d})|^2 dz\right) \tag{2.25}$$

where γ is the nonlinear coefficient of the fibre in which the XPM occurs and L is its length. d is the walk-off parameter between the group velocities, v_g, of the two pulses and is given by $\mathrm{d} = 1/v_{g2} - 1/v_{g1}$. We can choose to make d negligible by choosing a

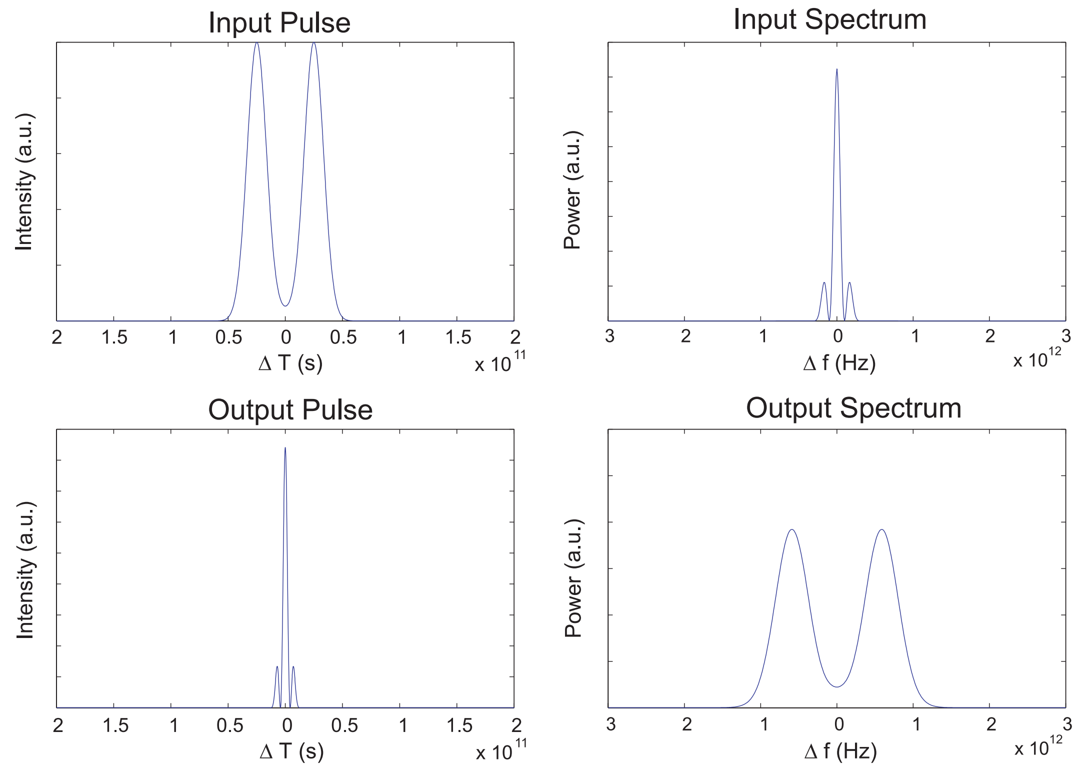

Figure 2.8: Simulation of a double peaked pulse undergoing TOFT.

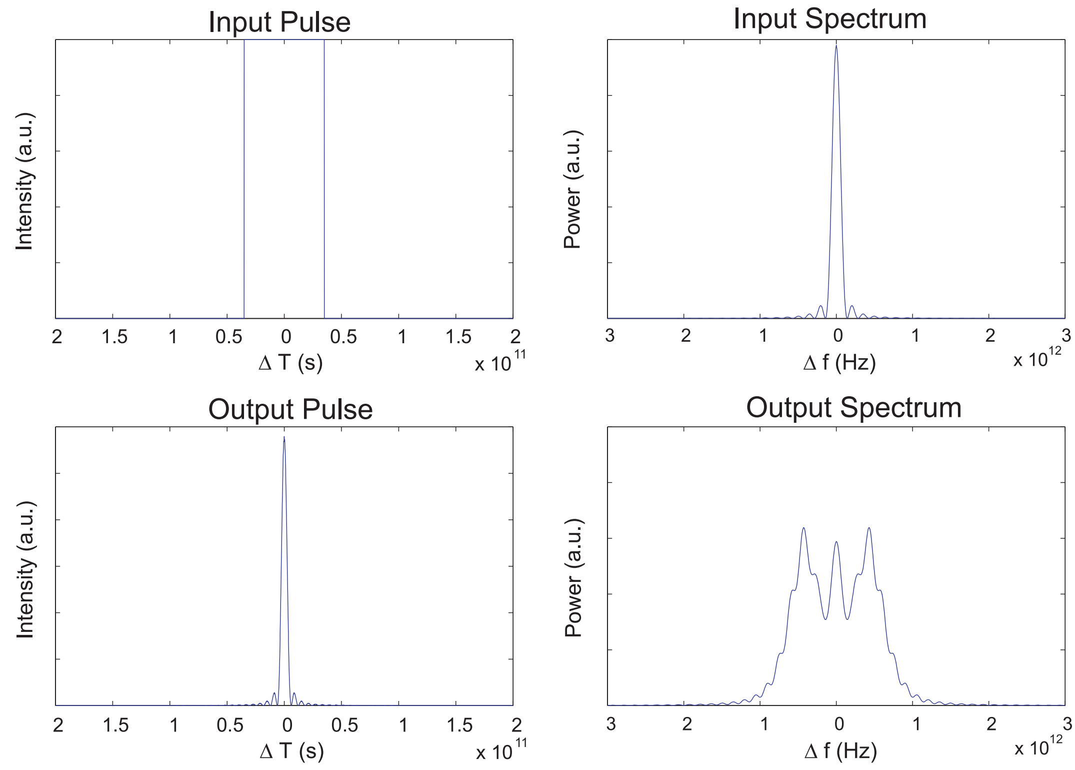

Figure 2.9: Simulation of a square pulse undergoing TOFT.

nonlinear medium in which the zero-dispersion wavelength is centred exactly between the signal and pump wavelengths. In this case $v_{g2} \approx v_{g1}$ and d will be small. Since the pump pulse will have a much higher intensity than the signal, we can make the assumptions $|A_{in}|^2 + 2|A_p|^2 \approx 2|A_p|^2$, and also $|A_p(\epsilon, \tau)|^2 \approx |A_p(0, \tau)|^2$ if the dispersion is low. Thus the total phase shift experienced by the signal due to XPM will be

$$\phi(\tau) = 2\gamma L P_p \left[1 - \left(\frac{\sqrt{2}\tau}{\tau_w} \right)^2 \right], \tag{2.26}$$

from which we can find

$$K = \frac{8\gamma L}{\tau_w^2} P_p. \tag{2.27}$$

Thus we can easily tune the scaling of the TOFT by varying the power of the pump pulse, which in turn will increase K.

2.5 Conclusions

In this chapter an introduction to the concept of space-time duality is given, leading to an understanding of how time lenses can be used to produce a TOFT. Applications using temporal analogues of classical optical components to achieve useful signal processing functions have been described with particular emphasis on systems to using TOFTs. As with spatial systems, time lenses play a large role in temporal systems. We review the non-trivial implementation of these time lenses beginning with a discussion on the nonlinear optical phenomena on which many of them are based. The use of XPM with parabolic pulses is of particular interest, since it is the most appropriate time lens for use with high repetition rate telecommuncations signals. It will thus be the method by which we will demonstrate and analyze TOFTs in this thesis.

With the aim of using TOFTs as a distortion compensator in telecommunications systems, the following chapters present three methods of generating parabolic pulses for high duty cycle time lensing. Chapter 4 explores parabolic pulses generated in a length of normally dispersive fibre, Chapter 5 explores parabolic pulses generated in a superstructured fibre Bragg grating (SSFBG) and Chapter 6 we use the combination of a reconfigurable filter and an optical frequency comb to shape dark parabolic pulses.

But before we look at these three approaches to performing TOFT, we must first describe some of the tools we will use, the most important being the linear frequency resolved gating (L-FROG) pulse characterisation technique. The description of the L-FROG technique along with its background and similar techniques is presented next in Chapter 3. This chapter also includes some examples of experiments in which I have used the L-FROG to characterize some particularly interesting signals. The L-FROG presents a complete and clear representation of the signals in a way that cannot be achieved with more traditional pulse characterisation methods.

Bibliography

[1] J. W. Goodman. *Introduction to Fourier Optics.* Roberts and Company, 1968.

[2] A. Papoulis. *Systems and Transforms with Applications in Optics.* McGraw-Hill, 1968.

[3] S. A. Akhmanov, A. S. Chirkin, K. N. Drabovich, A. I. Kovrigin, R. V. Khokhlov, and A. P. Sukhorukov. Nonstationary nonlinear optical effects and ultrashort light pulse formation. *IEEE Journal of Quantum Electronics*, 4(10):598–605, 1968.

[4] T. Jannson and J. Jannson. Temporal self-imaging effect in single-mode fibres. *Journal of the Optical Society of America*, 71(11):1373–1376, 1981.

[5] T. Jannson. Real-time Fourier transformation in dispersive optical fibers. *Optics Letters*, 8(4):232–234, 1983.

[6] B. H. Kolner and M. Nazarathy. Temporal imaging with a time lens. *Optics Letters*, 14(12):630–632, 1989.

[7] M. T. Kauffman, A. A. Godil, B. A. Auld, W. C. Banyai, and D. M. Bloom. Applications of time lens optical systems. *Electronics Letters*, 29(3):268–269, 1993.

[8] M. T. Kauffman, W. C. Banyai, A. A. Godil, and D. M. Bloom. Time-to-frequency converter for measuring picosecond optical pulses. *Applied Physics Letters*, 64(3): 270–272, 1994.

[9] J. v Howe and C. Xu. Ultrafast optical signal processing based upon space-time dualities. *Journal Of Lightwave Technology*, 24(7):2649–2662, 2006.

[10] J. v Howe and C. Xu. Ultrafast optical delay line by use of a time-prism pair. *Optics Letters*, 30(1):99–101, 2005.

[11] B. H. Kolner. Space-time duality and the theory of temporal imaging. *IEEE Journal of Quantum Electronics*, 30(8):1951–1963, 1994.

[12] M. A. Muriel, J. Azana, and A. Carballar. Real-time Fourier transformer based on fiber gratings. *Optics Letters*, 24(1):1, 1999.

[13] E. Hecht. *Optics*. Addison Wesley, San Francisco, 4th edition, 2002.

[14] M. A. Foster, R. Salem, Y. Okawachi, A. C. Turner-Foster, M. Lipson, and A. L. Gaeta. Generation of 270 Gb/s NRZ data packets from a 10-Gb/s signal using a temporal telescopic system. In *Optical Fiber Communications Conference*, page OWS4, San Diego, 2009.

[15] C. V. Bennett, R. P. Scott, and B. H. Kolner. Temporal magnification and reversal of 100 Gb/s optical data with an up-conversion time microscope. *Applied Physics Letters*, 65(20):2513–2515, 1994.

[16] L. K. Mouradian, F. Louradour, V. Messager, A. Barthelemy, and C. Froehly. Spectro-temporal imaging of femtosecond events. *IEEE Journal of Quantum Electronics*, 36(7):795–801, 2000.

[17] Mark A. Foster, Reza Salem, David F. Geraghty, and Amy C. Turner-Foster. Silicon-chip-based ultrafast optical oscilloscope. *Nature*, 456:81–84, 2008.

[18] M. Romagnoli, P. Franco, R. Corsini, A. Schiffini, and M. Midrio. Time-domain Fourier optics for polarization-mode dispersion compensation. *Optics Letters*, 24 (17):1197–1199, 1999.

[19] L. A. Jiang, M. E. Grein, H. A. Haus, and E. P. Ippen. Timing jitter eater for optical pulse trains. *optics letters*, 28(2):78–80, 2003.

[20] F. Parmigiani, P. Petropoulos, M. Ibsen, and D. J. Richardson. Pulse retiming based on XPM using parabolic pulses formed in a fiber Bragg grating. *IEEE Photonics Technology Letters*, 18(7):829–831, 2006.

[21] M. Nakazawa, T. Hirooka, F. Futami, and S. Watanabe. Ideal distortion-free transmission using optical Fourier tranformation and Fourier transform-limited optical pulses. *IEEE Photonics Technology Letters*, 16(4):1059–1061, 2004.

[22] T. Hirooka, K. I. Hagiuda, T. Kumakura, K. Osawa, and M. Nakazawa. 160-Gb/s-600-km OTDM Transmission Using Time-Domain Optical Fourier Transformation. *IEEE Photonics Technology Letters*, 18(24):2647–2649, 2006.

[23] T. Hirooka, M. Okazaki, and M. Nakazawa. A Straight-Line 160-Gb/s DPSK Transmission Over 1000 km With Time-Domain Optical Fourier Transformation. *IEEE Photonics Technology Letters*, 20(13):1094–1096, 2008.

[24] T. Hirooka, M. Okazaki, P. Guan, and M. Nakazawa. 320-Gb/s Single-Polarization DPSK Transmission Over 525 km Using Time-Domain Optical Fourier Transformation. *IEEE Photonics Technology Letters*, 20(22):1872–1874, 2008.

[25] P. Guan, M. Okazaki, T. Hirano, T. Hirooka, and M. Nakazawa. Low-Penalty 5 x 320 Gb/s/Single-Channel WDM DPSK Transmission Over 525 km Using Time-Domain Optical Fourier Transformation. *Photonics Technology Letters, IEEE*, 21 (21):1579–1581, 2009.

[26] M. Nakazawa and T. Hirooka. Distortion-free optical transmission using time domain optical Fourier transformation and transform-limited optical pulses. *Journal Of The Optical Society Of America B-Optical Physics*, 22(9):1842–1855, 2005.

[27] T. Hirooka, M. Nakazawa, F. Futami, and S. Watanabe. A new adaptive equalization scheme for a 160-Gb/s transmitted signal using time-domain optical Fourier transformation. *IEEE Photonics Technology Letters*, 16(10):2371–2373, 2004.

[28] T. Hirooka and M. Nakazawa. All-Optical 40-GHz Time-Domain Fourier Transformation Using XPM With a Dark Parabolic Pulse. *IEEE Photonics Technology Letters*, 20(22):1869–1871, 2008.

[29] T. Hirooka, M. Nakazawa, and K. Okamoto. Bright and dark 40 GHz parabolic pulse generation using a picosecond optical pulse train and arrayed waveguide grating. *Optics Letters*, 33(10):1102–1104, 2008.

[30] M. Okazaki, Guan Pengyu, T. Hirooka, M. Nakazawa, and T. Miyazaki. 160-Gb/s 200-km Field Transmission Experiment With Large PMD Using a Time-Domain Optical Fourier Transformation Technique. *Photonics Technology Letters, IEEE*, 20(24):2192–2194, 2008.

[31] T. Hirooka and M. Nakazawa. Derivation of analytical expression for third-order dispersion using time-domain optical Fourier transformation. In *European Conference on Optical Communication*, volume 3, pages 653–654, 2005.

[32] T. Hirooka and M. Nakazawa. Optical adaptive equalization of high-speed signals using time-domain optical fourier transformation. *Journal Of Lightwave Technology*, 24(7):2530–2540, 2006.

[33] A. A. Godil, B. A. Auld, and D. M. Bloom. Time-lens producing picosecond optical pulses. In *IEEE Lasers and Electro-Optics Society annual meeting*, page 672 (OTA1.2), Boston, 1992.

[34] G. P. Agrawal. *Nonlinear Fiber Optics*. Optics and Photonics. Academic Press, third edition, 2001.

[35] R. W. Boyd. *Nonlinear Optics*. Academic Press, third edition, 2008.

[36] C. V. Bennett and B. H. Kolner. Principles of parametric temporal imaging - Part I: System Configurations. *IEEE Journal of Quantum Electronics*, 36(4):430–437, 2000.

[37] R. Salem, M. A. Foster, A. C. Turner, D. F. Geraghty, M. Lipson, and A. L. Gaeta. Optical time lens based on four-wave mixing on a silicon chip. *Optics Letters*, 3 (10):1047–1049, 2008.

[38] R. Salem, M. A. Foster, A. C. Turner, D. F. Geraghty, M. Lipson, and A. L. Gaeta. Signal regeneration using low-power four-wave mixing on silicon chip. *Nature Photonics*, 2:35–38, 2008.

[39] M. A. Foster, A. C. Turner, J. E. Sharping, B. S. Schmidt, M. Lipson, and A. L. Gaeta. Broad-band optical parametric gain on a silicon photonic chip. *Nature*, 441: 960–963, 2006.

[40] C. Finot, J. M. Dudley, D. J. Richardson, B. Kibler, and G. Millot. Optical Parabolic Pulse Generation and Applications. *IEEE Journal of Quantum Electronics*, 45(11), 2009.

[41] J. Wang, Y. Wu, C. Lou, and Y. Gao. Pedestal-free 10GHz pulse compression using comb-like dispersion prifiled fibers and its application in 40-Gb/s OTDM systems. *Optical Engineering*, 42(8):2380–2383, 2003.

[42] C. V. Bennett and B. H. Kolner. Upconversion time microscope demonstrating 103 x magnification of femtosecond waveforms. *Optics Letters*, 24(11):783–785, 1999.

[43] T. T. Ng, F. Parmigiani, M. Ibsen, Z. Zhang, P. Petropoulos, and D.J. Richardson. Compensation of linear distortions by using XPM with parabolic pulses as a time lens. *IEEE Photonics Technology Letters*, 20(13):1097–1099, 2008.

[44] P. Petropoulos, M. Ibsen, A. D. Ellis, and D. J. Richardson. Rectangular pulse generation based on pulse reshaping using a superstructured fiber Bragg grating. *Journal Of Lightwave Technology*, 19(5):746, 2001.

[45] E. Kreyszig. *Advanced Engineering Mathematics*. John Wiley and Sons, 8th edition, 1999.

Chapter 3

The Linear FROG

In the development of a TOFT, it is important to be able to map signals in both the temporal and spectral domains and the relationship between them. This relationship, expressed in the phase of the signal, is acted on by various processes in TOFT such as time lensing. A pulse characterisation tool that gives us knowledge of the signal phase is clearly crucial. In this chapter we look at some different types of pulse characterisation techniques. In particular we will focus on the frequency resolved optical gating (FROG) technique and a variation of it which uses linear rather than nonlinear gating. This is the preferred pulse phase measurement technique used in this thesis and we call this the L-FROG even though its gating mechanism is not actually optical. The first part of this chapter reviews some traditional pulse characterisation techniques which do not measure signal phase but are also routinely used in the experiments in this thesis. We then move on to reviewing signal phase measurement techniques before describing the FROG and L-FROG. The latter part of the chapter presents some examples of experiments in which the L-FROG was used to either measure some interesting pulse types or to characterise an active component (a semiconductor optical amplifier (SOA) in this case), showing its versatility.

3.1 Background

Pulse characterization is important and useful for the development of many optical applications. Of most interest is normally the size, shape and spectral content of a given signal. The simplest of these is the spectral measurement. A diagram of a basic spectrometer is shown in Fig. 3.1. A reflection grating is used to separate frequency components of the signal which are then selected and measured with a scanning aperture and photodetector. A photodetector-array would also suffice here instead of scanning, but the resolution would be limited to the array resolution rather than the aperture size.

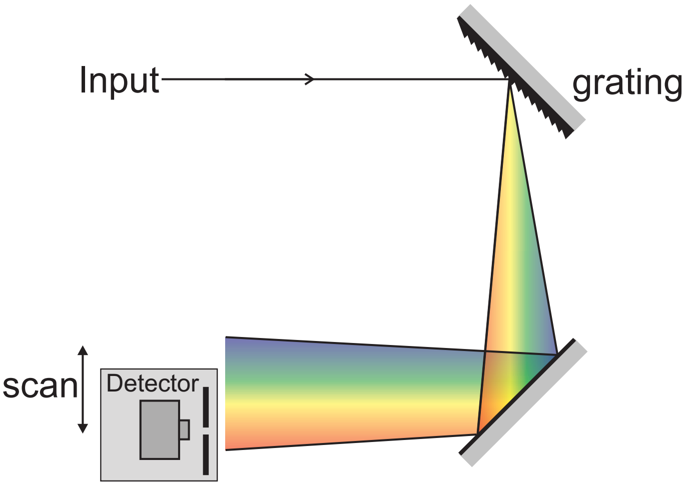

Figure 3.1: Basic layout of a spectrometer

The size and shape of a pulse are somewhat more difficult to measure. For long pulses, photodiodes or sampling oscilloscopes with sufficient bandwidth may be used to map the pulse intensity profile. However these methods often have insufficient bandwidth to measure very short pulses of picosecond or subpicosecond scale. For these short pulses the difficulty comes in finding an event shorter than the pulse duration with which to measure it.

Autocorrelators solve this dilemma by using the short pulse itself as the measuring tool. The basic layout of an autocorrelator is shown in Fig. 3.2. The short pulse is directed onto a beamsplitter to produce two identical copies of itself. One of these passes through a variable path length introducing a delay between itself and its twin. When they are recombined again in the SHG crystal, the overlapping section of the two pulses will form a new pulse at twice the original frequency and with an intensity given by [1],

$$I_{sig}^{SHG}(\tau) \propto I(t)I(t-\tau) \tag{3.1}$$

where τ is the delay introduced between the two pulses. As the delay is varied, we scan through τ giving rise to the detected function

$$A(\tau) = \int_{-\infty}^{\infty} I(t)I(t-\tau)dt \tag{3.2}$$

which is incidently the autocorrelation of the input pulse. Since this is based on the overlap between the two pulses, it can be used to calculate the width of the pulses involved (given that we know the pulse shape). Autocorrelators have proven massively useful, successfully measuring pulses down to the femtosecond scale [2, 3]. However unique pulse shape solutions cannot be deduced from autocorrelations, meaning that the pulse width can only be accurately determined if the pulse shape is already known. In many situations this is not a great limitation as we frequently have some idea what pulse shape is expected. But in other situations, the pulse may have a complicated structure or a fine width measurement is required. For example, if a pulse is measured to have an autocorrelation width of 10 ps, then a Gaussian pulse assumption leads to a deduced pulse width of 7.07 ps, but a sech^2 pulse shape assumption will result in the measured width of 6.48 ps, a 9% difference!

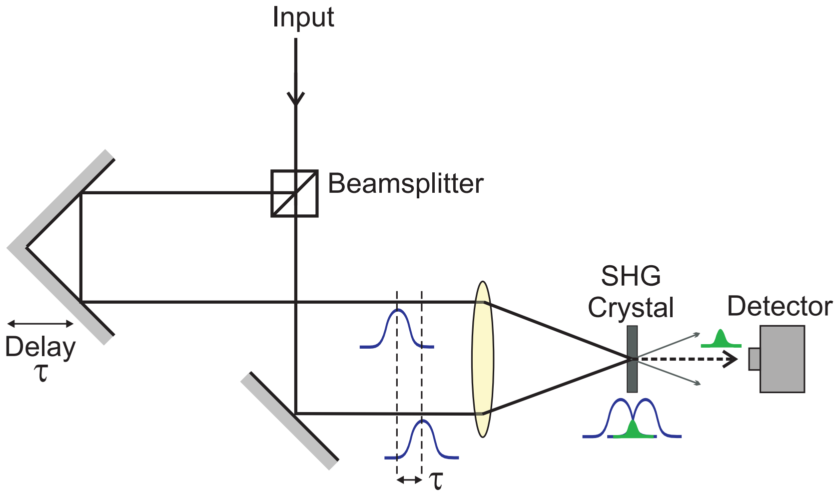

FIGURE 3.2: Basic layout of an autocorrelator

Alternatively, optical sampling oscilloscopes are suitable for more precise determination of pulse shapes. Optical sampling oscilloscopes reduce the bandwidth requirement of detectors by scanning the pulse features over many periods [4]. The concept is shown in Fig. 3.3. A short probe pulse is propagated with the test signal and slightly unsynchronized such that it aligns with a different part of the test signal with each successive period. A nonlinear process such as SFG or FWM between the signal and probe would thus generate a wave at a new frequency, which traces out the signal waveform as the probe walks through it. Slow detection and re-scaling of the new frequency would subsequently reveal the test signal waveform. However, even optical sampling oscilloscopes can only give knowledge of the signal intensity and provides no information as to its phase profile.

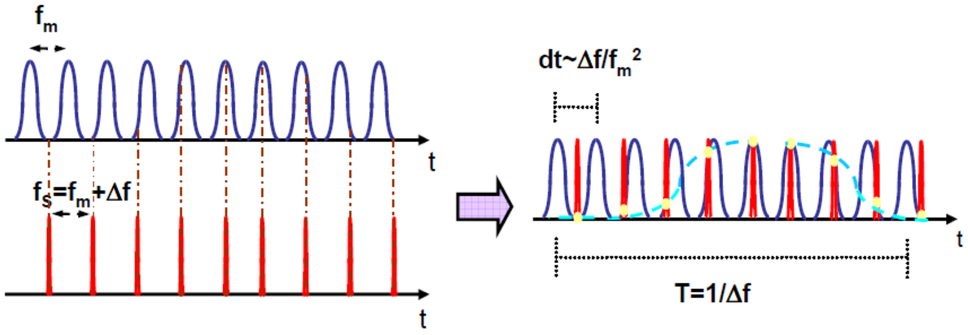

Figure 3.3: Operational concept of an optical sampling oscilloscope.

A group of pulse characterization techniques have demonstrated the capability to not only measure the temporal and spectral intensity of pulses, but also their phase [5–9]. These are clearly of immense interest since we have already established that the phase of a signal links its temporal and spectral domains. This means that knowledge of a signal's intensity and phase in one domain automatically allows one to determine the signal's intensity and phase in the other domain. We can consider pulse phase characterization schemes to fall into 3 general categories: tomographic, interferometric and spectroscopic techniques.

Tomographic techniques are similar in concept to reconstructing a three dimensional object by taking photos of it (a two dimensional projection) from different angles, as shown in Fig. 3.4(a). Fig. 3.4(b) shows the time-frequency equivalent. In this case, the pulse (object) is contained in the time-frequency domains rather than the spatial domain, and is projected from two dimensions (time-frequency) to one (frequency) which can then be measured by a spectrometer. While the use of spectrometers simplify the measurement of the projections, the 'turning' or rotation of the pulse in time-frequency is much less trivial than its spatial analogy. Rotation of a pulse in time-frequency space is achieved by applying a linear chirp similar to a time lens and can be implemented with the same array of techniques as time lenses including phase modulation, XPM, etc.

Then by measuring the spectrum of the signal before and after application of the linear chirp, the initial phase of the signal can be calculated from knowledge of the applied chirp. However, as this technique required a linear chirp, it suffers from some of the same limitations as time lenses, such as having a restricted time window into which the test pulse must fit, thus limiting the applicability of the technique to pulses greater than 20 ps [5].

Interferometric techniques use temporal or spectral interference between two pulses to obtain an interferogram which reflects the phase differences between them. Thus the phase of one pulse can be deduced from knowledge of the other pulse. This scheme is advantageous in that the phase differences are directly measured in the interferogram. Unfortunately, precise knowledge of the probe pulse is not always easily available. To get around this, some interferometric techniques such as Spectral Phase Interferometry for Direct Electric-field Reconstruction (SPIDER) uses self referencing [6]. Fig. 3.5 shows a diagram of how a SHG SPIDER is implemented. An interferometer is used to split the test pulse and recombine it after introducing a delay, τ, to one arm. However, since temporal shearing would produce an interferogram which oscillates too rapidly to be easily measured, the temporal shear needs to be converted into a spectral shear to simplify the measurement. This can be achieved in one of two ways. In a SHG SPIDER, a strongly dispersed pump pulse is coupled with the 'double pulse' and propagated through a $\chi^{(2)}$ crystal such that each of the pulses interacts with a different frequency in the pump. The two emerging pulses are thus spectrally sheared replicas of each other [6]. Alternatively, the temporal-to-spectral shear conversion can also be achieved using the rising and falling linear portions of a sinusoidal phase modulation to oppositely chirp the two

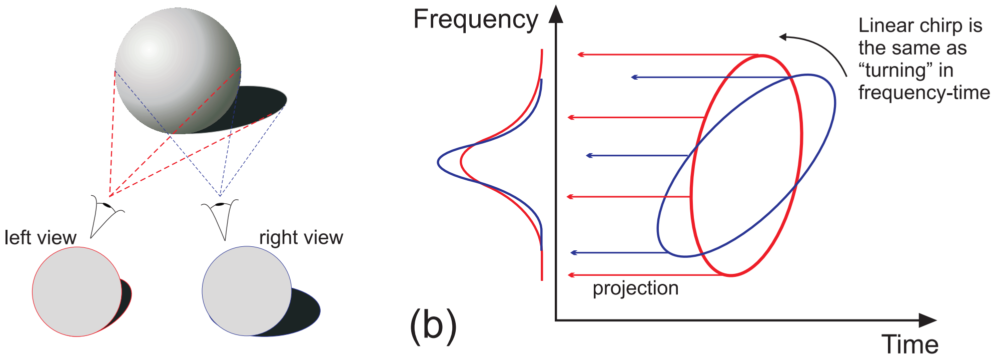

FIGURE 3.4: (a) A 3D object can be reconstructed using two 2D images viewed at different angles. (b) Linearly chirping the pulse effectively 'turns' it in the frequency-time plane so that it can be reconstructed from its projections.

pulses [10]. The spectrally sheared pulses are then detected on a spectrometer forming an interferogram from which the spectral phase is calculated. While the latter technique significantly simplifies the SPIDER and makes it more suitable for telecommunications signals, the necessity of the imparted phase shift to be very linear requires the duty cycle of the measured pulse to be very low. Because of the need for a very dispersed pump or a very linear phase shift, the use of SPIDER for telecommunications signals usually requires the pulse to be gated down to a lower repetition rate. Interferometric techniques are thus often limited, depending on implementation, to regimes that are not practical for telecommunications applications.

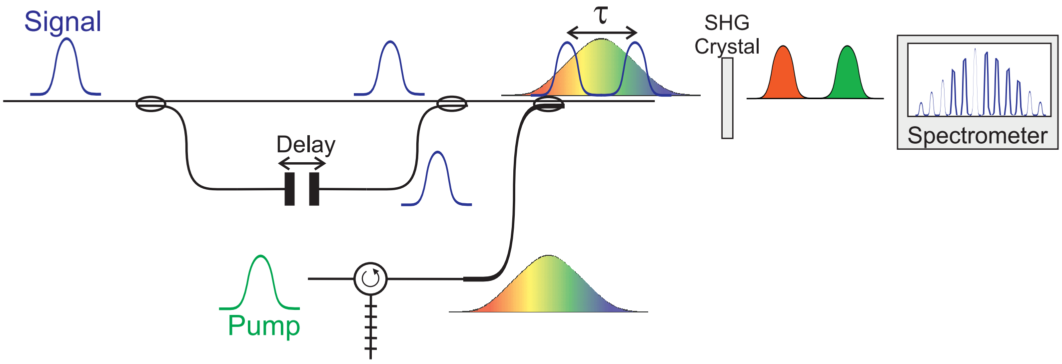

Figure 3.5: Implementation of a SHG SPIDER: The pulse is duplicated with delay τ in an interferometer so that each replica picks up a different spectral shift when mixed with a dispersed pump in the SHG crystal. The two are then measured with a spectrometer to get an interferogram.

Spectroscopic techniques are the most widely used of the three types, despite requiring an iterative deconvolution process to retrieve the signal phase. FROG is perhaps the most common implementation of this technique and was first demonstrated by Kane and Trebino in 1993 [7]. The FROG combines an autocorrelator and an optical spectrum analyzer, both of which individually, can only give information about the temporal or spectral profile of the pulse. However, since phase changes in a signal must manifest in either the temporal or the spectral profile of the pulse, the combination of these two techniques can allow also the pulse phase to be indirectly measured. Instead of just measuring the signal with a detector as a conventional autocorrelator would do, the second harmonic signal in the FROG is detected by a spectrometer, such that the spectral content of the pulses at each delay τ in the autocorrelation is also measured and not just the overlap power. This can be displayed as a spectrogram which shows the pulse intensity as contours on a time versus frequency map, thus indirectly capturing the pulse phase information. The phase information can then be extracted from the spectrogram by performing a two dimensional deconvolution of the spectrogram [1]. The deconvolution algorithm compares the spectrogram from a predicted pulse field to the measured one to calculate an improved pulse field, which is then used as the predicted pulse field in the next iteration. The algorithm can be very effective in recovering not just the pulse shape and spectrum of the pulse, but also its phase information. This retrieval of the signal phase information makes the FROG an essential diagnostic tool when investigating phase manipulation techniques. One drawback to the FROG is its use of the autocorrelation. An autocorrelation is not in general an accurate representation of the actual pulse shape. For instance, it is by definition symmetric while many pulses are not, thus creating ambiguity in the time direction of the retrieved pulses.

To reduce some of these limitations, it was proposed that cross correlation rather than autocorrelation be used in the FROG technique [11]. The retrieval process from cross correlated pulses is more involved requiring a blind deconvolution to retrieve the pulse shapes of two different pulses. That is, the deconvolution is based on initial 'blind' guesses of the two pulses and performed iteratively to converge to a solution. The deconvolution algorithm we used was a variation of the principle components generalized projection algorithm detailed in [12]. Although more involved, the retrieval of the cross correlation can result in a better recovery of both the pulse shapes. This is because the deconvolution of two pulses allows the algorithm more flexibility in prediction, so it is easier to converge to a lower error. Additionally, the detected cross correlation between two different pulses is not necessarily symmetric as in the autocorrelation case, hence removing the direction of time ambiguity. Note that it is also possible to implement cross correlation in a SHG crystal [11], in which case the same recovery algorithm could be used for deconvolution, as long as the differing transfer functions applicable to SHG and EOMs are taken into account.

While the cross-correlation can be implemented in a SHG crystal, using two different pulses gives us the flexibility to consider other gating options. The use of electro-optic modulators (EOM), such as electroabsorption modulators (EAM) or electro-optic Mach-Zehnder modulators (MZM), are one such option [13]. EAMs are semiconductors which use the Franz-Keldysh effect or the quantum-confined stark effect to cause photon absorption that is dependent on applied voltage. Electro-optic MZMs are essentially interferometers which use interference effects to cancel the optical output rather than photon absorption in a semiconductor. Electro-optic crystals such as the commonly used lithium-niobate ($LiNbO_3$) change their refractive indices with applied voltage, and are used in one arm of the interferometer to change the optical path length in that arm. This in turn changes the phase difference between the interferometric arms and cause constructive or destructive interference when they are recombined. Both these mechanisms allow electrical signals to modulate continuous optical waves. If optical pulses are used instead of a continuous wave, the modulator acts to gate the input pulses. Varying the delay of the optical pulses relative to the electrical gate can then be used to form a cross correlation of the two. Since EOMs directly gate the signals without the use of nonlinearities, they have the benefit of being suitable for low power signals. Furthermore, fiberized EOMs are readily commercially available.

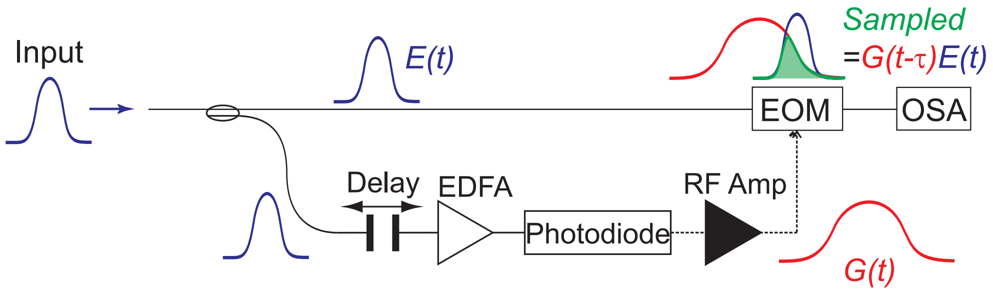

FIGURE 3.6: Layout of our L-FROG pulse characterization setup.

This technique of linearly gating the pulses to make a FROG measurement was originally developed and built at the ORC by M. Roëlens, a previous student [14]. I refer to it as the L-FROG to differentiate it from the more commonly used SHG-FROG which uses signal autocorrelation in a SHG crystal. The basic layout of the L-FROG is shown in Fig. 3.6. The pulse to be measured is split with a coupler to obtain a test pulse $E(t)$, and a separate gate pulse. The gate pulse is passed through a delay line which facilitates the scanning of the gate through the signal and a constant output EFDA to equalise any attenuation fluctuations in the delay line, before being detected with a 20 GHz bandwidth photodetector. The photodetector converts the gate pulse into an electrical gate $G(t)$ which after amplification is used to drive the EOM which actually samples the test pulse. Finally, the sampled signal is measured on a high resolution OSA to form slices of the measured spectrogram. This L-FROG setup is used in the remainder of the thesis for pulse phase characterization and is a valuable tool in our lab. However, alterations are often made to this setup when measuring unconventional or complicated pulses. In almost all cases, the alteration is simply to obtain a gate pulse which is simpler than the test signal. For example, gate pulses are often split from a signal before it enters the system under test or from an entirely different source which is synchronized with the source of the test signal.

The rest of this chapter presents experiments we have performed which use the L-FROG to measure interesting pulses. They have been selected to show the versatility of our L-FROG setup to measuring a wide range of signals from sub-picosecond widths in the first experiment which is a pulse compression scheme (Section 3.2) to dark pulses in the second experiment that were tens of picoseconds long and generated using a semiconductor optical amplifier based wavelength converter (Section 3.3). Other interesting pulse types have also been characterized throughout this work, in particular the output of a frequency comb generator studied in Chapter 6 is of great interest.

3.2 Characterization of Pulse Compression in a Bismuth-Oxide Fibre

In this section we present a pulse compression experiment using a highly nonlinear Bismuth-Oxide fibre. Two main aims are addressed in this experiment. The first is to demonstrate strong pulse compression resulting in sub-picosecond transform limited pulses at 10 Gb/s. The second purpose is to test the L-FROG pulse measurement system using different linear modulators. The pulse compression scheme presented here, uses SPM occurring in the highly normally dispersive, nonlinear Bismuth-Oxide fibre to cause spectral broadening. Pulse compression occurs at a second (linear) stage which removes the pulse chirp by propagation in a piece of single mode fibre. These experiments were taken in collaboration with S. Asimakis.

3.2.1 Background

The generation of short pulses has always been of interest, whether it be used to develop ultrahigh bandwidth communications, measurement systems or for a range of other applications [15–19]. While short pulse laser sources have been able to achieve extremely short pulse durations at low repetition rates [20], obtaining sub-picosecond pulses at GHz repetition rates simply, remains a challenge. Pulse compression schemes attempt to achieve this by starting with wider pulses at the desired repetition rate and then nonlinearly compressing them down to narrower widths. Pulse compression can be achieved using nonlinear effects such as FWM and SPM. FWM can be used to compress pulses by providing an intensity dependent gain in a similar way to saturable absorbers in lasers [21]. FWM occurring between a pulsed pump and a synchronized signal, provides the signal a large gain at the peak of the pump pulses and much less gain at the sides. This acts to 'shave away' the sides of the pulse leaving it narrower. While this scheme has the advantage of also providing the signal large gains, it requires synchronization and careful polarisation control between the signal and pump and requires the initial pulse to already be short.

To avoid these complications, SPM methods of pulse compression are often preferred due to their simplicity. No other signals are required and the signal acts as its own 'pump'. As we saw in Section 2.3.3, Pulses undergo SPM when their powers are high enough to induce the nonlinear Kerr effect which, through analysis of the nonlinear Schrödinger equation [22], can be shown to modulate the signal's phase in an intensity dependent manner. The SPM induced phase shift, ϕ_{NL}, is given by [22]

$$\phi_{NL}(T) = \gamma P_0 L I(T) \tag{3.3}$$

where P_0 is the initial peak power of the pulse, $I(T)$ is the normalised intensity profile of the pulse. This intensity dependence of the phase causes a chirp to occur at the leading and trailing edges of the pulse which is given by

$$\delta\omega = -\frac{\mathrm{d}\phi}{\mathrm{d}T} = -\gamma P_0 L \frac{\mathrm{d}I}{\mathrm{d}T}. \tag{3.4}$$

Thus for pulses which are initially already short with high peak powers, the intensity gradient is steep giving rise to a large chirp and new frequencies are generated. SPM schemes largely differ in their choice of nonlinear medium. These generally fall into two categories, those with anomalous dispersion ($\beta_2 < 0$) and those using normal dispersion ($\beta_2 > 0$). If the nonlinear fibre in which SPM occurs has anomalous dispersion then the blue-shift occurring at the leading edge of the pulse is delayed with respect to the red-shifted components at the trailing edge thus keeping the pulse compressed without other action. This self compression is the simplest scheme and is the same mechanism by which solitons can be created. Dispersion decreasing fibers are often used as the nonlinear medium in these regimes [23] to adiabatically guide the pulse into narrower soliton solutions. However, the fabrication of such high quality dispersion decreasing fibers is non-trivial. Alternatively, fibers have been fabricated with sections of alternating SMF and dispersion shifted fibers spliced together. These create sections of controlled dispersion which are reduced in each subsequent section to effectively create the same effect as the dispersion decreasing fibers with much simpler fabrication [24].

In the normal dispersion regime, the wavelengths generated at the leading and trailing edges of the pulse actually move *away* from each other and so must be brought together externally by a grating pair, a length of anomalously dispersive fibre or some other form of controlled opposing dispersion. Although less simple than the anomalous dispersion regime, the normal dispersion actually acts to stretch and linearize the chirp generated by the SPM. The chirp is then able to be more completely compensated for by the external dispersion resulting in better pulse quality at the output. The nonlinear media chosen in this regime vary greatly from SMF or dispersion shifted fibers used in the normal regime [2, 25, 26] to highly nonlinear doped fibers [27], microstructured fibers [28, 29] and specialized gratings [30]. In Ref [31], Fu *et al.* used a chalcogenide soft glass fiber to compress 6 ps pulses down to 420 fs. The external chirp compensation here was achieved with a dispersive grating written for the purpose. Although very good pulse quality was able to be achieved in this case, the compressed pulse train was obtained at a 9 MHz repetition rate which is much lower than appropriate for telecommunications applications. Furthermore, the use of chalcogenide fibre limits the maximum input power into the fibre if the onset of two photon absorption is to be avoided. Two photon absorption would increase the fibre losses, thus degrading the performance of the compressor. Hence, the scheme is not suitable to be power scaled for increased compression.

In this experiment, our aim was to produce short sub-picosecond pulses at high repetition rates. To do this, we chose to use a SPM-based compression scheme in the positive GVD regime. Our nonlinear medium was a 2 m length of highly nonlinear Bismuth-Oxide doped single mode fibre, chosen for its very high effective nonlinear coefficient of $\gamma \simeq 1100\mathrm{W}^{-1}\mathrm{km}^{-1}$ and high normal dispersion of $\mathrm{D} = -252$ ps/nm/km at telecommunications wavelengths [32]. The high nonlinear coefficient meant that we were able to achieve significant pulse broadening with only a very short length of fibre, thus avoiding possible synchronisation issues when using the resulting pulses in further applications. Meanwhile, the large normal dispersion of the fiber at telecommunications wavelengths is effective at linearizing the large chirp induced by this high nonlinearity, thus improving the final compressed pulse quality. Again, this makes the resulting pulses advantageous for use in other applications.

3.2.2 Experiments

The SPM based pulse compression scheme was set up to operate at approximately 10 GHz. As well as demonstrating pulse compression, we wanted to test in this experiment the ability of the L-FROG to measure very short pulses. The pulse compression experimental setup is shown in Fig. 3.7. Our source was an erbium-doped mode locked laser (PriTel Ultrafast Optical Clock) driven by a 9.935 GHz clock to produce 2.5 ps sech^2 pulses. The pulses were generated at a wavelength of 1549.3 nm and an average power of 6 dBm. They were then amplified up to 25 dBm in a high power EDFA. The resulting pulses were approximately 1.3 ps wide (FWHM) due to some initial negative GVD pulse compression occurring inside the amplifier. Fig. 3.8 shows the initial pulse characteristics before propagation in the highly nonlinear fibre. It is evident from Fig. 3.8(a) that the input pulse has a nearly zero chirp and is close to transform limited. Its corresponding spectrum is shown in Fig. 3.8(b) and is noted to have a 3-dB bandwidth of 1 nm.

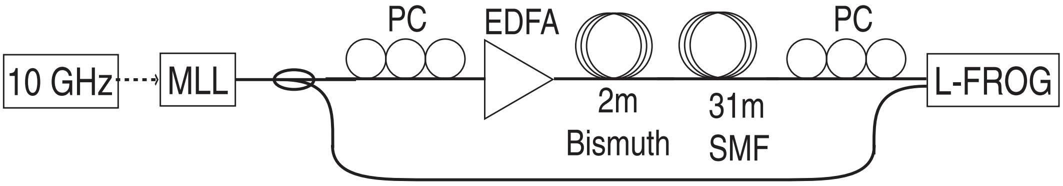

FIGURE 3.7: The pulse compression setup.

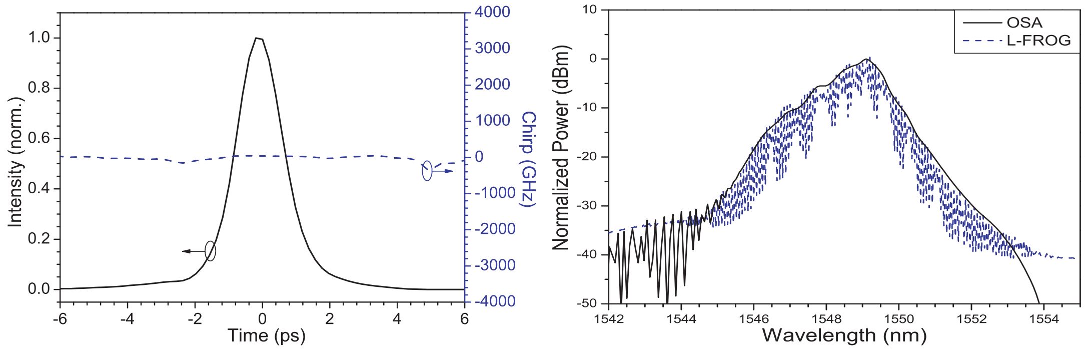

(a) **(b)**

FIGURE 3.8: (a) The pulse emerging from the amplifier is 1.3 ps in width with a near-zero chirp. (b) The spectrum of the amplified pulse.

By passing our amplified pulses through this highly nonlinear medium, they undergo severe SPM, acquiring a large chirp and spectral broadening. The high dispersion of the Bismuth fibre then stretches out the chirp, linearizing it as discussed in Section 3.2.1. The resulting temporal pulse is shown in Fig. 3.9(a) and the output spectrum broadened from 1 to 12 nm is shown in 3.9(b). The characterisation of the pulses was obtained with L-FROG measurements and compared to both numerical simulations of our system and independent measurements of the pulse spectra with an optical spectrum analyzer. The temporal pulse can be seen to be square-ish as expected and that the emerging chirp is indeed large and fairly linear, spanning ±1000 GHz across the 8.5 ps width of the pulse. However, the temporal pulse is also shown to exhibit large ripples along the top edge and there are deeper oscillations in the spectrum that was predicted by our simulations which are likely to be correlated to the temporal discrepancies. The origins of these unexpected ripples were not able to be precisely determined. However, we suspect that they could possibly result from back reflections at the Bismuth-SMF splice interfaces which had ≈ 3 dB loss each.

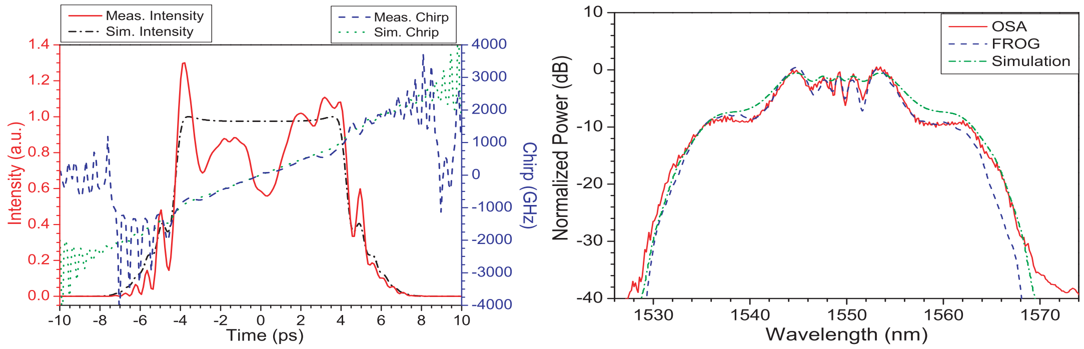

(a) **(b)**

FIGURE 3.9: (a) The L-FROG retrieval of the signal pulse after the Bismuth fibre is shown compared to simulation. (b) Good correlation is shown between the simulated, retrieved and independently measured spectra.

To compensate for the chirp and complete the compression of the pulse, the highly chirped and spectrally broadened pulse was then passed through anomalously dispersive SMF fibre. The L-FROG system was valuable here to aid the optimisation of the system. To obtain a transform limited output, the exact length of compensating SMF (to within half a meter) had to be chosen. Being able to measure the phase of the output allowed us to determine whether too much or too little SMF was being used. Through fine tuning with the L-FROG, we found that 31 m of SMF gave the best pulse we could obtain for this level of amplification. The resulting output pulse, shown in Fig. 3.10(a), was now

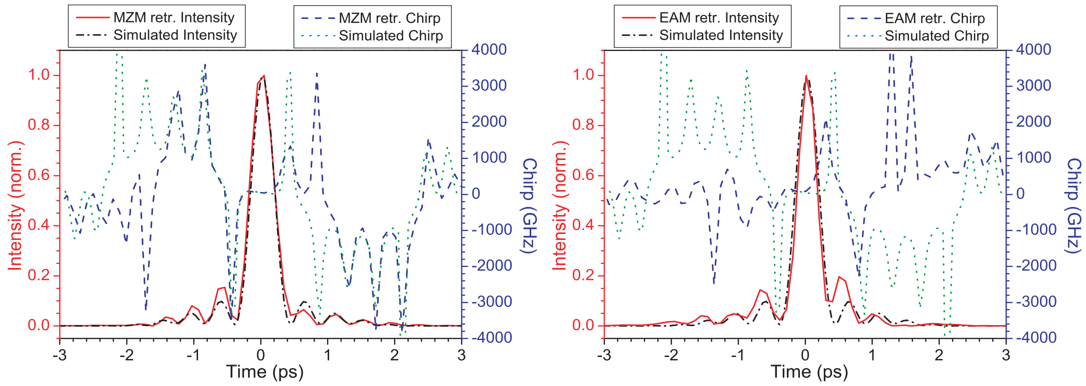

(a) **(b)**

FIGURE 3.10: The phase (dash-dot) and intensity (solid line) profile of the compressed signal pulse as retrieved by (a) the MZM-FROG and (b) the EAM-FROG.

only 402 fs in duration and had an extremely flat chirp indicating that it was transform limited. The L-FROG retrieval is again compared to numerical simulations and shown to have a very good match. Thus, we believe we have successfully demonstrated the compression of 1.3 ps pulses to 402 fs at 9.953 GHz.

To achieve our second aim of testing the capability of the L-FROG, the pulse was measured using two different modulators, an EAM and a MZM. The EAM has typically been the modulator of choice to use with the L-FROG [13]. It possesses a steeper gating function than the MZM thus providing a narrower gate and better gate extinction. In addition, it is largely polarisation insensitive which eliminates the need for a polarisation controller, which is not the case with MZMs. However, the use of the MZM has its own benefits as we see below. In the first instance, the pulse was measured using a lithium niobate MZM in the L-FROG. This is the measurement retrieval seen in Fig. 3.10(a) and has a good agreement with simulation as noted above. Fig. 3.10(b) shows the repeat measurement taken with an EAM. It is clear that the EAM measurement retrieval shows a poorer match to simulations. The inferiority of this measurement is even more evident in Fig. 3.11 which compares the simulated and retrieved spectra to the spectrum independently measured with the OSA. While the simulations and the MZM retrieval both show a decent match to the OSA spectrum, the EAM retrieved spectrum can be clearly seen to be skewed. The skewing corresponds to the cutoff of the semiconductor in the modulator near 1540 nm. These measurements highlight the benefits of using a MZM when measuring broadband signals. The femtosecond scale pulses measured here are the shortest and most broadband pulses we have attempted with the L-FROG. As such we have found that for pulses of this type, our traditional choice of using EAMs to perform gating in the L-FROG is inappropriate.

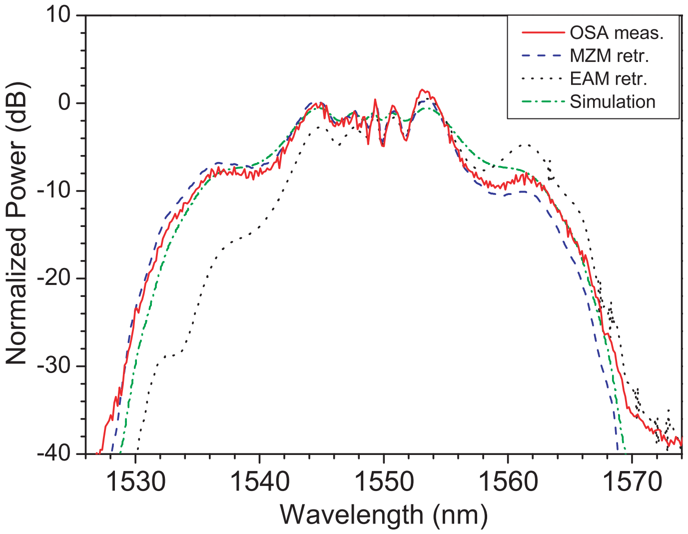

FIGURE 3.11: Comparison of the measured and retrieved spectra for the two modulators.

3.2.3 Conclusions

We have successfully obtained 402 fs compressed pulses by use of SPM in a HNLF and a length of anomalous dispersion fibre. The pulses were obtained at a 9.935 GHz repetition rate and were shown to be very nearly transform limited. Furthermore, we have used these compressed pulses to demonstrate the characterising capability of the L-FROG system. Measurements of the pulses were taken with the L-FROG using different modulators and show the superiority of the lithium niobate MZM over the EAM as a result of its wider optical bandwidth. In practice, the MZM is advantageous because it is more robust electrically and has a higher tolerance for excessive voltage increases. However disadvantages of the MZM include its polarisation sensitivity, introducing the need for polarisation control preceding the modulator. Care must be taken that the extra dispersion in the polarisation controller is taken into account when choosing to use the MZM. Additionaly the MZM is unable to provide as much extinction ratio (ER) in gating as can be obtained from the EAM ($\mathrm{ER_{MZM}} \sim 20$ dB compared to $\mathrm{ER_{EAM}} \sim 30$ dB). Nevertheless, we have used the MZM for all the L-FROG measurements presented in this thesis (except for the parabolic pulses shown in Fig. 5.8), and although the polarisation sensitivity was inconvenient, neither it nor the ER were found to be limiting.

3.3 Measurement of Semiconductor Optical Amplifier Responses

In this section, we measure the response of semiconductor optical amplifiers (SOA) to short optical pulses. This demonstration shows the applicability of L-FROG techniques to the characterization of active devices and also of dark pulses. The work was carried out in collaboration with A. Perez-Pardo and S. Sales from the ITEAM Research Institute of the Universidad Politécnica de Valencia. The SOAs we measured were provided by the ITEAM Research Institute and packaged into a Mach-Zehnder Interferometer (MZI) device. Using the SOA-MZI in a pump-probe configuration, we have investigated both the cross gain modulation (XGM) and cross-phase modulation (XPM) response to short pump pulses. These experiments were undertaken at the ORC primarily by myself, with the assistance of A. Perez. While we at the ORC provided the expertise on the characterisation of the device, the majority of the expertise regarding analysis of SOA gain dynamics was obtained from our collaborators at ITEAM. Together, we endeavored to assist in the understanding of nonlinear behaviour of SOA devices by measuring their response, which should aid the optimisation of these versatile devices.

3.3.1 Background

SOAs are of considerable interest as nonlinear optical processing devices, since they can be used for operations such as signal regeneration and wavelength conversion. To understand the response of SOA devices, we need to understand its gain dynamics, which are determined by the movement of free carriers in the valence and conduction bands of the SOA. The effects can largely be considered in terms of the quickly reacting intraband transitions versus the slowly reacting interband transitions. Depending on the width of the pulses we input into the SOA, the dominating effect changes, thus changing the gain dynamics. When the SOA is operated using short pulses (on the order of a few picoseconds), the intraband effects dominate and the saturation energy of the output pulse becomes pulse width dependent [33]. The shorter the pump pulses, the larger the compression associated with the intraband effects [34]. In the case of longer pulses, the slow gain compression would be much larger because of the much higher contribution of the interband effects on the SOA saturation [33]. In order to use the SOA intraband fast dynamics for high speed applications, the slow gain compression should be kept as small as possible because of its slower dynamics. Using sub-picosecond pulses it is possible to keep the slow gain compression small, even for input pulse energies higher than the saturation energy.

All-optical processing of signals in SOAs usually employs either XGM or XPM. In the latter case, it is common to use integrated SOA Mach-Zehnder interferometers (SOA-MZI) in order to convert phase changes into intensity variations. As the signal repetition rates approach the operating bandwidth of the SOA devices, precise knowledge of the response of the devices (in both intensity and phase) becomes ever more crucial. Previous measurements of fast SOA phase responses have either involved measurements of the alpha factor, which relates the refractive index change with any induced gain or absorption changes in the SOA [33, 35], or used interferometric set-ups [36]. While the alpha characteristic is a useful indicator, it does not provide a detailed appreciation of the phase profile of the SOA response. Interferometric setups on the other hand, can be quite involved and are prone to environmental instabilities. The high sensitivity, high stablility and all-fiberised implementation of the L-FROG, makes it particularly attractive for the characteriastion of theses signals.

3.3.2 Experimental Setup

The SOA response measurements were made on two 1 mm long SOAs arranged in a five port SOA-MZI (model 07.4059.LI1.WSP08 from Heinrich Hertz Institut), as shown at the top of Fig. 3.12. A gain-switched DFB laser (GSL) was used as the signal source to produce 1551 nm pulses at 10 GHz followed by a length of dispersion compensating fibre to compensate for the chirp of the generated pulses. Details of the GSL can be found in Appendix A. A MZM driven with an alternating bit pattern was then used to halve the repetition rate of the pulse train from 10 GHz down to 5 GHz. The lower repetition rate was chosen to allow the SOAs sufficient recovery time and thereby to avoid patterning effects. The 5 GHz pulse train was then split into two arms, one of which became the pump signal into the SOA-MZI. At launch into the SOA-MZI, the pump pulses were 4.5 ps (FWHM) and had a time-bandwidth product of 0.66. A second CW laser signal at 1540.6 nm acted as the probe to the SOA-MZI and its output was measured by the L-FROG. Note that since the L-FROG performs a spectral measurement, we can choose an appropriate wavelength range on the optical spectrum analyser (OSA) to measure the signal without requiring an additional optical filter to remove the pump.

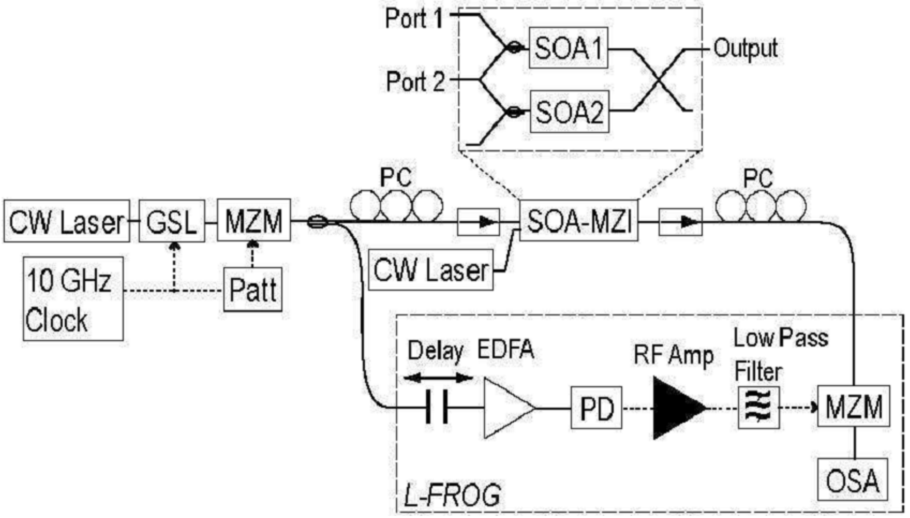

Figure 3.12: Experimental setup of the SOA-MZI characterisation.

3.3.3 Cross-Gain Modulation Measurements

We performed measurements of XGM in the SOA by illuminating only SOA1 of the MZI-SOA (see Fig. 3.12). At the output, the amplitude and phase of the XGM carved and converted probe pulses were measured using the L-FROG system. Fig. 3.13 shows a measurement of the probe output for an average input power of -10 dBm. The 5 GHz lines of our pulse train can be clearly seen stretching across the spectrogram as can the broadened spectrum on the leading and trailing edges. Fig. 3.14 shows the intensity and phase profile of the converted pulses when the pump pulses had an average power of -10 dBm. An inverted converted signal, typical of the XGM process can clearly be observed. The phase profile shows that there is a large red shift (negative chirp) associated with the steep leading edge of the pulse and a smaller blue shift (positive chirp) associated with the shallow trailing edge of the pulse as a result of the slow response time. These phase changes arise from the nonlinear refractive index variations in the amplifier, which result in a chirp [33]. Similar intensity and phase profiles were obtained for different average pump input powers from -13 to -6 dBm (1.5, 2.5, 4, 6, 8 and 10 mW peak powers). The intensity profiles can be seen in Fig. 3.15(a). Note that the plots are normalized with respect to the maximum power of the probe signal at the output of the SOA. The total gain compression is the ratio of the unsaturated probe level to the minimum of the probe transmission. As expected, both total and slow gain compression increases with increasing pump energy which is in agreement with the theory [33]. The increase in total gain compression is mainly due to the increase of the

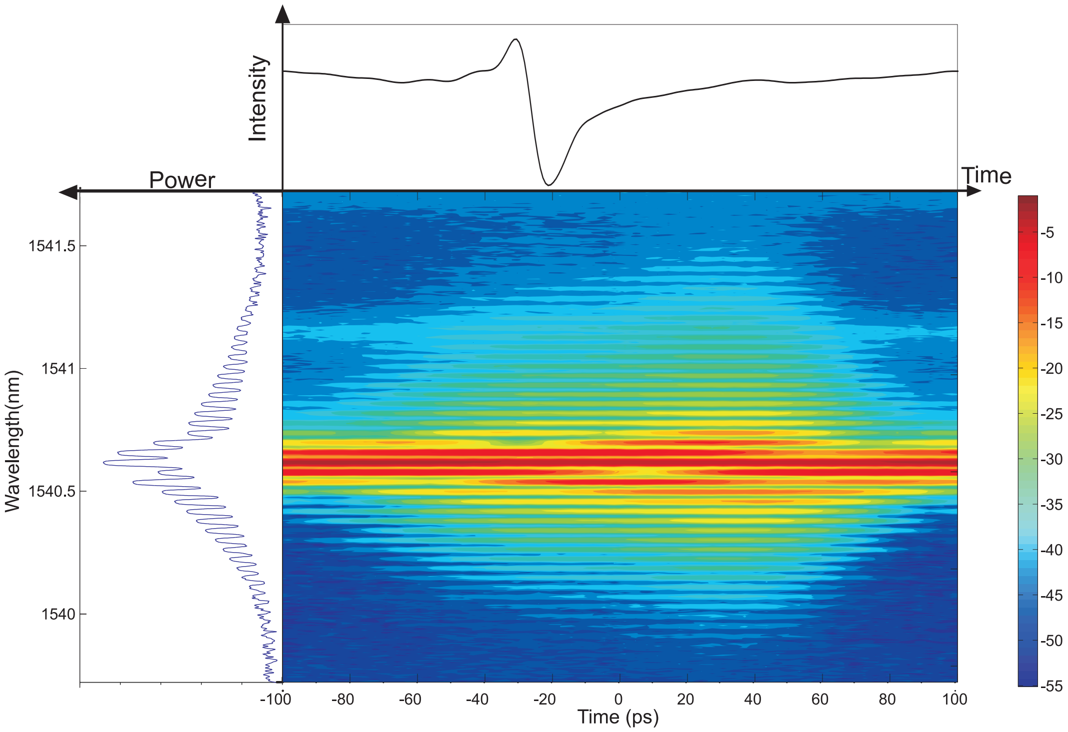

FIGURE 3.13: Measured spectrogram for pump power = -10 dBm.

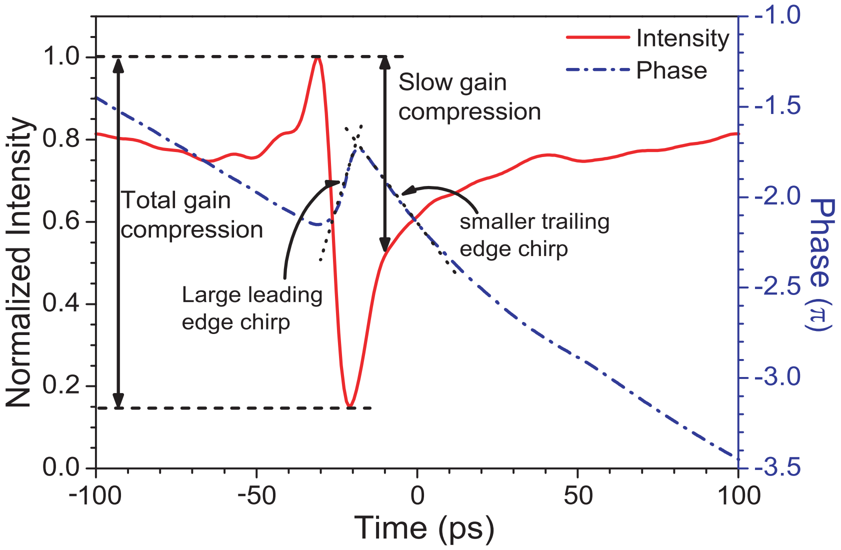

FIGURE 3.14: Measured intensity and phase for pump power = -10 dBm.

plasma temperature in the active region, which is caused by the increase in pump energy. However, the slow gain compression increases because of the reduced carrier density due to the increasing stimulated emission.

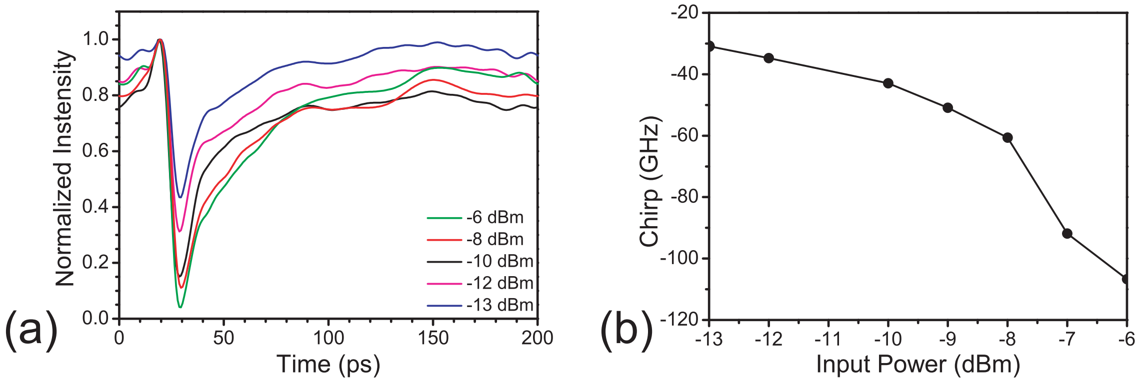

FIGURE 3.15: (a) Measured probe transmission pulses for different pump powers. (b) Maximum (leading edge) chirp for XGM at different pump powers.

After compression induced by the pump, the gain shows a fast recovery, resulting from intraband effects, mainly carrier heating and spectral hole burning. Faster effects, like two photon absorption would only play a main role for shorter pulses (fs). After the fast gain recovery, the gain recovers slowly toward the unsaturated value as a result of electrical pumping. This interband recovery becomes shorter for longer SOA devices and for higher electrical bias currents [33]. Typical values for the 10%-90% recovery time are less than 50 ps for 2500 μm long, strongly biased SOAs, and up to 1 ns for shorter SOAs (250 μm). Since the period of the signal in our measurements was 200 ps, at low powers, the gain was able to fully recover to its unsaturated value in the 1 mm long SOA devices that we experimented with. Fig. 3.15(b) shows the peak chirp experienced by the pulse for increasing pump powers. We note that the peak chirp gradually increased from -30 GHz to -105 GHz due to carrier induced index changes. Since the recovery time due to intraband effects is affected by the input power, we have a variation of 75 GHz in the maximum observed chirp for 7 dB variation in power input. These and the previous results are in agreement with characterisation measurements obtained using different techniques [33].

3.3.4 Cross-Phase Modulation Measurements

Having measured the response of a single SOA, we can measure the XPM characteristics of the SOA by using the wavelength-converted pulses in a Mach-Zehnder interferometric configuration. To do this, the input pulses were generated in the same way as for the XGM case, but we now operate the SOA-MZI with both SOAs active. The XPM in SOA1 can then interfere with the CW output from SOA2, and be converted to intensity modulation. Thus at the output of the SOA-MZI we obtain pulses which are primarily dependent on the XPM in SOA1, but also receive some shaping from the gain compression. In this part of our experiment, SOAs 1 and 2 were operated at current values of $I_1 = 300$ mA and $I_2 = 160$ mA, respectively. These currents were selected for out-of-phase operation of the SOA-MZI to give inverted pulses. This mode of operation yields an opposite sign in the frequency chirp of the converted signal to that obtained when the device is operated in the in-phase operation mode. Fig. 3.16(a) shows the L-FROG measured intensity profiles of the SOA-MZI output pulses. Average input peak powers between -10 and -4 dBm (3.8, 4.5, 6, 8 and 10 mW peak powers) were used to see the phase and amplitude dependence of the wavelength converted output on input pump energy. We observe that as in the XGM case, both the total and slow gain compression increase with increasing pump energy. Likewise in Fig. 3.16(b), the chirp of the output pulses is shown to increase with increasing pump energy. Further, comparing the amount of frequency chirp induced in the probe signal at the output of the SOA-MZI to that measured after XGM only, we note that the chirp at the output is much lower than that observed in XGM. This difference here is due to the interference at the output and is

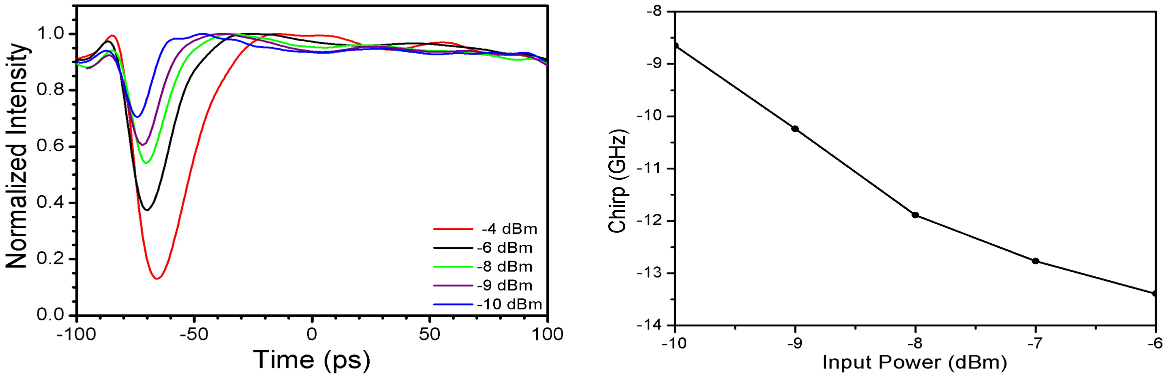

(a) (b)

FIGURE 3.16: Measured SOA-MZI output pulses for different average pump powers. (b). Maximum (leading edge) chirp of the output pulses for different pump input powers.

consistent with the theory presented in [37]. Since the output of the MZI is given by the difference between the fields of the two arms, the maximum chirp excursion is reduced. As a result, XPM in the Mach-Zehnder configuration produces pulses with lower chirp than XGM alone and so is more favourable for switching applications.

3.3.5 Conclusions

We have performed XGM and XPM characterisation measurements of 1 mm long SOAs operated in a single SOA and in Mach-Zehnder configurations respectively. We have fully characterized the dynamic response of the SOA-MZI to short picosecond pulses at 5 GHz using a L-FROG system employing a fast $LiNbO_3$ MZM as the sampling gate. Our measurements demonstrate the applicability of the L-FROG technique for the characterisation of the dynamic response of fast optical devices, providing full phase and intensity profiling with good stability.

3.4 Conclusions

We have described in this chapter a complete signal characterization technique based on the FROG technique. The technique uses linear gating in an EOM to achieve a cross-correlation with the signal rather than an autocorrelation in a SHG crystal. The fiberized form of this technique makes it more robust than its nonlinear parent. Additionally, the use of cross-correlation enables the measurement of more complex pulses as was demonstrated in Section 3.3. However, the L-FROG is not without its limitations and the choice of a particular L-FROG configuration is dependent on the signal to be measured. These considerations include the choice of EOM as discussed in Section 3.2 which depends on the bandwidth and dispersion sensitivity of the signal. Also, the time and frequency resolutions of the measurement is traded-off against the measurement time, which may be crucial for unstable or drifting signals. The magnitude of this trade off is then dependent on the specifications of the spectrometer and delay line used. Finally, the choice of the gate pulse is important in leading to a speedy and accurate deconvolution. The gate pulse should ideally be simple in structure, stable and have a pulse width significantly different from the pulse to be measured. While L-FROG measurements can still be obtained for signal and gate pulses of similar widths, such a situation can 'confuse' the deconvolution process causing signal pulse features to sometimes be found on the retrieved gate profile and vice versa.

The L-FROG technique has been demonstrated in this chapter to be useful in characterizing pulses with unusual profiles. We have studied the characterisation of both sub-ps pulses and dark pulses generated in SOA-MZIs. L-FROG has proven to be an essential tool throughout this project for system optimisation, the analysis of phase manipulation schemes and the characterisation of more exotic pulse shapes. Most notably, pulses with parabolic intensity profiles will be presented in the following chapters.

Bibliography

[1] R. Trebino. *Frequency-Resolved Optical Gating: The Measurement of Ultrashort Laser Pulses.* Kluwer Acedemic Publishers, 2002.

[2] J. A. R. Williams, I. Bennion, and L. Zhang. The compression of optical pulses using self-phase-modulation and linearly chirped Bragg-gratings in fibers. *IEEE Photonics Technology Letters*, 7(5):491–493, 1995.

[3] M. D. Pelusi and H.-F. Liu. Higher order soliton pulse compression in dispersion-decreasing optical fibers. *IEEE Journal Of Quantum Electronics*, 33(8):1430–1439, 1997.

[4] P. A. Andrekson. Picosecond optical sampling using four wave mixing in Fiber. *Electronics Letters*, 27(16):1440–1441, 1991.

[5] C. Dorrer and I. Kang. Complete temporal characterization of short optical pulses by simplified chronocyclic tomography. *Optics Letters*, 28(16):1481–1483, 2003.

[6] C. Iaconis and I. A. Walmsley. Spectral phase interferometry for direct electric-field reconstruction of ultrashort optical pulses. *Optics Letters*, 23(10):792–794, 1998.

[7] D. J. Kane and R. Trebino. Characterization of arbitrary femtosecond pulses using refquency-resolved optical gating. *IEEE Journal Of Quantum Electronics*, 29(2): 571–579, 1993.

[8] J. Prawiharjo, K. Gallo, B. C. Thomsen, M. A. F. Roelens, P. J. Almeida, N. G. R. Broderick, and D. J. Richardson. Frequency-resolved optical gating in a quasi-phase-matched LiNbO3 waveguide. *IEEE Photonics Technology Letters*, 17(4):849–851, 2005.

[9] P. O'Shea, M. Kimmel, X. Gu, and R. Trebino. Highly simplified device for ultrashort-pulse measurement. *Optics Letters*, 26(12):932–934, 2001.

[10] C. Dorrer and I. Kang. Highly sensitive direct characterization of femtosecond pulses by electro-optic spectral shearing interferometry. *Optics Letters*, 28(6):477–479, 2003.

[11] K. W. DeLong, R. Trebino, and W. E. White. Simultaneous recovery of two ultrashort laser pulses from a single spectrogram. *Journal Of The Optical Society Of America B-Optical Physics*, 12(12):2463–2466, 1995.

[12] D. J. Kane. Recent progress toward real-time measurement of ultrashort laser pulses. *IEEE Journal Of Quantum Electronics*, 35(4):421–431, 1999.

[13] C. Dorrer and I. Kang. Simultaneous temporal characterization of telecommunication optical pulses and modulators by use of spectrograms. *Optics Letters*, 27(15): 1315–1317, 2002.

[14] B. C. Thomsen, M. A. F. Roelens, R. T. Watts, and D. J. Richardson. Comparison between nonlinear and linear spectrographic techniques for the complete characterization of high bit-rate pulses used in optical communications. *IEEE Photonics Technology Letters*, 17(9):1914–1916, 2005.

[15] M. Saruwatari. All-optical signal processing for terabit/second optical transmission. *IEEE Journal on Selected Topics in Quantum Electronics*, 6(6):1363, 2000.

[16] C. X. Yu, H. A. Haus, and E. P. Ippen. Gigahertz-repetition-rate mode-locked fiber laser for continuum generation. *Optics Letters*, 25(19):1418–1420, 2000.

[17] C. X. Yu, H. A. Haus, and E. P. Ippen. Soliton squeezing at the gigahertz rate in a Sagnac loop. *Optics Letters*, 26(10):669–671, 2001.

[18] J. A. Valdmanis and G. Mourou. Subpicosecond electrooptic sampling: principles and applications. *IEEE journal of quantum electronics*, QE-22(1):69–78, 1986.

[19] B. B. Hu and M. C. Nuss. Imaging with terahertz waves. *Optics Letters*, 20(16): 1716–1718, 1995.

[20] W.-W. Hsiang, C.-Y. Lin, M.-F. Tien, and Y. Lai. Direct generation of a 10 GHz 816 fs pulse train from an erbium-fiber soliton laser with asynchronous phase modulation. *Optics Letters*, 30(18):2493–2495, 2005.

[21] T. Yamamoto and M. Nakazawa. Active optical pulse compression with a gain of 29.0 dB by using four-wave mising in an optical fiber. *IEEE Photonics Technology Letters*, 9(12):1595–1597, 1997.

[22] G. P. Agrawal. *Nonlinear Fiber Optics.* Optics and Photonics. Academic Press, third edition, 2001.

[23] M. L. V. Tse, P. Horak, J. H. V. Price, F. Poletti, F. He, and D. J. Richardson. Pulse compression at 1.06 mm in dispersion-decreasing holey fibres. *Optics Letters*, 31(23):3504–3506, 2006.

[24] J. Wang, Y. Wu, C. Lou, and Y. Gao. Pedestal-free 10GHz pulse compression using comb-like dispersion prifiled fibers and its application in 40-Gb/s OTDM systems. *Optical Engineering*, 42(8):2380–2383, 2003.

[25] S. W. Chan, K. K. Chow, and C. Shu. Spectral filtering from a self-phase modulated signal for all-optical pulse compression and reshaping. pages 113–114, 2003.

[26] K. Tai and A. Tomita. 50x optics fiber pulse compression at 1.319 mm. *Applied Physics Letters*, 48(5):309–311, 1986.

[27] J. T. Gopinath, H. M. Shen, H. Sotobayashi, E. P. Ippen, T. Hasegawa, and T. Nagashima. Highly nonlinear bismuth-oxide fiber for supercontinuum generation and femtosecond pulse compression. *Journal Of Lightwave Technology*, 23(11):3591–3596, 2005.

[28] S. Lako, J. Seres, P. Apa, J. Balazs, R. S. Windeler, and R. Szipocs. Pulse compression of nanojoule pulses in the visible using microstructure optical fiber and dispersion compensation. *Applied Physics B-Lasers And Optics*, 76:267–275, 2003.

[29] B. Schenkel, R. Paschotta, and U. Keller. Pulse compression with supercontinuum generation in microstructure fibers. *Journal Of The Optical Society Of America B-Optical Physics*, 22(3):687–693, 2005.

[30] G. Lenz, B. J. Eggleton, and N. Lichinister. A pulse compressor based on self-phase modulation in a fiber Bragg grating. In *Conference on Lasers and Electro-Optics (CLEO)*, page 165, 1998.

[31] L. Fu, A. Fuerbach, I. C. M. Littler, and B. J. Eggleton. Efficient optical pulse compression using chalcogenide single-mode fibers. *Applied physics Letters*, 88(8), 2006.

[32] F. Parmigiani, S. Asimakis, N. Sugimoto, F. Koizumi, P. Petropoulos, and D. J. Richardson. 2R regenerator based on a 2-m-long highly nonlinear bismuth oxide fiber. *Optics Express*, 14(12):5038–5044, 2006.

[33] L. Schares, C. Schubert, C. Schmidt, H. G. Weber, L. Occhi, and G. Guekos. Phase dynamics of semiconductor optical amplifiers at 10-40 GHz. *IEEE Journal of Quantum Electronics*, 39(11):1394–1408, 2003.

[34] K. L. Hall, G. Lenz, A. M. Darwish, and E. P. Ippen. Subpicosecond gain and index nonlinearities in InGaAsP diode lasers. *Optics Communications*, 111:589–612, 1994.

[35] J. Wang, A. Maitra, C. G. Poulton, W. Freude, and J. Leuthold. Temporal Dynamics of the Alpha Factor in Semiconductor Optical Amplifiers. *Journal Of Lightwave Technology*, 25(3):891–900, 2007.

[36] F. Gigarding, G. Guekos, and A. Houbavlis. Gain recovery of bulk semiconductor optical amplifiers. *IEEE Photonics Technology Letters*, 10(6):784–786, 1998.

[37] L. Occhi. *Semiconductor Optical Amplifiers Made of Ridge Waveguide Bulk inGaAsP/InP: Experimental Characterisation and Numerical Modelling of Gain, Phase, and Noise.* PhD thesis, 2002.

Chapter 4

Timing Jitter Compensation using TOFTs

This chapter describes the generation of parabolic pulses by nonlinear propagation in a normally dispersive fibre and its application to temporal optical Fourier transforms (TOFT). In the first part, we detail how parabolic pulses can be generated in a dispersion compensating fibre (DCF). The governing equations are applied to the generation of pump pulses with parameters desirable for our application. The latter part of the chapter describes an experiment which uses the parabolic pulses to perform timing jitter compensation in a TOFT configuration.

4.1 Nonlinearly Generated Parabolic Pulses

In our efforts to generate parabolic pulses to use as time lenses, we start by investigating the simplest and most common way of encountering these pulses. Parabolic pulses have been observed naturally at the output of high power fibre amplifiers [1]. The formation of these parabolics come about from the interplay between SPM and the normal dispersion of the amplifier fibre. In 2000, Kruglov *et al.* showed theoretically that any pulse propagating in a normally dispersive fibre with constant gain would eventually evolve into a parabolic shape, so long as the bandwidth of the parabolic pulse did not exceed the gain bandwidth of the fibre [2]. In addition, after evolving into a parabolic shape, the pulse would continue to propagate in a self-similar fashion, meaning that the pulse will remain the same shape even if it increases or decreases in size [3]. This evolution is due to the parabolic shape being an asymptotic solution of the nonlinear Schrödinger equation with gain. However, the gain requirement in this form of parabolic generation is undesirable in some applications since the generated parabolic is limited by the gain bandwidth and the need for high power adds cost and complexity to the system. Alternatively, parabolic pulses have also been demonstrated to form in dispersion decreasing fibres [4]. Analytically, the decrease of dispersion in the medium is equivalent to providing gain and so also results in the forming of parabolic pulse solutions. While dispersion decreasing fibres have the benefit of being passive as opposed to the gain fibres, they can present difficulties in fabrication and are not readily available. In 2007, Finot *et al.* proposed an alternative method of generating self-formed parabolics which was both passive and without the need for fabrication of complex fibres [5]. Their method was based on using two sections of fibre instead of one, such that the parabolic pulses are formed in the first section and then maintained in the second.

The two stage method is the method we will use to generate the parabolic pulses for time lensing in this chapter. A summary of how parabolic pulses generated with this method and the parameters governing the outcome are given below. We are particularly interested in how the study presented in Ref [5] can be applied to creating a time lens for TOFT. As well as the attraction of being able to generate parabolic pulses simply in a length of DCF, the two stage configuration of this method allows for the second stage to be integrated into the time lens potentially creating a simple and elegant Fourier transformer.

4.1.1 Principle of Passive Two-Stage Parabolic Generation

The principle of generation of parabolic pulses with the passive two stage method relies on SPM and dispersion, similarly to propagation in the gain fibre. The difference is that in the absence of a constant gain, the propagation no longer evolves asymptotically towards a parabolic solution, but rather evolves *through* an optimally parabolic shape before becoming square-ish and is eventually susceptible to wave-breaking [6, 7]. Wave-breaking occurs when the new frequencies generated during SPM run out of phase with the original pulse causing interference and side lobes in the pulse. To avoid this, a suitable length of normally dispersive fibre can be chosen such that the pulse exits the fibre when it is most parabolic. This is the first stage of this two-stage method. The quality of the parabolic pulse at this optimal point (at the output of the first stage) is governed by many parameters such as the input pulse shape, the input pulse energy and the ratio between the nonlinearity and dispersion of the fibre. To find the best parabolic obtainable in the parameter space, the quality of the parabolic was quantified in Ref [5] through the use of a misfit parameter. The misfit parameter is defined by the difference between the normalized pulse intensity profile and the profile of an ideal parabolic pulse of the same energy, and is given by

$$M^2 = \frac{\int [|A|^2 - |p|^2]^2 d\tau}{\int |A|^4 d\tau}. \tag{4.1}$$

where $|A|^2$ is the pulse intensity profile and $|p|^2$ is the intensity profile of the fitted ideal parabolic. The optimal parabolic for a given input pulse shape could then be found by mapping the misfit parameter over a range of nonlinearity and dispersion. Such a map was simulated by C. Finot *et al.* for a Gaussian input pulse and shown in Fig. 4.1. The N and ξ axes in the figure are the normalized representations of the nonlinearity and dispersion respectively and are given by

$$N = T_0\sqrt{\frac{\gamma P_c}{\beta_2}} \qquad \text{and} \qquad \xi = \frac{\beta_2 L}{T_0^2} \tag{4.2}$$

where T_0 and P_c are the rms width and the peak power of the input pulse respectively, and γ and β_2 are the nonlinearity and dispersion of the first fibre respectively. The white line shown in Fig. 4.1(a) indicates the condition beyond which wave-breaking will occur and the black line in Fig. 4.1 indicates the minimum misfit as a function of ξ.

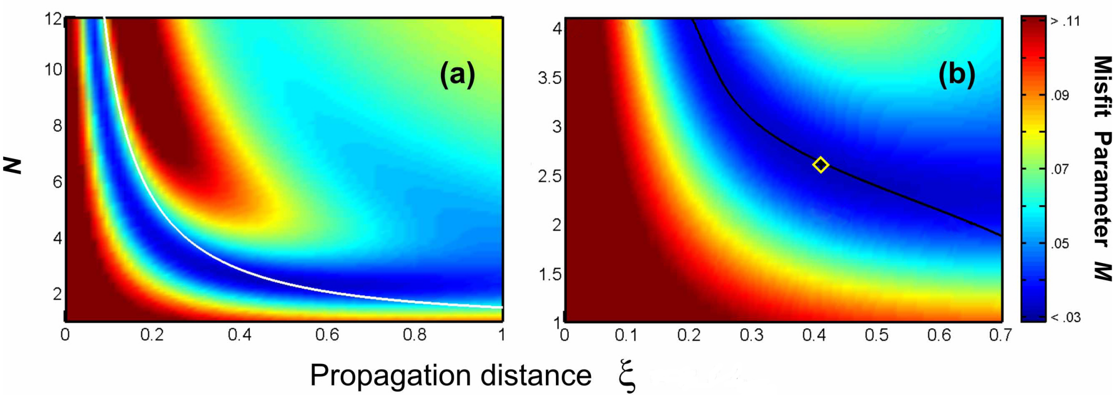

FIGURE 4.1: Evolution of the misfit parameter by N and ξ. The minimum misfit point is indicated by the yellow diamond. (adapted from figure in [5])

We had said earlier that this method uses two stages. Although the first stage was chosen to optimise the formation of a good parabolic pulse shape, the shape could not be maintained. Thus a second stage was needed to stabilise the pulses. The parabolic pulses entering the second stage should have as low a misfit as possible (ideally < 0.05)

and exhibit a linear chirp. The linear chirp is characteristic of parabolics formed through nonlinear propagation and is important because it enables the self-similar propagation observed in the gain-formed parabolics. However, this system has no gain and the requirement is instead met by an increase in nonlinearity. That is, the fibre in the second stage needs to have a nonlinearity parameter $N' > N$ where [5]

$$N' = T_0 \sqrt{\frac{\gamma' G P_c}{\beta_2'}}. \tag{4.3}$$

It can be seen from Eqn. 4.3 that choosing a fibre with a larger nonlinearity to dispersion ratio in the second stage is equivalent to providing the required gain for self-similar propagation. To avoid having to provide a gain G, we can instead obtain the nonlinear increase by choosing a second stage fibre with nonlinearity and dispersion parameters γ' and β_2' for which

$$\frac{\gamma'}{\beta_2'} > \frac{\gamma}{\beta_2}. \tag{4.4}$$

Note also that the larger the increase in γ'/β', the greater will be the effective G which is desirable in maintaining a low misfit parameter, but will also result in a wider output parabolic [5]. Thus we can use Fig. 4.1 and Eqn. 4.4 to help us to choose the parameters we will use for generating the parabolic pulses we require to perform time lensing and TOFT.

4.2 Experiment Design

4.2.1 TOFT Experiment Design

Now that we know how to generate parabolic pulses, we consider how they would be incorporated into a TOFT experiment. Fig. 4.2 shows the basic setup for a TOFT experiment.

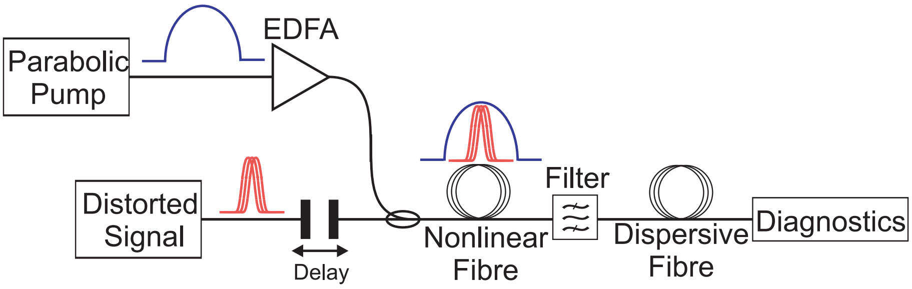

FIGURE 4.2: Basic setup for a TOFT experiment using XPM with parabolic pulses.

The high powered parabolic pump pulses are coupled with the target signal, and propagated in a length of highly nonlinear fibre (HNLF) in which XPM will occur. Recall from Chapter 2 that the XPM will impose the intensity profile of the strong pump as a phase shift onto the signal, creating the time lens. After XPM, the signal is then passed through a band-pass filter separating it from the pump to prevent further nonlinear interactions as it is dispersed through the single mode fibre (SMF). The transformed signal can then be measured. Electronic synchronization of the sources and an optical delay line aid in ensuring that the pump and signal pulses are temporally aligned in the HNLF. Since efficient XPM requires the pulses to also be aligned in polarization, polarization controllers are placed in both the pump and signal arms.

This basic overview of the setup is quite simplistic and in the next few sections we will look at each of the principle components of the setup in more detail. At the same time, we need to consider the compatibility of the components to make sure all the components work well together to successfully produce a TOFT device. Central to the compatibility of the components is the XPM process which acts as the time lens. For the XPM to create the desired quadratic phase shift on the signal, the most critical consideration is the synchronization of the pump and signal pulses such that they remain temporally stationary with respect to each other. In the first instance, this means that the pump and signal need to have the same repetition rate and have synchronized clocks. In real operation, clock recovery of the signal would first need to be performed which could be used to drive the pump source. However in our proof-of-principle experiment, the fibre lengths traversed by the signal will not be very long and synchronization of the pump and signal at the sources is sufficient. Although this ensures the pulses are synchronized at the entrance to the HNLF, greater consideration must be given to maintaining the pulse overlap during nonlinear propagation. To avoid dispersive walk-off between the two pulses as they propagate, the two pulses need to have the same group velocity. This means that either the chosen fibre needs to have a low dispersion slope, or else the wavelengths of the two pulses need to be chosen symmetrically about the zero dispersion wavelength.

Another consideration that affects the quality of the XPM phase transfer is the wavelength separation of the signal and pump. When matching the pulse wavelengths with the fibre we need to also ensure that the signal and pump are sufficiently separated in wavelength such that any spectral broadening arising from SPM of the pump will not cause it to interfere with the signal. Finally after time lensing, we require a matching dispersion. This acts as the focal length required to complete the transformation and can be easily achieved by using the correct length of a suitable fibre such as SMF. Filtering the signal before propagation in this dispersive medium ensures no further interaction between it and the pump pulses.

4.2.2 Parabolic Pulse Design

We have seen in section 4.1 that under the right conditions, a Gaussian pulse can evolve into a parabolic pulse through the use of nonlinearities. We can use this theory to generate parabolic pulses that are suitable for creating time lenses. To be able to use the parabolic pulses for time lensing, we need to consider not only the quality of the parabolic (its misfit parameter), but also its width, power, chirp and how it will evolve in the HNLF. The first two parameters, width and power, will largely determine the properties of our time lens. They also determine K which governs the magnification factor of the output (see Section 2.4). In our experiments we ideally want a parabolic pulse profile that goes to zero at ±12.5 ps (i.e. 25 ps base width), so that it could potentially be multiplexed up to 40 Gb/s. We need to start with a good quality Gaussian pulse which is shorter than the target parabolic profile, because it will broaden on propagation and develop the characteristic linear chirp. However, a Gaussian pulse which is very much shorter than the target parabolic will require a lot of growth and will thus result in a parabolic pulse which is very spectrally wide, which is also undesirable.

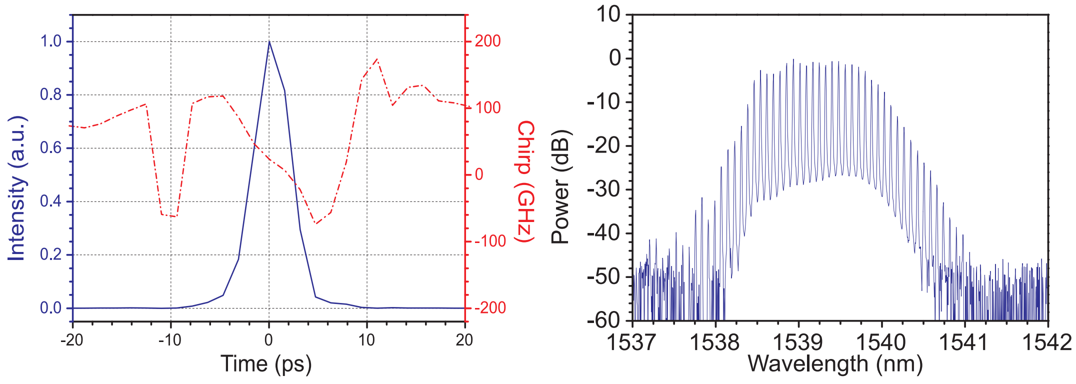

(a) (b)

FIGURE 4.3: (a) Retrieved FROG trace and (b) spectrum of the GSL output pulse (before filtering)

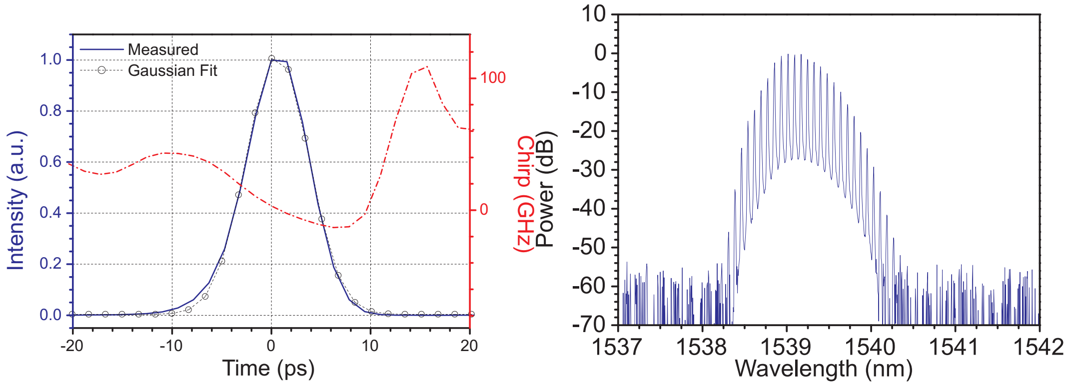

(a) (b)

FIGURE 4.4: (a) Retrieved FROG trace and (b) spectrum of filtered GSL pulse.

Our choice of pulse source falls on a DFB solid state gain-switched laser (GSL) which can be driven with a 9.953 GHz RF signal to produce 7.5 ps pulses at 1540 nm. The GSL was measured with the L-FROG using the MZM as the EOM. The L-FROG trace and spectrum of the GSL output are shown in Fig. 4.3. The spectrum shown in Fig. 4.3(b) is noticeably non-Gaussian indicating that the GSL output pulse is also not Gaussian. We can improve the shape of the pulse by shaping it with a 1 nm Gaussian thin-film tuneable filter. The characterization of the filtered output by the L-FROG can be seen in Fig. 4.4 and exhibits a good match to the fitted 7.7 ps ideal Gaussian shown. Referring back to the misfit parameter map given in Fig. 4.1, we can see that the misfit is minimised at the point $(N, \xi) = (2.6, 0.4)$ indicated by the yellow diamond. We substitute these values into Eqn. 4.2 to find the optimal parameters with which to generate the parabolic pulses for the TOFT. We are using DCF with a normal dispersion of $\beta_2 = 146$ ps^2/km and a nonlinearity of $\gamma = 8.7$ W^{-1}km^{-1} in which to generate our parabolic pulses. Eqn 4.2 can thus be rearranged to give $P = 5.5$ W and $L = 55.6$ m as the parameters we should use to minimise the misfit. Fig. 4.5(a) shows the expected output pulse when using these parameters. These pulses were simulated using a split-step Fourier routine, written by myself following the method described in [8]. Although the fit between the simulated pulse and an ideal parabolic is very good, we would ideally like to increase the input power we use in order to maximise the K of our time lens. Furthermore, we note that the output pulse is 11.4 ps (FWHM) which is shorter than the target parabolic profile of 17.7 ps (equivalent to 25 ps at the base). Thus although this configuration would give us the parabolic with the lowest misfit parameter, we see that it can still be optimised to make it more suitable for time lensing.

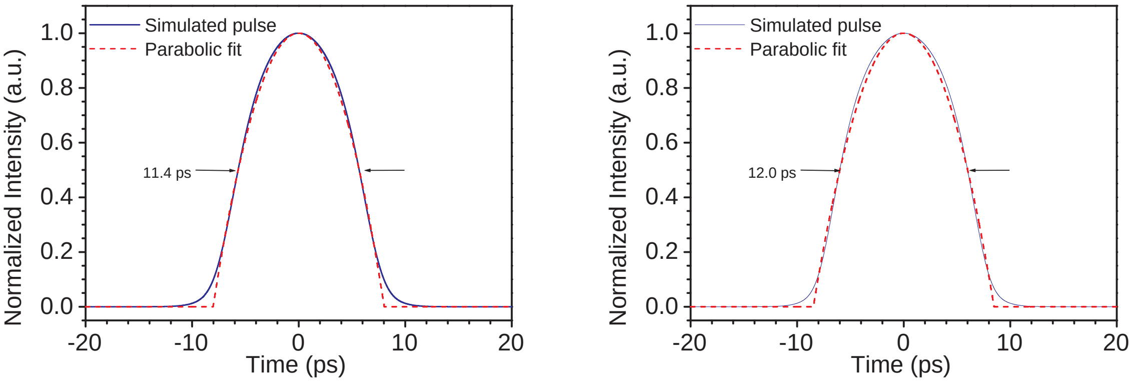

(a) (b)

Figure 4.5: (a) Lowest misfit parabolic simulated using P=5.5W and 55.6 m DCF (b) Wider parabolic simulated using P=8W and 50 m DCF

Firstly, we want to have a high pump power which means that N needs to be increased. We can refer back to the misfit parameter map (Fig. 4.1) to see how an increase in N will affect the quality of our parabolic pulse. Since we are moving away from the optimal point (2.6,0.4) we know that the misfit parameter is going to increase. However, as indicated on Fig. 4.1(b) we see that the increase in N can be partially compensated for by decreasing ξ. That is, we need to reduce the length of DCF. Fig. 4.5(b) shows the output parabolic when the average input power is increased to 28 dBm (Pp $=$ 8W,$N = 3.8$) and the length of DCF is reduced to 50 m ($\xi = 0.36$). Therefore we have managed to increase the pump power, thus increasing K which will give us higher fidelity in our TOFT as discussed in Section 2.4. Note that as an added bonus we have also managed to increase the width of the parabolic to 12 ps (FWHM) to provide a bigger window in which regeneration can occur. The sacrifice we have made here in order to achieve these is the increase in misfit parameter. It can be seen by comparison of Figs 4.5(a) and (b) that the pulse at $(N, \xi) = (2.6, 0.4)$ is a better match to an ideal parabola as compared to the revised pulse at $(N, \xi) = (3.2, 0.34)$. However, while this slightly affects the quality of the TOFT, it is more than compensated for by giving us more power and a wider regeneration window.

We have so far described the design process leading to the formation of parabolic pulses in our system. In the second stage of the parabolic generation we require a fibre in which the parabolic pulses can be stabilized and propagate self-similarly. That is, we need a fibre which will satisfy Eqn 4.4 for our system. Incidently, recall that we want to use our parabolic pulses to perform time lensing which also requires a nonlinear fibre. We can thus simplify the configuration of the device by choosing a nonlinear fibre which will satisfy the criteria for both time lensing and self-similar propagation of the parabolic pulses. Our choice of a suitable nonlinear fibre is described in the next section.

4.2.3 The Nonlinear Fibre

One of the most important parts of the setup and at least as important as the design of the pump and signal pulses, is the nonlinear medium in which they will propagate. The main purpose of the nonlinear fibre in a TOFT setup is to manifest XPM between the parabolic pump and the signal pulse so that time lensing can occur. For this purpose, it should ideally have a good nonlinearity and a suitable dispersion profile to reduce dispersive walk-off as mentioned previously. In this particular experiment, the choice of nonlinear fibre also fulfills a second role which is to act as the second stage of the parabolic pulse generator. That is, the second fibre needs to provide a medium in which the parabolic pulses can propagate self-similarly, thus maintaining their parabolic shape. This would ensure that the time lens does not distort along the fibre. To satisfy this second role, we saw from Eqn 4.4 that we need a fibre with a greater nonlinearity to dispersion ratio than the fibre in which the parabolic was formed. That is, it needs to have a higher nonlinearity or lower dispersion (or both) than the DCF.

The HNLF we chose was a 220 m, germanium-doped, narrow core fibre provided by Sumitomo Electric. It encourages XPM between the pump and the signal by having a good nonlinearity, a low dispersion and a zero-dispersion wavelength at 1550 nm. The main fibre parameters are given in Table 4.1. The low dispersion of the HNLF ensures that the signal is minimally dispersed during the time lensing process and the location of the zero-dispersion wavelength in the middle of the C-band allows us a fair amount of flexibility in choosing signal and pump wavelengths. As long as the signal and pump

Fibre Parameter	Value
γ	20 $\mathrm{W}^{-1}\mathrm{km}^{-1}$
β_2 (at 1550 nm)	-0.013 $\mathrm{ps}^2/\mathrm{km}$
β_3 (at 1550 nm)	0.048 $\mathrm{ps}^3/\mathrm{km}$
λ_0	1550 nm
L	220 m
Loss (at 1550 nm)	0.53 dB/km

TABLE 4.1: Parameters for the 220 m HNLF used for XPM.

are situated symmetrically around the zero-dispersion wavelength, the walk-off between the pump and the signal will be fairly minimal. The very low dispersion also made this fibre appropriate as the second stage of the parabolic generator, giving a nonlinearity parameter value of $N' = 80.2$. Thus N' is a large increase from $N = 3.8$ in the first stage and satisfies Eqn 4.4.

4.2.4 Test Signal

It may seem surprising that choosing a suitable target signal on which to perform a TOFT demonstration had to be undertaken as carefully as creating the parabolic time lens itself. The two most important criteria we had to consider when choosing a test signal were wavelength and pulse width. To match the pump wavelength, we needed a signal pulse at 1560 nm. The pulse width is important because we are only able to TOFT whatever lies within our time lens and so any parts of the signal extending beyond the parabolic region of the pump would not be transformed correctly. Furthermore, we required that the signal still fits in the parabolic as much as possible after a distortion has been applied. However, signals that are too short pose their own problems. We established in Section 2.4 that the greater the spectral extent of the signal, the greater K must be for a successful transformation in the spectral domain. If we choose a signal with too large a spectral content then we may find that we do not have enough pump power to ensure Eqn. 2.23 is satisfied.

This brings us to the question of signal distortion. To show that a domain swap has occurred we need a linear distortion that distinguishes the time domain signal profile from its spectrum, which should remain unchanged. Furthermore, we wanted to show that this domain swap could be applied to the compensation of distorted telecommunications signals. Signal distortion suffered in telecommunications experiments is often achieved by propagating the test signal through a real or simulated transmission system such as a recirculating loop. However for the purposes of our TOFT demonstration, the experiment was simplified by artificially introducing the distortion onto the signal before compensation with the TOFT. This had the added benefit of being controllable in severity and allows testing against a specific type of distortion, which would not be the case if real transmission was used. The distortion we applied had to be significant enough to easily observe without being so severe as to cause the signal to extend beyond the parabolic window. We decided to distort the signal pulses by introducing artificial timing jitter to the test signal. The occurrence of timing jitter in a signal does not change or shift its spectrum. Thus when a TOFT is applied the spectrum is transferred into the time domain, consistently centered and without jitter. Conversely, temporally mistimed pulses when transferred into the frequency domains, will be wavelength shifted thus converting the timing jitter into spectral jitter. The timing jitter was applied to the signal by using an additional low frequency generator to modulate the driving frequency into the signal GSL. Thus the 9.953 GHz nominal driving frequency of the signal became 9.953+$q(t)$ GHz, where $q(t) = M\sin(f't)$ is the sinusiodal RF signal from the additional generator of frequency, f'. Because $q(t)$ is only applied to the synthesizer driving the signal source, this causes a small variation in the timing of the test signals when compared to the undithered pump clock. The greater the amplitude, M, of the modulating signal, the larger will be the deviation and the timing jitter suffered by the signal. This setup gave us a distortion of artificial timing jitter that could be controlled through the amplitude of the modulating frequency and which could be easily monitored in real time by observing the signal on a high speed sampling oscilloscope. Being able to monitor the timing jitter in real time on an oscilloscope also simplified the alignment of the pump and signal pulses. The correct alignment could be easily determined from the reduction of timing jitter observed.

4.3 Timing Jitter Compensation Experiment and Results

All the elements of the TOFT experiment described above were put together in a complete setup as shown in Fig. 4.6. The final setup consisted of two synchronised GSLs at 1540 nm and 1560 nm to act as the pump and signal sources respectively.

The parabolic pulses were generated using the design parameters discussed in Section 4.2.2. The GSL output was filtered to generate a 7.7 ps Gaussian pulse (see Figs 4.3 and 4.4 for before and after filtering characterisations). The Gaussian pulse was then amplified up to an average power of 28 dBm and propagated through 50 m of DCF to evolve into a parabolic shape, which is the first stage of its development. Fig. 4.7 shows the characterisation of the pulses we obtained at the output of the DCF, which were measured using the L-FROG system and a standard OSA. Also shown in Fig. 4.7(a) is the Gaussian profile at the input to the DCF. We note that there is an asymmetry in the temporal parabolic profile, which is suspected to arise from a slight asymmetry in

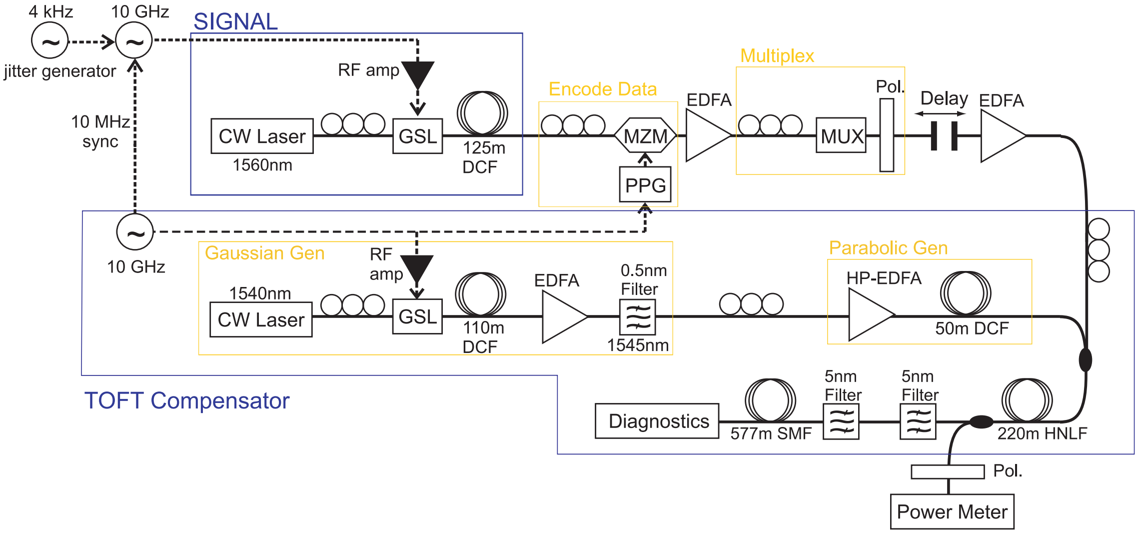

FIGURE 4.6: Setup of the TOFT experiment to compensate for timing jitter.

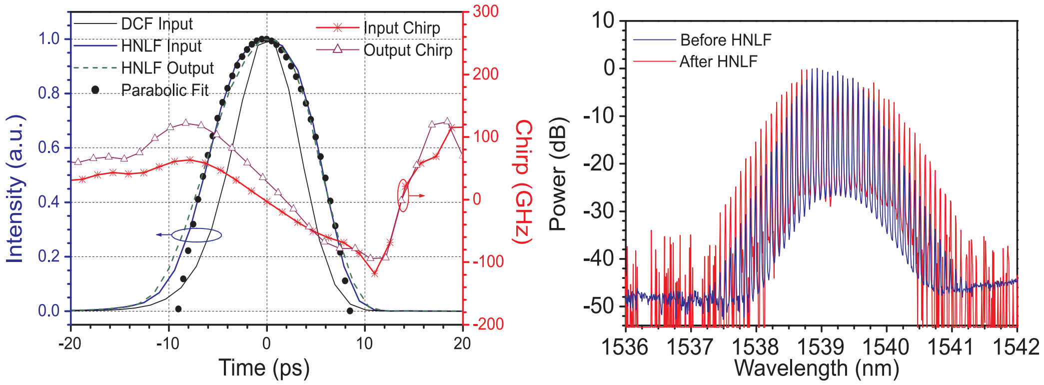

(a) (b)

FIGURE 4.7: (a) The retrieved L-FROG trace of the nonlinearly generated parabolic and (b) the spectrum of parabolic pulse, before and after the HNLF

the input pulse. The pulse nevertheless exhibits a good linear chirp across the majority of its width and matches well to an ideal parabolic in its central region.

The test signal was generated with a second 9.953 GHz GSL at 1560 nm. The output of the GSL was compressed with 125 m of DCF to compensate for the inherent chirp from the source. Fig. 4.8 shows the L-FROG trace and spectrum of the 10 Gb/s signal. The measured signal is 4.9 ps wide (FWHM), with a flat phase in Fig. 4.8(a) showing that the chirp has been fully compensated. The signal can also be seen to have small side lobes which arise from the square-ish, non-Gaussian shape of the spectrum seen in Fig. 4.8(b). We resisted filtering the signal to obtain a better shape, in order to maintain the minimum pulse width. The pulses were passed through a polarisation

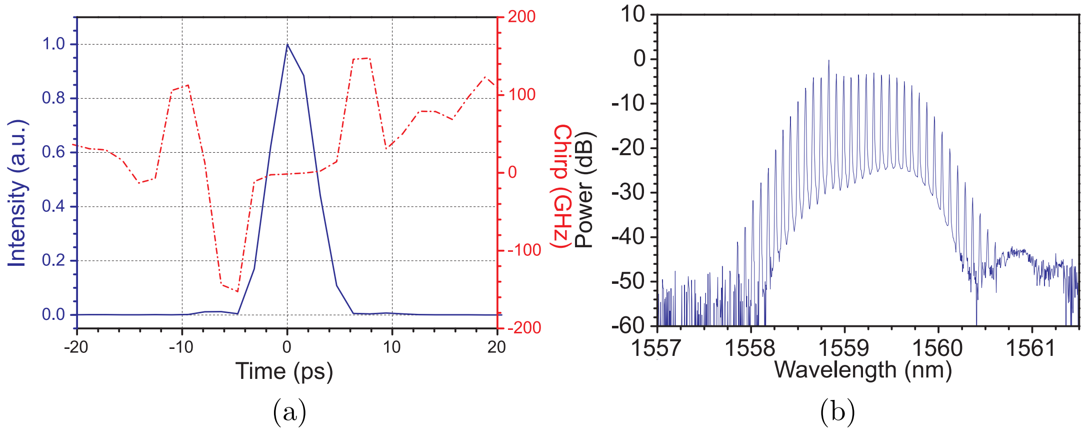

FIGURE 4.8: (a) Retrieved FROG trace and (b) spectrum of the 10 Gb/s signal

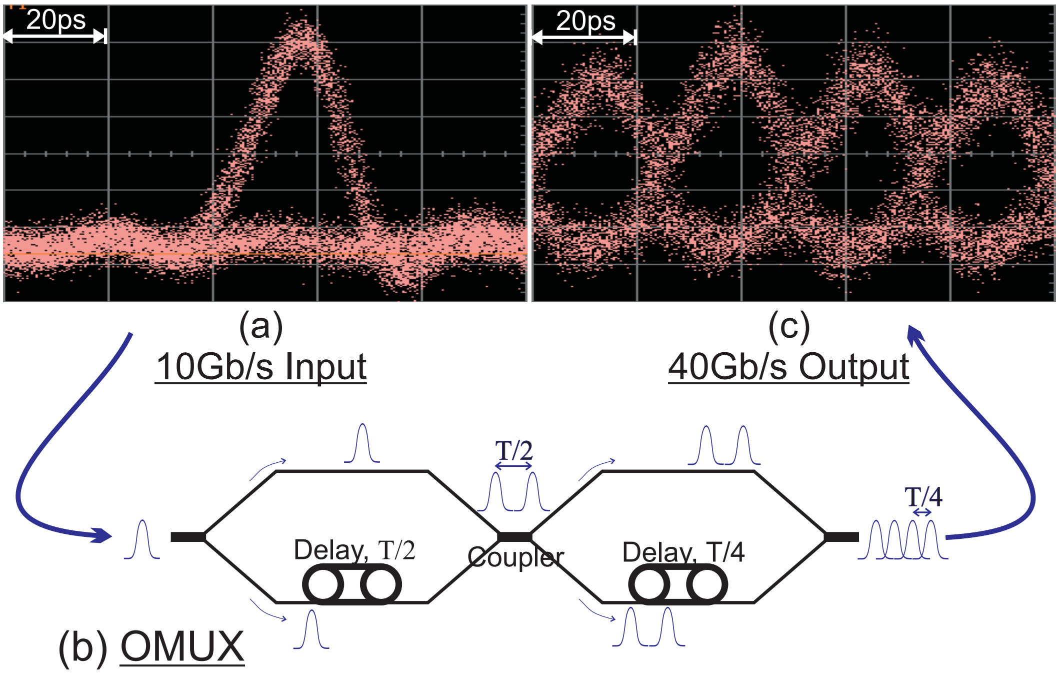

FIGURE 4.9: Waveform of the data (a) at 10 GB/s, (b) through the OMUX and (c) after multiplexing to 40 Gb/s.

controller and a LiNbO$_3$ Mach-Zehnder modulator to be encoded with a $2^{31}-1$ pseudo-random bit sequence (PRBS). The eye diagram of the 10 Gb/s test signal after data modulation is shown in Fig. 4.9(a), as measured with a sampling oscilloscope. The broad width of the signal shown here and the ringing surrounding it are due to the limited 32 GHz bandwidth of the photodetector. The 10 Gb/s encoded signal was then multiplexed up to 40Gb/s while the pump remained at 10 Gb/s to demonstrate the effect of regenerating one 10 Gb/s tributary against the other three. The optical multiplexer (OMUX) we used was made in house and consisted of a series of couplers and delay lines as shown schematically in Fig. 4.9(b). The delay lines were made by wrapping lengths of polarisation maintaining fibre around micrometer controlled fibre stretchers. The resulting multiplexed 40 Gb/s signal is shown in Fig. 4.9(c). It can be seen that there is a slight variation in the amplitudes of the four channels. This is due to an imperfection in the construction of the multiplexer in balancing the polarisations of the various channels and could not be adjusted at the time of this experiment. This 40 Gb/s data was then the initial signal for this experiment.

The next step was to apply timing jitter to the signal. To quantify the amount of timing jitter we were adding to the signal we measured the 'width' of the leading edge of its eye diagram. That is, a histogram was taken of a slice of the leading edge of the signal as shown in Fig. 4.10. The histogram represents the distribution of arrival times of the signal pulses into the photodiode and so will broaden for strongly jittered pulses and narrow for well timed pulses. The severity of the jitter can thus be quantified by measuring the standard deviation of the histogram distribution at a given intensity level of the pulse (e.g. half maximum). Fig. 4.11(a) shows our multiplexed 40 Gb/s signal after the application of timing jitter. The timing jitter of the clean signal was measured to have a standard deviation of less than 800 fs, but could not be accurately resolved, since this is the inherent jitter of the sampling oscilloscope. After introduction of the artificial timing jitter (shown in Fig. 4.11(a)), the signal jitter was measured to have a standard deviation of 1.6 ps, which is more than twice the timing jitter of the clean signal.

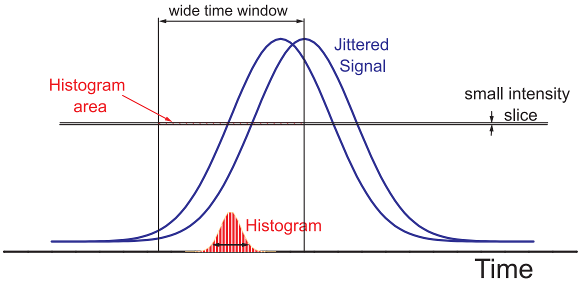

FIGURE 4.10: Timing jitter was quantified by taking a histogram of the samples in the selected histogram area. A narrow intensity slice and a wide temporal selection is used take a width measurement of the leading edge.

The high powered parabolic pump pulses and timing jittered signal were combined via a 90:10 coupler to preserve as much of the pump power as possible (21.4 dBm). The pulses were then launched into the 220 m HNLF to undergo XPM. After the time lensing by XPM, the signal was separated from the pump using two 5 nm band pass filters to increase the combined filter extinction ratio and ensure that the pump was fully excluded. Finally, a 577 m length of anomalously dispersive SMF was used to match the chirp induced by the pump and complete the transformation.

Fig. 4.11 shows characterisations of the timing jittered test signal before and after TOFT. Parts (a), (c) and (e) on the left column shows measurements of the noisy signal before TOFT and parts (b), (d) and (f) in the right column shows the measurements of the signal after TOFT. The eye diagram of the noisy signal in Fig. 4.11(a) distinctly shows a broader leading and trailing edge distributions than the clean signal shown in Fig. 4.9(b). After TOFT, in Fig. 4.11(b) it can be clearly seen that the second channel (indicated with an arrow) has a much reduced jitter. Unfortunately due to the severe jitter from the neighbouring channels and the limited bandwidth of the detector, it was not possible to quantify the reduction in jitter of the output pulse. However, the eye can be seen to be wider in the regenerated channel compared to the uncompensated channels and the pulse edges are better defined. Figs 4.11(c) and (d) show L-FROG characterisations of the 40 Gb/s signal before and after TOFT. Although the L-FROG is an averaged measurement and thus does not show timing jitter, we can see that where all the four pulses had the same profile and phase in Fig. 4.11(c). Then after the TOFT, the second pulse (indicated with an arrow) has been regenerated and is cleaner than the others in Fig. 4.11(d). Note in particular that the regenerated pulse is a clean shape and no longer exhibits the side lobes of the input and further, that it has a flat chirp indicating proper compensation. The final two parts (e) and (f) show the corresponding spectrum of the signal before and after TOFT. Although the signal spectrum appears noisy, this is due to the affect of applying the PRBS modulation.

The characterisations of the output pulses in Fig. 4.11 show that we have effectively compensated for the timing jitter. However, it was mentioned above that we have been unable to quantify the jitter reduction due to the lack of distinction between the regenerated channel and its neighbouring channels. While this could be improved by using a photodetector with a larger bandwidth, it is also in part due to the quality of the input signal. We observed in Fig. 4.8(a) that the signal pulse exhibited side lobes and commented that we were reluctant to filter the signal in order to preserve its narrow width. The preservation of the signal width was important in ensuring confinement of the signal within the parabolic window. However, the side lobes then became the cause

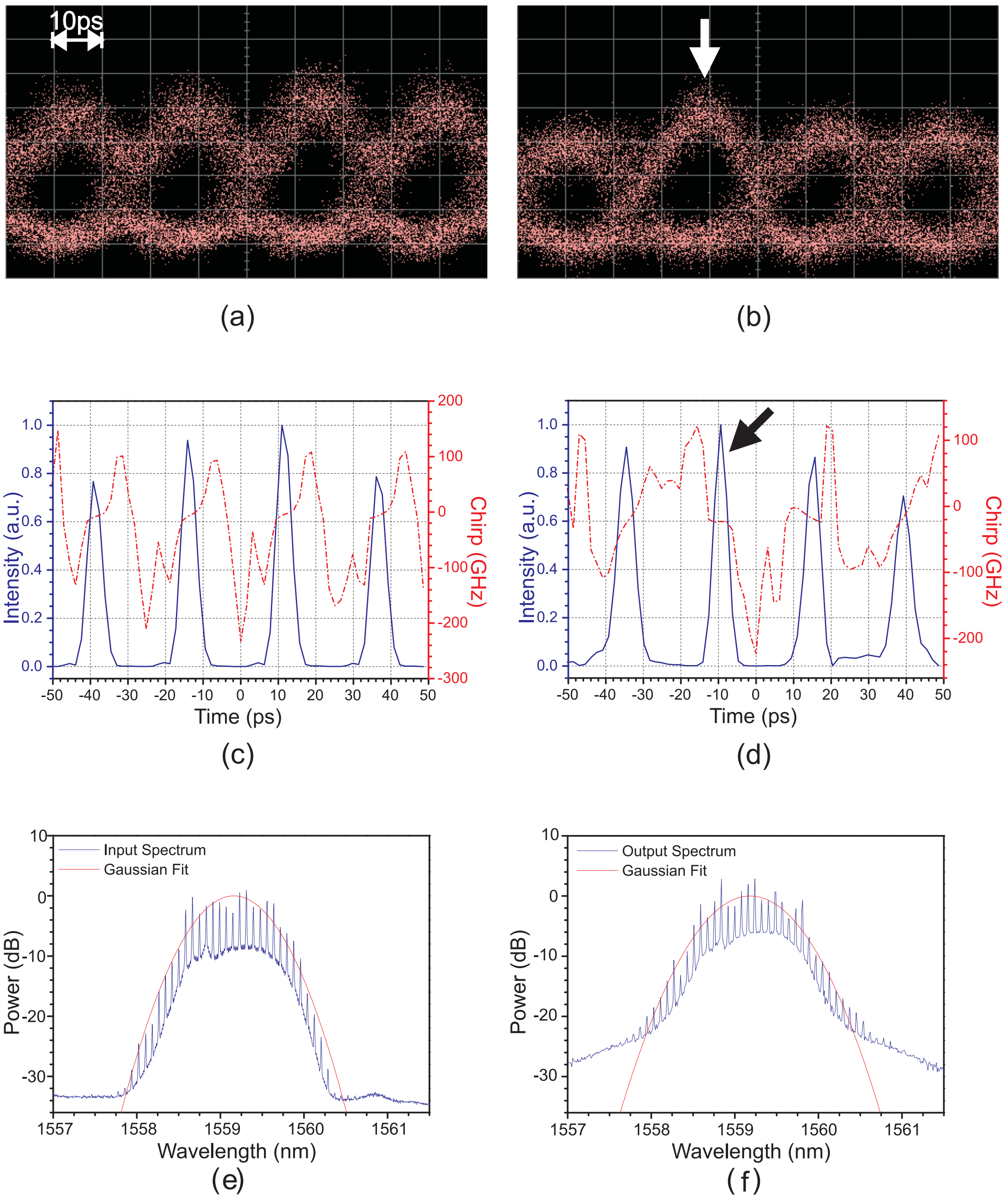

FIGURE 4.11: Jittered 40Gb/s signal: Eye (a) before TOFT and (b) after TOFT with one channel regenerated (arrow). L-FROG (c) before TOFT and (d) after TOFT with one channel regenerated (arrow). Spectrum (e) before TOFT and (f) after TOFT.

of interference and beating between the multiplexed pulses when jitter was introduced. This problem could have been resolved with the use of a wider bandwidth signal source such as a mode-locked laser. Unfortunately at the time of these experiments, no functioning solution was available in our lab and it was decided that time should be better spent in exploring new experimental directions.

While awaiting more suitable signal sources, we investigated some ways in which the TOFT device could be improved. The most significant of these is the inflexibility presented by the interdependence between the parabolic pulses' width, quality and power. We noted in Section 4.2.2 that in order to increase K and obtain a wider transform window, we had to sacrifice some of the quality of the parabolic pulse. To be able to overcome the interdependence would extend the applicability of this technique to allow for independent scaling of K and the transform window width. We have in the following chapters investigated the generation of parabolic pulses by more flexible means. More specifically, different forms of spectral filtering are used to generate parabolic pulses which can be propagated through SMF or other optical components such as an amplifier without sacrificing the quality of the parabolic profile.

4.4 Conclusions

In this chapter we have performed the implementation of a temporal optical Fourier transform by using parabolic pulses for time lensing. The parabolic pulses were generated in a two stage system by exploiting their natural evolution in normally dispersive nonlinear fibre in the first stage to form the parabolic shape, and then maintained in a second highly nonlinear stage. We have shown that given an appropriate combination of parameters and nonlinear fibres, these passively generated parabolic pulses can be maintained for use in further applications. The nonlinear parabolics were used to create a time lens, by undergoing XPM with the test signal to create a TOFT based timing jitter compensator. The TOFT based timing jitter compensator was operated at 10 GHz against a 40 Gb/s data stream in order to regenerate one out of the four 10 Gb/s OTDM tributaries. The sampled eye and L-FROG characterisations of the 40 Gb/s output signal clearly show the improvement of the regenerated channel compared to its neighbours. Finally, we discussed the limitations and potential improvements to this system. The incompatibility of the system to pump power changes leads us to investigate spectrally shaped parabolic pulses in the following chapters.

Bibliography

[1] M. E. Fernmann, V. I. Kruglov, B. C. Thomsen, J. M. Dudley, and J. D. Harvey. Self-similar propagation and amplification of parabolic pulses in optical fibres. *Physical Review Letters*, 84(26):6010–6013, 2000.

[2] V. I. Kruglov, A. C. Peacock, J. D. Harvey, and J. M. Dudley. Self-similar propagation of parabolic pulses in normal-dispersion fibre amplifiers. *Journal of the Optical Society Of America B - Optical Physics*, 19(3):461–469, 2002.

[3] C. Finot, F. Parmigiani, P. Petropoulos, and D. J. Richardson. Parabolic pulse evolution in normally dispersive fiber amplifiers preceding the similariton formation regime. *Optics Express*, 14(8):3161–3170, 2006.

[4] A. Plotski, A. Sysoliatin, M. Y. Salganskii, P. Harper, J. Harrison, S. K. Turitsyn, and A. I. Latkin. High power parabolic pulse generation in dispersion decreasing tapered fibre. In *Optical Fibre Communications Conference*, page OTuJ2, Anaheim, 2007.

[5] C. Finot, L. Provost, P. Petropoulos, and D. J. Richardson. Parabolic pulse generation through passive nonlinear pulse reshaping in a normally dispersive two segment fiber device. *Optics Express*, 15(3):852–864, 2007.

[6] D. Anderson, M. Desaix, M. Karlsson, M. Lisak, and M. L. Quiroga-Teixeiro. Wave-breaking-free pulses in nonlinear-optical fibers. *Journal of the Optical Society of America B*, 10(7):1185–1190, 1993.

[7] S. Boscolo, A. I. Latkin, and S. K. Turitsyn. Passive nonlinear pulse shaping in normally dispersive fibre systems. *IEEE Journal of Quantum Electronics*, 44(12):1196–1203, 2008.

[8] G. P. Agrawal. *Nonlinear Fiber Optics.* Optics and Photonics. Academic Press, third edition, 2001.

Chapter 5

TOFT using Parabolic Pulses Formed in a SSFBG

In this chapter, we demonstrate the compensation of second and third order dispersion by performing TOFT with a different type of parabolic pulse. The parabolic pulses we use here do not evolve naturally as they did in the experiments of Chapter 4, but are specifically shaped using a specially designed superstructured fibre Bragg grating (SSFBG). The use of a grating allows us to have much greater control of the shape and phase profile of the parabolic pulses, hence greatly reducing the tails we saw on the nonlinearly generated parabolics. Furthermore using a grating greatly relaxes many of the compatibility considerations that we had to make previously, between the parabolic generation and the time lensing stages of the setup. For instance when the parabolic pulses were generated nonlinearly, they were linearly chirped, meaning that it was important to minimise any SMF between the two stages and that a careful choice of the fibre for XPM had to be made. Both of these are important to maintaining the required balance between nonlinearity and dispersion during the propagation of the parabolic pulse, and hence preserve its shape. Consequently, the input power of the parabolic pulses and hence the K of the time lens could not be freely adjusted and had to coincide with powers that were optimal for parabolic generation. Parabolic pulses generated by SSFBGs can overcome this limitation by producing unchirped pulses which are minimally affected by amplification and thus allows the K of the time lens to be easily and independently adjusted.

The first part of this chapter gives a brief overview of fibre Bragg gratings and SSFBGs, how they are designed and how they can be used to create interesting and useful pulse

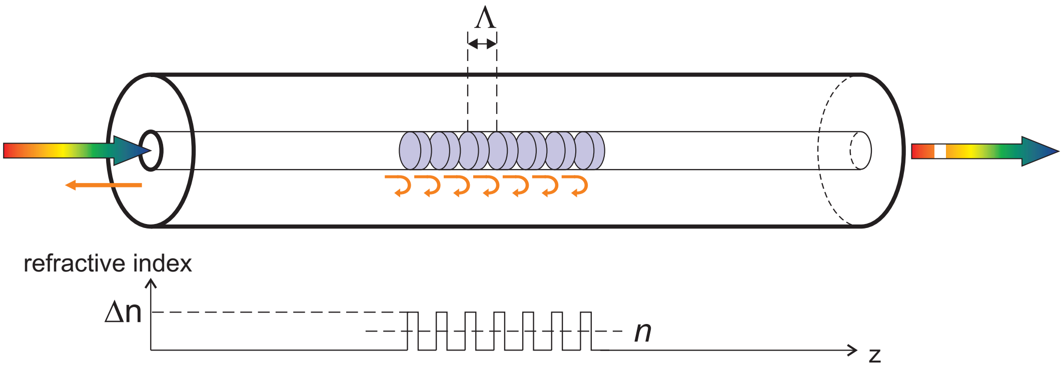

FIGURE 5.1: Filtering by a fibre Bragg grating.

shapes. The design of SSFBGs for parabolic pulse generation is then described and the output pulses characterised. Finally we demonstrate the compensation of pulses degraded with second and third order dispersion by using the SSFBG generated parabolic pulses in a TOFT compensator.

5.1 Fibre Bragg Gratings

Fibre Bragg gratings (FBG) are commonly used in telecommunications as filters [1], demultiplexers [2, 3] and dispersion compensators [4]. The most basic FBGs work by having a periodically varying refractive index in the core of the fibre which acts as a Bragg reflector to a given wavelength. The principle is shown in Fig. 5.1. At the interface of each refractive index change, a small fraction of the input light is reflected. The Bragg wavelength is the wavelength for which all the reflected portions are in phase and interfere constructively. This is given by

$$\lambda_B = 2n\Lambda \tag{5.1}$$

where n is the mean refractive index of the grating and Λ is the period of the grating as indicated in Fig. 5.1. As a result the Bragg wavelength will be strongly reflected back along the fibre while the other wavelengths pass through.

Such FBGs can be fabricated (or written) by using the UV sensitivity of hydrogenated, germanium-doped silica to produce the refractive index change. Fig. 5.2 shows an example of a grating writing rig. A UV laser beam is shone onto the fibre to be written through a phase mask. The first order diffracted beams from the phase mask will form

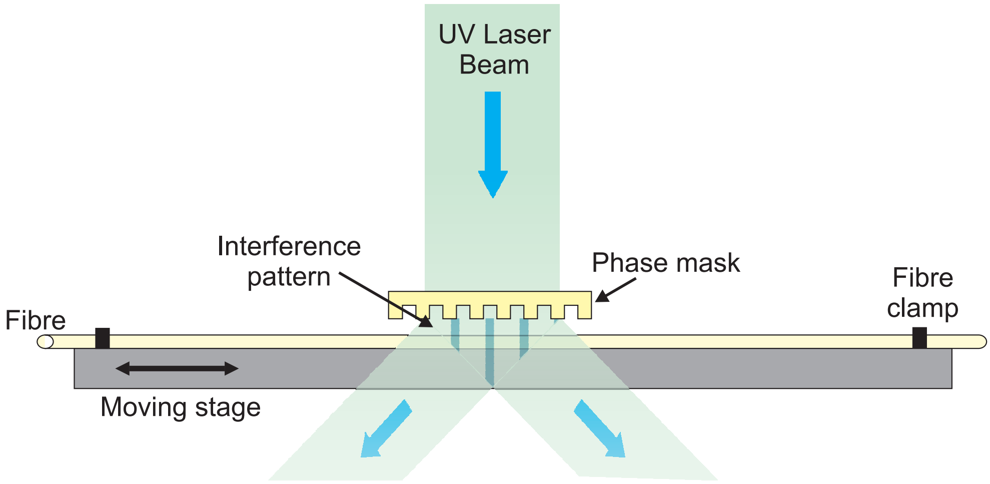

FIGURE 5.2: Schematic of a grating writing rig.

an interference pattern in the region below the mask where the exposed fibre lies. Illumination of the doped fibre core with the UV interference pattern will cause the doped silica to have an increased refractive index at the high intensity parts. Thus the interference pattern imparts a periodic refractive index change onto the fibre. For some more complicated grating structures such as the SSFBGs discussed and used in this chapter, a moving stage is used to move the fibre relative to the interference pattern. This enables longer gratings to be written and also for the grating profile to be more flexibly tailored along the length of the fibre. Smearing of the periodic structure during fibre translation is avoided by turning the UV beam on and off, such that the final structure is written in multiple sections. Further details of the technique used to write the gratings used in this chapter can be found in Ref [5].

Some common FBG structures are shown in Fig. 5.3 with their corresponding spectra. Fig. 5.3(a) shows the typical reflection spectrum for a uniform grating. The width of the drop band, $\Delta\lambda$ is given by

$$\frac{\Delta\lambda}{\lambda} \approx \frac{vn}{n_{eff}}$$

where v is the visibility of the modulation fringes and n_{eff} is the effective refractive index of the core outside the grating. More precise estimation of grating reflection spectra can be found using coupled-mode theory. While a thorough description of coupled-mode theory and its applications to various grating types is beyond the scope of this thesis, it can be found in many good references, of which I give a few [6–8]. Fig. 5.3(b) shows the structure of an apodized grating for which the refractive index change, Δn, is tapered

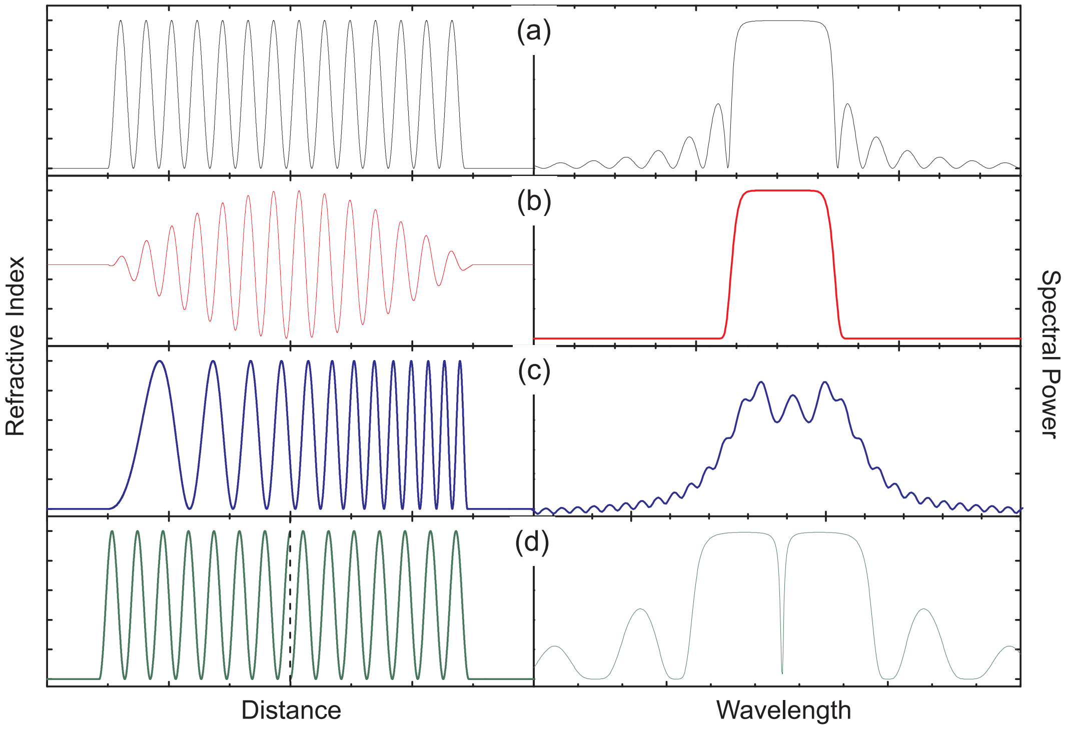

FIGURE 5.3: Some common fibre Bragg grating structures. Shown are (a) uniform, (b) raised-cosine apodized, (c) chirped and (d) phase shifted grating profiles and their corresponding spectra. Note that the grating period has been greatly exaggerated in these figures.

at the ends of the grating. This has the effect of suppressing the side lobes in the reflection spectrum and thus producing a cleaner filter. Chirped gratings (Fig. 5.3(c)) have a period that changes along the length of the grating causing different wavelengths to be reflected at different parts of the grating. The time delay between the wavelengths propagating different path lengths applies a dispersion to the filtered signal. Chirped gratings can thus be used for dispersion compensation. Fig. 5.3(d) shows a grating exhibiting a phase shift. Introducing phase shifts in a grating can be used to obtain very narrow transmission peaks and are often necessary for creating complex pulse shapes.

FBGs have a wide range of applications in telecommunications where their robust fiberized form is particularly attractive. The dependence of the Bragg wavelength on the grating period (in terms of optical path length), Λ, means that the wavelength and dispersion of a grating is tunable through stretching or compressing the fibres [9], or even by temperature tuning [4]. The versatility of FBGs is demonstrated by their wide range of uses within the experiments in this chapter. As well as their main use in shaping sech^2 pulses into parabolic pulses for time lensing, they will also be used to generate the

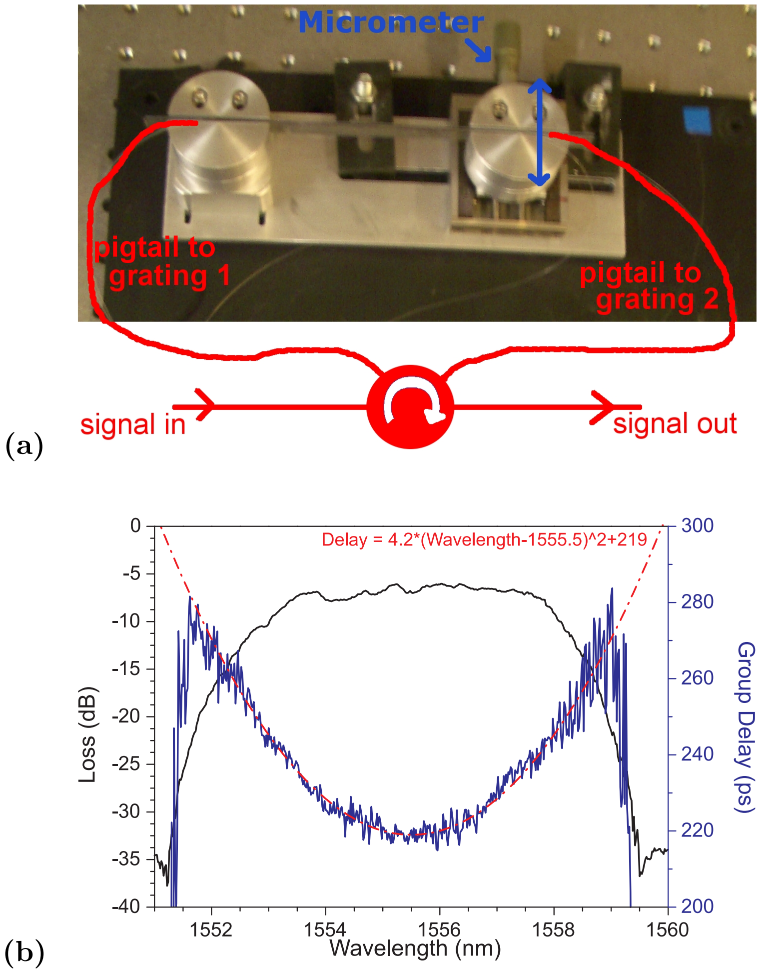

FIGURE 5.4: (a) Photo of the tunable TOD grating rig. (b) Characterisation of the third order dispersion TOD grating at the setting used for experiment.

TOD impairment we want to compensate for.

To generate the third order dispersion (TOD) we wanted to show compensation for in this experiment, two chirped fibre gratings were fabricated and mounted together in a strain rig to enable tunability. The first grating imposed both a group velocity dispersion (GVD) and a TOD to the signal, while the second grating compensated for the GVD in the first grating. A photo of the TOD gratings fabricated by M. Ibsen and mounted by Z. Zhang are shown in Fig. 5.4(a). At the top right corner of the strain rig can be seen a micrometer which is used the tune the gratings by moving one end of the mount. This in turn flexes the mount in an S-bend, thus stretching and compressing parts of it to change the induced delay. By mounting the gratings together, the GVD values were always matched and only the TOD was tuned as the mount is flexed. Fig. 5.4(b) shows the characterisation of the grating pair tuned to a TOD value of 8.4 ps/nm^2.

5.2 Superstructured Fibre Bragg Gratings

Another type of FBG which is of particular interest to us is the SSFBG. SSFBGs are able to shape pulses by having an overlaying superstructure which modulates the standard refractive index modulations of the grating [10]. When written weakly (<20% reflectivity to ensure full penetration of the wave into the grating) this superstructure can be shown to have the same profile as the grating's impulse response in both phase and amplitude [11, 12]. However, the impulse response itself will not determine the output pulse we can expect from a grating, which is of course also dependent on the input pulse. Rather, the output will be given by the convolution of the input and impulse functions. That is,

$$y(t) = x(t) * h(t) \tag{5.2}$$

where $y(t)$ is the output temporal profile, $x(t)$ is the input profile and $h(t)$ is the impulse function.

To design a grating to generate a specific output pulse from a given input, we can simplify the calculation of $h(t)$ by looking at its Fourier transform $H(\omega)$. In the frequency domain, the convolution becomes the product

$$Y(\omega) = X(\omega)H(\omega) \tag{5.3}$$

from which we can find the required reflection spectrum $H(\omega)$ from the input $X(\omega)$ and desired output $Y(\omega)$ spectra. Thus the grating requires an impulse response given by

$$h(t) = F^{-1}\{H(\omega)\} = F^{-1}\left\{\frac{Y(\omega)}{X(\omega)}\right\}. \tag{5.4}$$

From here, we can find the required superstructure of the grating by scaling the impulse response with the time-to-space transformation $z = \frac{tc}{2n}$, which arises from the propagation time of the light reflected in the grating. A diagram of the design process is shown in Fig. 5.5. The method described has been used to design gratings for several interesting pulse shapes which are useful for optical signal processing [13–15].

5.3 TOFT Setup using a Superstructured Grating

The experimental setup and operation principle of the scheme is shown in Fig. 5.6. In this experiment, we changed our pump source from the GSL we used in Chapter 4 to

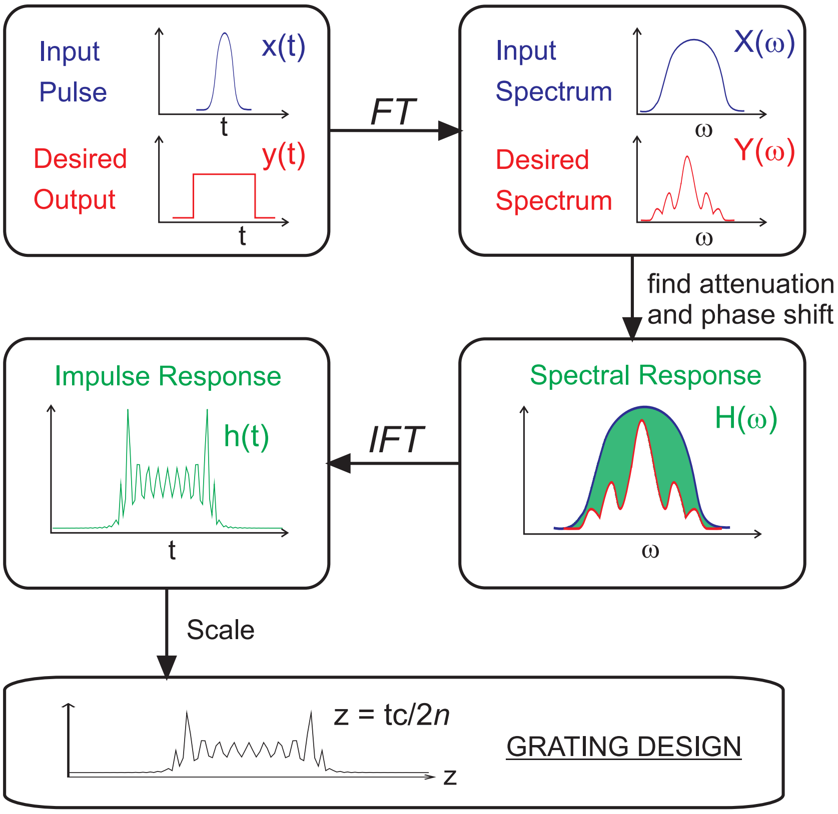

FIGURE 5.5: Flow chart of the steps in designing a SSFBG

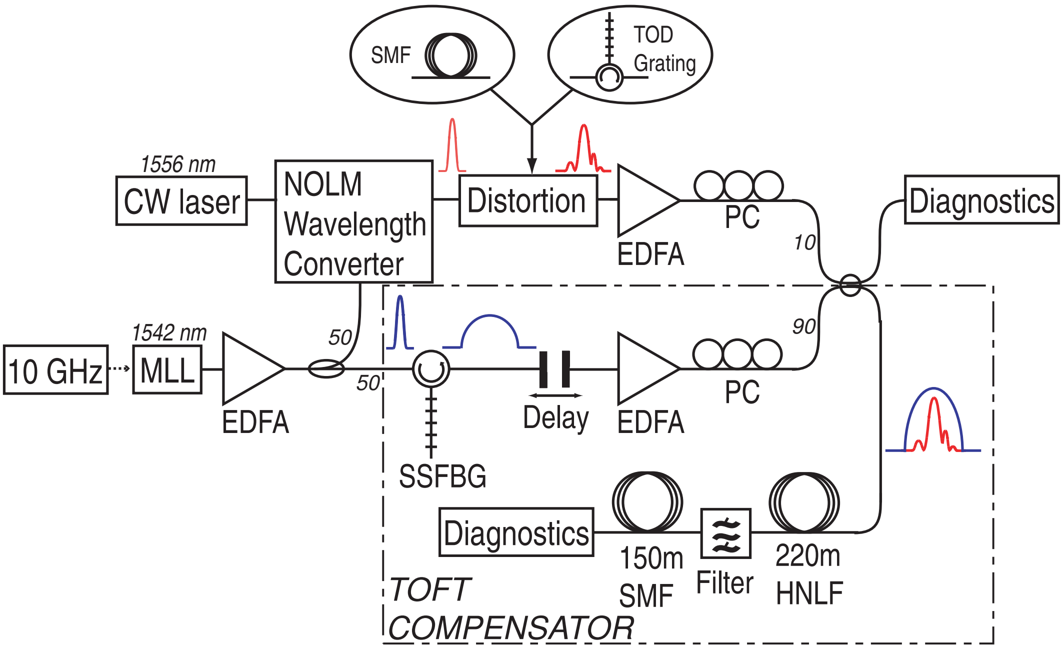

FIGURE 5.6: Experimental setup of the Fourier transform compensator using a SSFBG.

the 10 GHz mode-locked erbium fiber ring laser (MLL) used in Section 3.2. The change was required because unlike the nonlinear method of generating parabolic pulses we

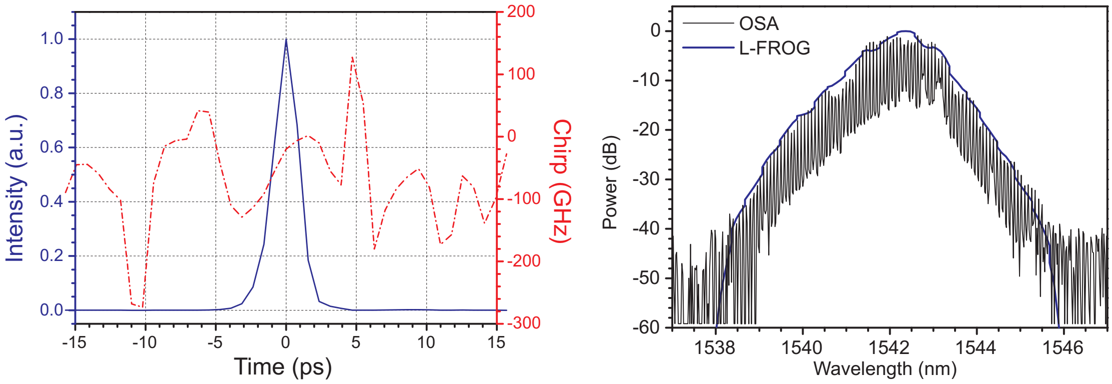

(a) **(b)**

FIGURE 5.7: (a) L-FROG characterization of the MLL output pulse. (b) Spectrum of the MLL output.

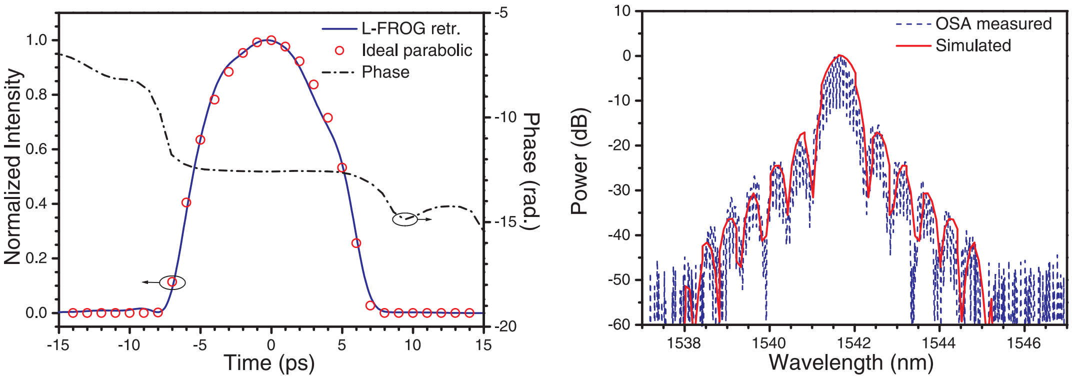

(a) **(b)**

FIGURE 5.8: (a) Temporal profile of the parabolic pulse as compared to an ideal 10 ps parabola. (b) Spectral response of the SSFBG.

described in Chapter 4, we are now filtering the pump spectrum rather than broadening it. We thus need to start with a pulse bandwidth that is greater than the design width in order to ensure there is enough bandwidth to be carved with the SSFBG. The MLL was operated at 1542 nm to produce 2.1 ps sech^2 pulses with a 3-dB bandwidth of 1.7 nm.

The laser pulses are shown in Fig. 5.7. The pulses were then amplified and shaped in a SSFBG designed to generate a 10 ps (FWHM) parabolic envelope superimposed upon a fifth order super-Gaussian profile to reduce their spectral extent. The amplifier was necessary due to the high loss inherent in these weakly reflective gratings, which was 10.4 dB in our case. The grating was designed by F. Parmigiani and fabricated by M. Ibsen for a previous application [16, 17]. The resulting pulses reflected off the grating were characterised with the L-FROG system and are shown in Fig. 5.8. Fig. 5.8(a) shows the temporal profile of the measured pulses as compared to an ideal parabolic

Fibre Parameter	Value
γ	20 $\mathrm{W}^{-1}\mathrm{km}^{-1}$
β_2	0.816 ps^2
β_3	0.046 ps^3
λ_0	1550 nm
L	490 m

Table 5.1: Parameters for the 490 m HNLF used in the NOLM.

pulse. The good agreement between the measured and the ideal pulses confirm that that the intensity profile of our shaped pulses had an almost linear gradient which in turn should induce a linear chirp on our distorted pulses by action of the XPM in the TOFT system. The reflected pulse spectrum is given in Fig. 5.8(b) showing the spectral shaping imposed by the SSFBG.

We also changed the test signal to use for this experiment. In the previous chapter, we had struggled with obtaining a test signal which would be well confined within the TOFT compensation window. We had compromised by obtaining signal pulses which were 5 ps wide, but of poor quality. In this improved experiment, we wish to solve the problem by using the MLL to generate the signal pulses. However, because this source was already being used to generate the parabolic pump pulses at 1542 nm, we needed to first split the MLL output into two paths using a 50:50 coupler and then wavelength convert one path to a suitable signal wavelength. The wavelength conversion was achieved with a nonlinear optical loop mirror (NOLM) employing a 490 m length of HNLF.

The principle of operation of the NOLM is shown in Fig. 5.9 and the main parameters of the HNLF are shown in Table 5.1. Wavelength conversion is achieved in a NOLM by using the pulsed signal as a nonlinear gate with which to carve pulses from a CW. In the absence of the pulsed signal, the CW is split 50:50 into two waves entering the NOLM, one propagating clockwise and the other anti-clockwise around the loop. Due to the operation of the directional coupler, a $\pi/2$ phase shift is acquired each time the light passes through it. Thus the counter-propagating waves will be $\pi/2$ out of phase with each other and after traversing the same length around the NOLM will interfere destructively in the output direction and contructively in the input direction. The NOLM is thus acting as a mirror in sending all the signal power back towards the input. We can upset the balance between the two counter propagating waves by introducing the pulsed signal which co-propagates with only the clockwise wave. As XPM occurs in the HNLF between the pulsed signal and the clockwise wave, it gains a phase shift

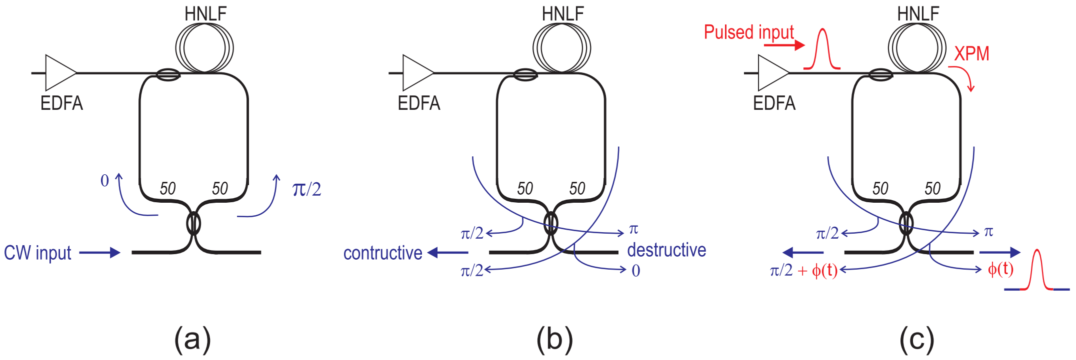

FIGURE 5.9: Operational principle of the NOLM. (a) The counter-propagating waves are $\pi/2$ out of phase. (b) After traversing the same path they interfere destructively at the output and constructively at the input. (c) XPM with a control pulse induces a phase shift in one wave which opens a gate to produce a pulse similar to the control.

which is dependent on the power of the pulses. Tuning the pulse peak power to induce a π phase shift in the clockwise signal will cause it to now interfere constructively at the output and so carve a pulse of a similar width to the pulsed input signal, but at the wavelength of the CW.

We were able to obtain 3 ps pulses at 1556 nm at the output of our NOLM which we used as our test signal for the TOFT (see Fig. 5.10). Both the temporal and spectral profiles can be seen to be clean with an almost flat phase in the temporal pulse. The spike in the centre of the spectrum is a residual CW component which was incompletely compressed by the pulse carving in the NOLM. These pulses were subsequently passed through a distortion stage consisting of either a length of SMF for second order dispersion (GVD), or the chirped FBG to impose TOD on the signal. These formed the target signal to be processed and were coupled together with the amplified parabolic pulses using a 90:10 coupler. An optical delay line in the path of the parabolic pump was used to ensure the signal and pump pulses were overlapping temporally before being launched into the 220 m length of HNLF. This was the same fibre we used in Chapter 4 and its parameters are given in Table 4.1. As we were no longer using a nonlinearly generated parabolic pulse, we were able to place an EDFA in the pump arm. This allowed flexible amplification of the pump pulse which in turn allows tuning of K. The signal pulses however, were kept at a low power level (3 dBm) to avoid any spectral broadening from SPM.

As the distorted signal propagated through the HNLF, it acquired a linear chirp from XPM induced by the much stronger parabolic pulses. After the HNLF, the parabolic

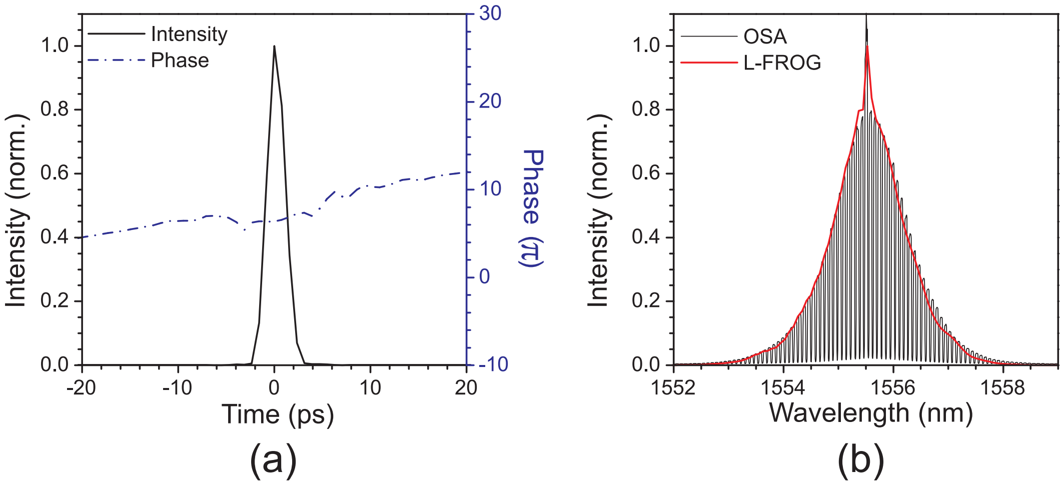

Figure 5.10: (a) Temporal profile of the clean input signal measured at output of the NOLM using the L-FROG and (b) its corresponding spectrum compared to the OSA.

pulses are filtered out by a 3 nm bandpass filter centered at 1556 nm, and the target signal launched into 150 m of SMF to complete the transformation [18].

5.4 Compensation of Group Velocity Dispersion using TOFT

We tested the operation of our TOFT compensator using target pulses which were clean, and those that were distorted with GVD. According to Eqn. 2.20, our parabolic pump pulses required an average power of 19.5 dBm to generate a chirp rate, $K = -0.34$ ps^{-2}, to inversely match the dispersion, $\beta_2 L = -3$ ps^2, arising from 150 m of SMF. However, recognizing TOFT of a GVD broadened signal is difficult because GVD changes only the width of the pulse and not the shape. Thus, in order to verify that TOFT would be achieved, we measured the pulse width that we obtained at the output of the system for various values of pump power. This was done for several values of applied GVD.

We expected that although pulses with different applied GVD would have different input pulse widths, the preservation of the spectrum in GVD would ensure they all have the same output pulse width if a TOFT has occurred. This behaviour would not be observed if instead of a TOFT, pulse compression had occurred, since compression would cause different input distortions to result in different transformed widths. Thus we can confirm the matching condition by observing the change in pulse width of the target pulses at the output of the compensator as the pump power is increased. This is shown in Fig. 5.11 (lines) where we have simulated the plot of output pulse width against average pump power for target pulses with different levels of distortion. We see that all the output pulses converge to the same width near the calculated pump power indicating the operational point for TOFT. Our measurements of the system as shown by Fig. 5.11 (symbols) confirm this and agree reasonably well with our simulations, intersecting near the predicted power level. The slight misalignment of the simulated intersection point is due to some minor leakage of the widely dispersed pulses outside the transform window. Therefore only the portion of the pulse inside the window will be transformed resulting in a narrower output, but also the formation of side lobes.

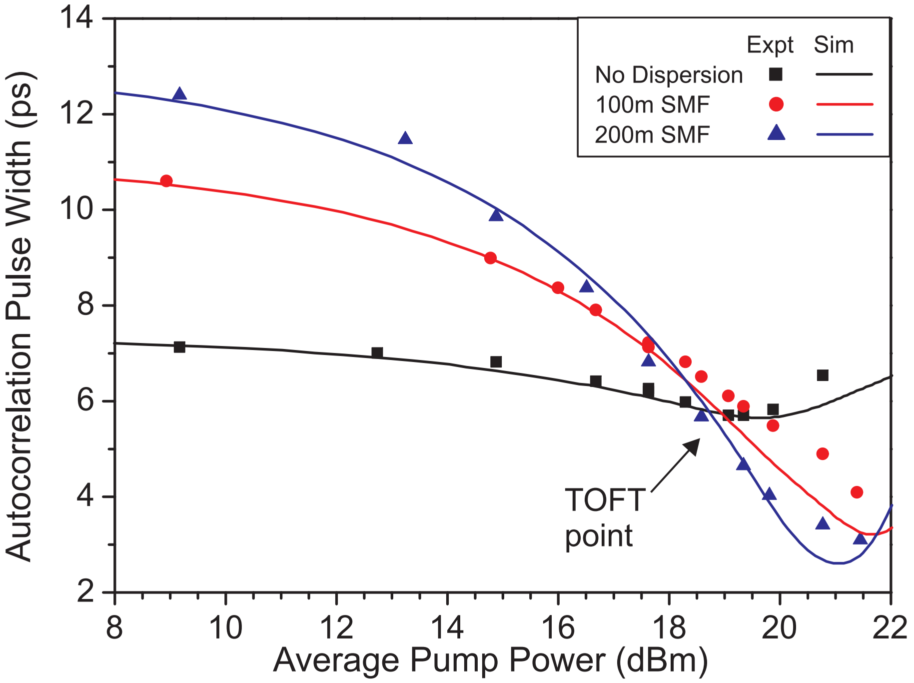

FIGURE 5.11: Dependence of the output pulse width on the pump power for various values of GVD distortion, indicating the correct operating point for TOFT

The GVD-distorted pulses at the input and output of the compensator, shown in Fig. 5.12, were measured at the TOFT operating point (19 dBm). Fig. 5.12(a) shows the autocorrelations of the input pulses with no dispersion and those dispersed by 100 m and 200 m of SMF. After compensation, all the pulses have the same autocorrelation width of 6 ps regardless of the GVD at the input, as shown in Fig. 5.12(b). This output width could potentially be reduced by using a different (but still matched) chirp and dispersion pair. That is, by increasing the pump power and shortening the SMF at the output. The input and output spectra of the GVD distorted pulses are shown in Fig. 5.13. We notice that unlike the autocorrelations, the spectral widths of the output signal do not correlate well with the amount of dispersion applied. This raises some questions about the spectral quality of our TOFT which will be further discussed in Section 5.6.

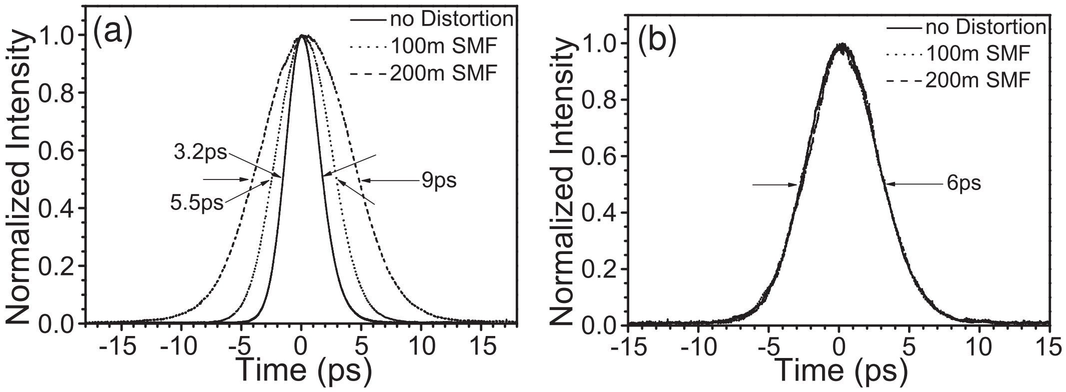

FIGURE 5.12: Autocorrelation traces of the three cases of GVD-distorted pulses at the (a) input of the compensating system and (b) at the output of the compensating system. Note that the labelled widths refer to the FWHM of the autocorrelation traces rather than the FWHM of the pulse intensity profiles.

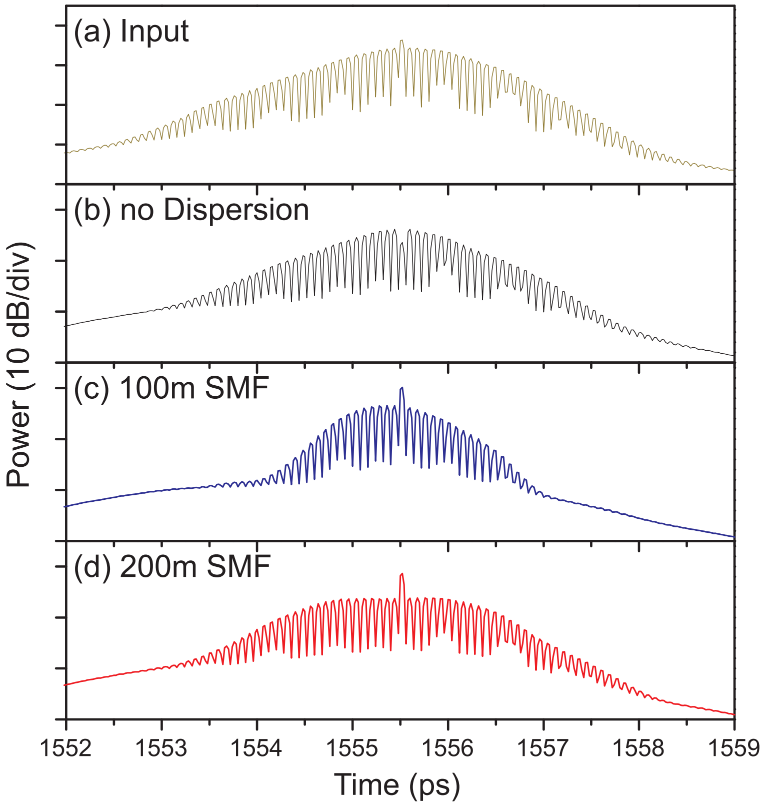

FIGURE 5.13: Signal spectra (a) before the TOFT and after the TOFT for (b) no signal dispersion, (c) dispersed by 100 m SMF and (d) dispersed by 200 m SMF.

5.5 Third Order Dispersion Compensation using TOFT

We then proceeded to apply TOFT to TOD-distorted pulses using the same setup. Because TOFT is not dependent on the input chirp of the pulses, we were able to use the same K and SMF length to transform the TOD distorted pulses. The pulses were dispersed to 8.4 ps/nm^2 by reflection off the grating pair characterised in Fig. 5.4(b). The relatively flat top of the loss spectrum ensured that the pulses experienced only minor spectral filtering but are mainly affected by the time delay to the frequency components of the signal. Fig. 5.14(a) shows the L-FROG characterization of the pulses reflected off the FBGs. The dotted line shows a 10 ps apodized parabolic pulse profile which can be seen to cover most of the distorted pulse but not all. Although we were not able to

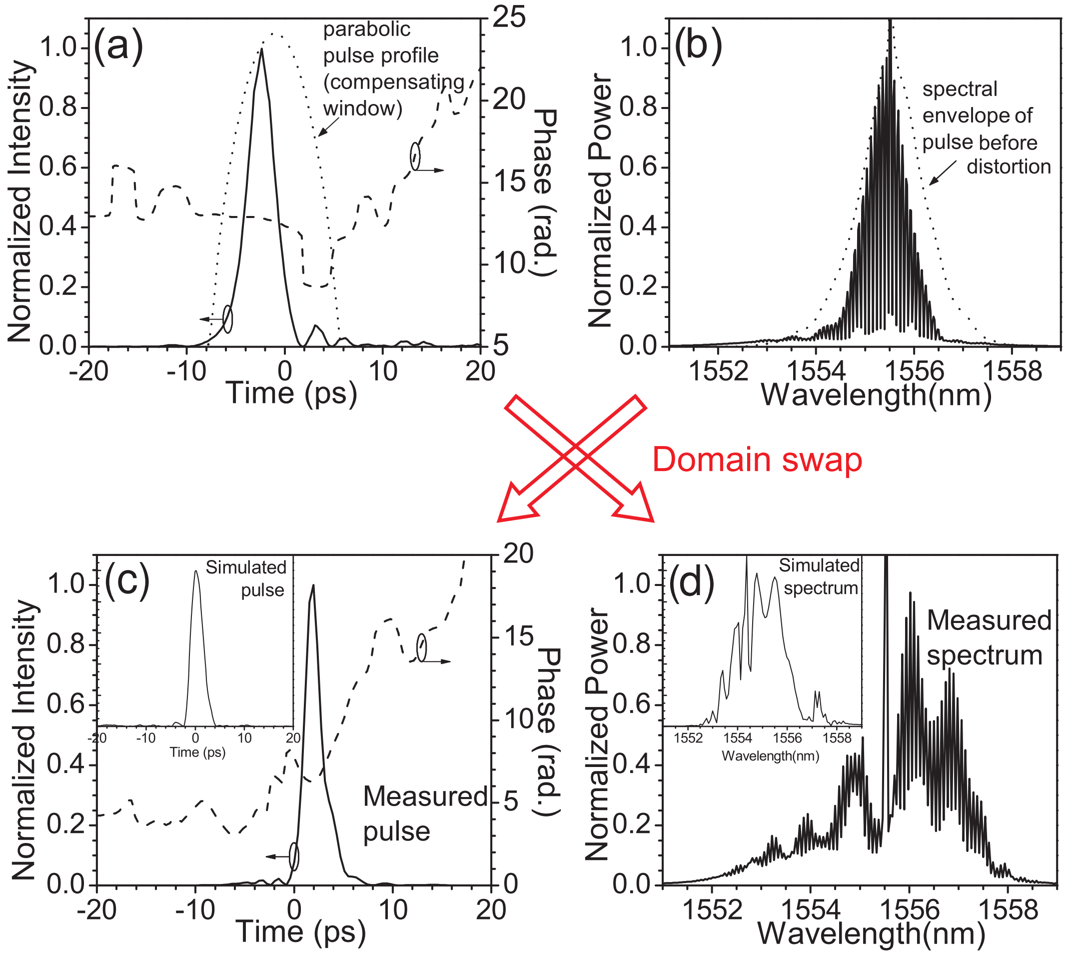

FIGURE 5.14: Temporal profile (a) and spectrum (b) of the TOD-distorted pulses at the input of the TOFT compensator. At the output of the TOFT compensator, the temporal profile (c) and spectrum (d) of the TOD-distorted pulses have swapped. Shape of output spectrum imperfect due to leakage outside the parabolic window, but has expected shape compared to simulation.

achieve complete confinement of the TOD pulses, we were able to contain the majority of the signal power. However, this meant that we could not expect parts of the TOD pulse extending outside the parabolic envelope to be transformed. The minor spectral filtering from the TOD gratings as compared to the original pulse can be seen in Fig. 5.14(b). The spectrum is otherwise largely unchanged. Figs. 5.14(c) and (d) show the corresponding temporal and spectral traces at the output of the device. In Fig. 5.14(c), the temporal pulse can be seen to be compressed and exhibits a waveform resembling the profile of the input spectrum in (b). Fig. 5.14(d) shows the transformed output spectrum to which the main temporal distortions have been passed. Although the spectrum does show ringing features resembling the distorted input pulse, it is clear that the transformation in the spectral domain is imperfect. This is partially due to the limited TOFT window provided by our 10 ps parabolic pulses. Any parts of the distorted pulse outside of this window did not experience the linear chirp which resulted in imperfect transformation. Another likely reason for the imperfect transform is the extra phase term in the spectrum as described in Section 2.23. We discuss this extra phase term further below and then in more detail in Chapter 7. The simulated converted pulse and spectrum using the apodized parabolic in (a), is shown in the inset for comparison.

5.6 Discussion

In the two experiments above where we have performed dispersion compensation on GVD and TOD distorted pulses, the results have a common characteristic. In both cases, the transformation of the spectral profile into the time domain was very good. However, the transformation of the temporal profile into the spectral domain has been less convincing. These results were unexpected because although the spectra have shown a reasonable match to simulation, we expect in theory that pulses experiencing TOFT should have a swap in *both* their temporal and spectral domains. That is, a dispersed pulse which is temporally broader than its undispersed form, should emerge from the TOFT with a broader spectrum than the undispersed. Furthermore, this should hold true regardless of the sign of the chirp on the dispersed pulse. However, this is not what we observe experimentally. Instead, we see that the spectral broadening and output pulse width is very dependent on the chirp of the distorted signal. Fig. 5.13 showed the spectral broadening of the pulses dispersed by SMF. It is clear that while the greater dispersion of the pulses passing through 200 m of SMF did result in a wider spectrum,

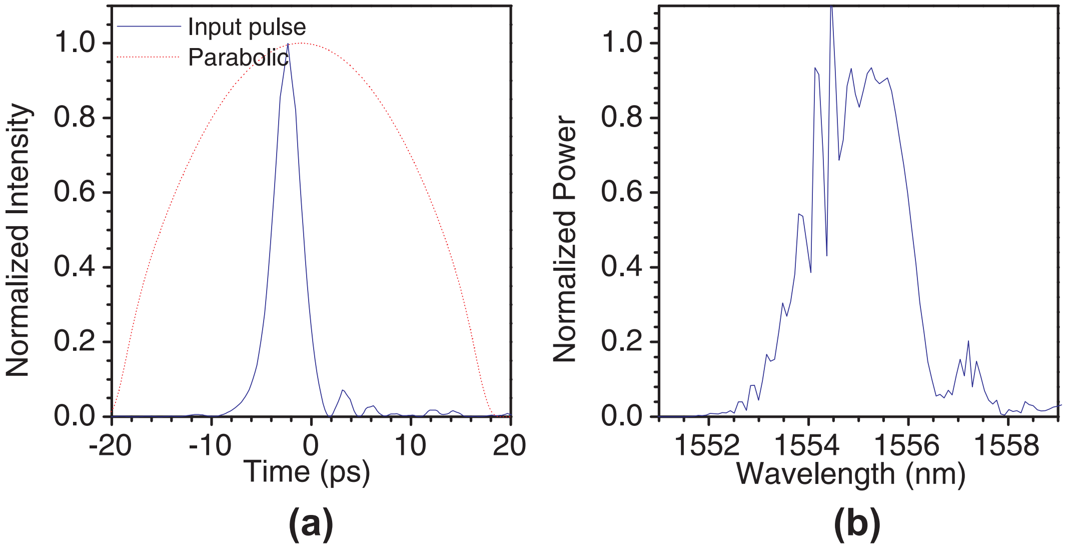

FIGURE 5.15: Simulation of the TOFT assuming a wider parabolic. (a) The simulated input pulse and wide parabolic pump. (b) The resulting spectrum after TOFT.

the pulses dispersed by 100 m SMF spectrally narrowed. Similarly, we observe that the spectrum of the TOD pulses after TOFT only loosely followed the temporal features of the incoming waveform. Fig. 5.15 shows a simulation of what the TOFT output would look like for a wider parabolic window than shown in Fig. 5.12(a), but with the same K. We see that the spectrum is still very poor in this case indicating that the confinement is not our main problem here. It is more likely that the output pulses were affected by the extra phase term we observed in the TOFT of the spectrum (Eqn. 2.22) in Chapter 2. The extra phase term given by $\exp[-\omega'^2/2K]$ is imaginary in the temporal domain and resides outside the Fourier transform integral thus affecting only the phase of the output and not its intensity. However in the spectral domain, the exponential is moved inside the Fourier transform integral and so affects the the waveform intensity itself. We had observed that using a high chirp rate, K, would reduce the effects of this phase term, but this poses practical problems in requiring stronger pump amplification and thereby giving rise to greater SPM in the pump. In Chapter 7 we investigate this problem further and change our TOFT configuration to compensate for the phase term *without* increasing the pump power.

5.7 Conclusions

In this chapter we have reviewed the operation and design of FBGs and SSFBGs. A SSFBG designed to generate 10 ps parabolic pulses was used to obtain the pulses we needed for time lensing. This was shown to provide benefits over the nonlinear parabolic pulses by allowing a variable pump power. We also improved the confinement of the test pulses in the TOFT window by using a NOLM to create a second short pulse source from the MLL we were already using for the pump. Our improved setup enabled us to examine the pulse width evolution of dispersed pulses through the TOFT and verify the TOFT operational point. Finally, we have experimentally demonstrated the mitigation of second and third order dispersion of short optical pulses with our TOFT compensator using the SSFBG shaped parabolic pulses. The quality of the transformations were very good in the time domain making this suitable for use as a compensator before an end detector. However, a discrepancy was observed in the width of the transformed spectra. By eliminating the extra phase term in the TOFT output spectra, we should be able to achieve even better fidelity in transforming pulses with the TOFT compensator.

In Chapter 7 we will investigate this phase term further and re-evaluate the TOFT system to correctly and completely compensate for it. However before that, we take a break from TOFTs to investigate a new pulse source derived from an optical frequency comb. The frequency comb can be filtered in some interesting ways which will help us to obtain high quality parabolic pulses and further improve the fidelity of our TOFTs.

Bibliography

[1] T. Erdogan. Fiber grating spectra. *Journal of lightwave technology*, 15(8):1277–1294, 1997.

[2] G. P. Agrawal and S. Radic. Phase-Shifted Fiber Bragg Gratings and their Application for Wavelength Demultiplexing. *IEEE Photonics Technology Letters*, 6(8): 995–997, 1994.

[3] J.J. Pan and Y. Shi. Dense WDM multiplexer and demultiplexer with 0.4nm channel spacing. *Electronics Letters*, 34(1):74–75, 1998.

[4] B. J. Eggleton, A. Ahuja, P. S. Westbrook, J. A. Rogers, P. Kuo, T. N. Nielsen, and B. Mikkelsen. Integrated tunable fiber gratings for dispersion management in

high-bit rate systems (vol 18, pg 1418, 2000). *Journal Of Lightwave Technology*, 18 (11):1591–1591, 2000.

[5] M. Ibsen, M. K. Durkin, M. J. Cole, M. N. Zervas, and R. I. Laming. Recent advances in long dispersion compenating fibre Bragg graitngs. In *IEE Colloquium on Optical Fibre Gratings*, page Paper 6, Birmingham, 1999.

[6] A. Yariv. Coupled mode thoery for guided wave optics. *IEEE Journal of Quantum Electronics*, 9:919–933, 1973.

[7] C. M. de Sterke, K. R. Jackson, and B. D. Robert. Nonlinear coupled-mode equations on a finite interval: a numerical procedure. *Journal of the Optical Society of America B*, 8(2):403–412, 1991.

[8] C. M. deSterke and N. G. R. Broderick. Coupled-mode equations for periodic superstructure Bragg gratings. *Optics Letters*, 20(20):2039–2041, 1995.

[9] C. S. Goh, S. Y. Set, and K. Kikuchi. Design and fabrication of a tunable dispersion-slope compensating module based on strain-chirped fiber Bragg gratings. *IEEE Photonics Technology Letters*, 16(2):524–526, 2004.

[10] B. J. Eggleton, P. A. Krug, L. Poladian, and F. Ouellette. Long period superstructure Bragg gratings in optical fibres. *Electronics Letters*, 30(19):1620–1622, 1994.

[11] H. Geiger, M. Ibsen, and R. I. Laming. Optimum recievers with fiber gratings. In *Optical Fiber Communications (OFC)*, pages 152–154, 1998.

[12] P. C. Teh, P. Petropoulos, M. Ibsen, and D. J. Richardson. Phase encoding and decoding of short pulses at 10 Gb/s using superstructured fibre Bragg gratings. *IEEE Photonics Technology Letters*, 13(2):154–156, 2001.

[13] P. Petropoulos, M. Ibsen, A. D. Ellis, and D. J. Richardson. Rectangular pulse generation based on pulse reshaping using a superstructured fiber Bragg grating. *Journal Of Lightwave Technology*, 19(5):746, 2001.

[14] F. Parmigiani, P. Petropoulos, M. Ibsen, and D. J. Richardson. All-optical pulse reshaping and retiming systems incorporating pulse shaping fibre Bragg gratings. *Journal Of Lightwave Technology*, 24(1):357–364, 2006.

[15] F. Parmigiani, P. Petropoulos, P. J. Almeida, M. Ibsen, and D. J. Richardson. Amplitude and timing jitter reduction using a fiber NOLM incorporating a fiber Bragg grating based pulse shaper. In *Optical Fiber Communications Conference (OFC)*, Anaheim, 2005.

[16] F. Parmigiani, C. Finot, K. Mukasa, M. Ibsen, M. A. F. Roelens, P. Petropoulos, and D. J. Richardson. Ultra-flat SPM-broadened spectra in a highly nonlinear fiber using parabolic pulses formed in a fiber Bragg grating. *Optics Express*, 14(17): 7617–7622, 2006.

[17] F. Parmigiani, P. Petropoulos, M. Ibsen, and D. J. Richardson. Pulse retiming based on XPM using parabolic pulses formed in a fiber Bragg grating. *IEEE Photonics Technology Letters*, 18(7):829–831, 2006.

[18] T. T. Ng, F. Parmigiani, M. Ibsen, Z. Zhang, P. Petropoulos, and D.J. Richardson. Compensation of linear distortions by using XPM with parabolic pulses as a time lens. *IEEE Photonics Technology Letters*, 20(13):1097–1099, 2008.

Chapter 6

Pulse Generation with an Optical Frequency Comb Generator

In this chapter we take a small break from optical Fourier transforms to look at an interesting new source which we have not yet introduced. The source is an optical frequency comb generator (OFCG) with very high stability and a very large bandwidth. Such a source is interesting to use because its large bandwidth makes it an excellent canvas on which to perform spectral shaping. As will be shown in this chapter, the combination of the large bandwidth comb and tuneable filters can create a very versatile and flexible pulse source, which will be extremely useful in our further studies of TOFT in the next chapter. This chapter begins with an overview of the OFCG. We gain further understanding of the OFCG in Section 6.1.1 in which we will use the L-FROG to characterise this useful resource. The latter sections of this chapter explore how tuneable filters can be used to turn the OFCG into a versatile source from which we can independently tune the output pulse width, wavelength and pulse shape. Furthermore, the source is used, in the last section, to simultaneously generate both the pump and the signal for our next temporal optical Fourier transform experiment.

6.1 The Optical Frequency Comb Generator

Stable optical frequency combs are interesting for many applications including accurate laser frequency measurements [1], optical coherence tomography [2] and as high repetition rate short pulse sources [3]. It was the quest for high repetition rate short pulses that led Gordon and Rigden to first propose generating these combs with a Fabry-Perot electro-optic modulator (FP-EOM) in 1963 [4]. In 1972, Kobayashi *et al.* used Gorden and Rigden's FP-EOM by placing it inside a laser cavity to increase the efficiency of the side band generation in his laser [5]. While many other schemes have been proposed in the following years for high repetition rate short pulse generation, it was in the early 1990s when Kourogi *et al.* revisited the idea of the FP-EOM [6]. Kourogi's interest was not in short pulse generation however, but rather in wide sideband generation for accurate frequency measurements. Kourogi considered the FP modulator without Kobayashi's laser cavity and used instead a CW laser input from which to create sidebands. The principle for Kourogi's OFCG is shown in Fig. 6.1. A $LiNbO_3$ phase modulator is placed inside a high finesse optical cavity and driven at n times the free spectral range (FSR) of the cavity [6, 7]. In this way, every time the light passes through the modulator it will experience a chirp that brings it very briefly through the resonance of the cavity and a pulse will be generated at this point in time. The higher the finesse of the cavity, the narrower will be the linewidth of the cavity resonance and thus the shorter the resulting pulse. Similarly, an increase in the driving amplitude will increase the chirp gradient at the crossing which also results in a narrower pulse. Thus the power is more efficiently coupled into the higher order modes. In each second half period, the RF signal must oscillate back through the resonance again, and generating a second pulse half a period away and with the opposite chirp to the first pulse. Fig. 6.2 represents this more clearly by unwrapping the cavity onto a time axis. The plot on the upper axis illustrates the chirp imparted by the modulator with the periodicity, T. On the lower axis, we see that whenever the chirp passes through the resonance condition of the cavity (blue), a pulse is generated resulting in two pulses per period and with opposing chirps. With each successive round trip in the cavity, the chirp is further reinforced and more of the CW light is coupled into the sidebands. The resulting optical frequency comb (OFC) has a symmetric spectrum consisting of discrete spectral lines

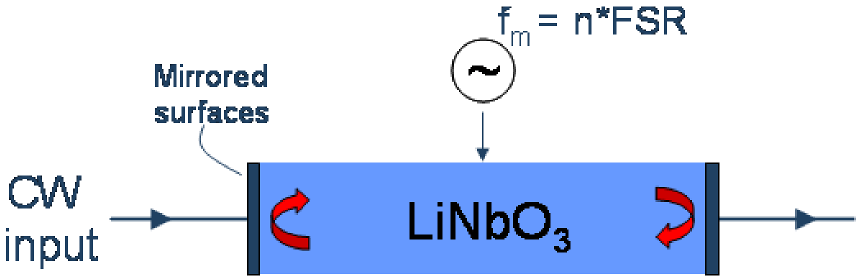

FIGURE 6.1: Principle of the optical frequency comb generator.

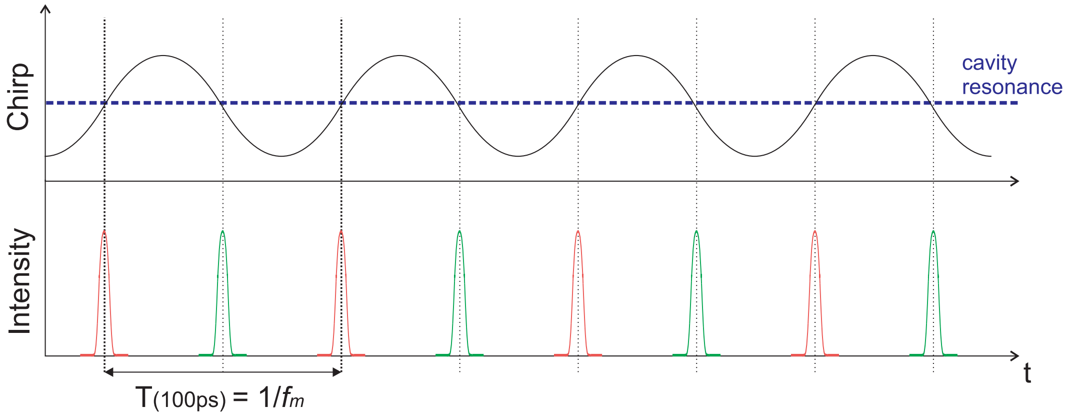

Figure 6.2: Pulse generation in the OFCG. A pulse is produced every time the modulating chirp brings the beam through the cavity resonance. The up and down chirps in each cycle generate a pair of oppositely chirped pulses per period.

separated by the modulation frequency, f_m, with wings that decay exponentially in the frequency domain. In one half of the spectrum, all the spectral lines are in phase with each other, while in the other half of the spectrum adjacent spectral lines are π out of phase with each other. From Fourier transform theory, it follows that each half of the OFCG spectrum generates a pulse with a Lorentzian envelope [3], an arctan phase profile and is temporally offset by half a period from the other half of the spectrum. The complete spectrum thus gives two pulses per period. However, the two pulses in these pairs are not identical, but have opposing chirps arising from the part of the RF cycle from which they are generated [7].

To understand this peculiar spectrum further, we considered it analytically. The power of the n^{th} sideband P_n of the OFCG can be approximated by [6]

$$P_n = \eta_{FP} \left(\frac{\pi}{2mF} \right)^2 \exp\left[-\frac{|n|\pi}{mF} \right] P_0 \tag{6.1}$$

where η_{FP} is the efficiency of the Fabry-Perot cavity, m is the single pass modulation index, P_{in} is the input laser power and F is the finesse of the Fabry-Perot which describes how well the signal is confined to the cavity, and is related to the reflectance, R, of the mirrored surfaces by the relation $F = \frac{4R}{(1-R)^2}$. To obtain the envelope function from the discrete lines, we can consider that $|n| = \frac{f}{f_m}$, where f_m is the line spacing of the comb such that when $f = nf_m$ we have a spectral line. So

$$P(f) = \eta_{FP} \left(\frac{\pi}{2mF} \right)^2 \exp\left(-\frac{\pi}{mf_mF} f \right) P_0$$

This can be expressed as

$$P(f) = \eta_{FP} P_0 \left(\frac{\alpha f_m}{2} \right)^2 \exp\left(-\alpha f\right) \tag{6.2}$$

where $\alpha = \frac{\pi}{m f_m F}$ is the decay rate of the spectrum. To simplify the problem, we begin by considering only one half of the spectrum. That is, we can assume zero phase and $n > 0$. Thus the electric field of the spectrum is just the square root of the power spectrum for $n > 0$. So

$$u(\omega) = \frac{\alpha f_m}{2} \sqrt{\eta_{FP} P_0} \exp\left(-\frac{\alpha}{4\pi}\omega\right) \tag{6.3}$$

It can be seen that the decay rate α gives the slope of the spectrum on a logarithmic scale. To find the pulse in the time domain, we take the Fourier transform of $u\left(\omega\right)$ (from 0 to ∞, since the spectral density is zero for $\omega < 0$), so

$$u(t) = \frac{\alpha f_m}{2} \sqrt{\eta_{FP} P_0} \left[\frac{1}{\sqrt{2\pi}} \int_0^\infty e^{-\frac{\alpha}{4\pi}\omega} e^{-i\omega t} d\omega \right] \tag{6.4}$$

which eventually gives,

$$u\left(t\right) = \frac{\alpha f_m}{2\sqrt{\left(\frac{\alpha}{4\pi}\right)^2 + t^2}} \sqrt{\frac{\eta_{FP} P_0}{2\pi}} \exp\left(i \tan^{-1}\left(-\frac{4\pi t}{\alpha}\right)\right) \tag{6.5}$$

For the other half of the spectrum, we can replace the phase alternation of the spectral lines by offsetting it from the first half spectrum by a half period. Then putting the two halves together, we obtain the electric field for the whole signal as

$$E(t) = \alpha f_m \sqrt{\eta_{FP} P_{in}} \left(\frac{\exp\left[i \tan^{-1}\left(\frac{\mathrm{t-T/4}}{\alpha}\right)\right]}{\sqrt{\alpha^2 + (t - T/4)^2}} + \frac{\exp\left[i \tan^{-1}\left(-\frac{\mathrm{t+T/4}}{\alpha}\right)\right]}{\sqrt{\alpha^2 + (t + T/4)^2}} \right) \tag{6.6}$$

where T is the period. Furthermore, the two phase terms contained in $E(t)$ can be seen to be time reversed, highlighting that they originate from and depend directly on α.

Fig. 6.3(a) shows the resulting temporal profile of the pulse as expressed in Eqn. 6.6. However in practice due to the broad spectrum of the OFC, its generation will inherently introduce dispersion to the pulses from the $\mathrm{LiNbO_3}$ crystal itself and any fibre in the system. With a modest amount of dispersion the pulses will begin to look like Fig. 6.3(b), exhibiting mirror image profiles that stem from the opposing slopes on the two sides of the spectrum.

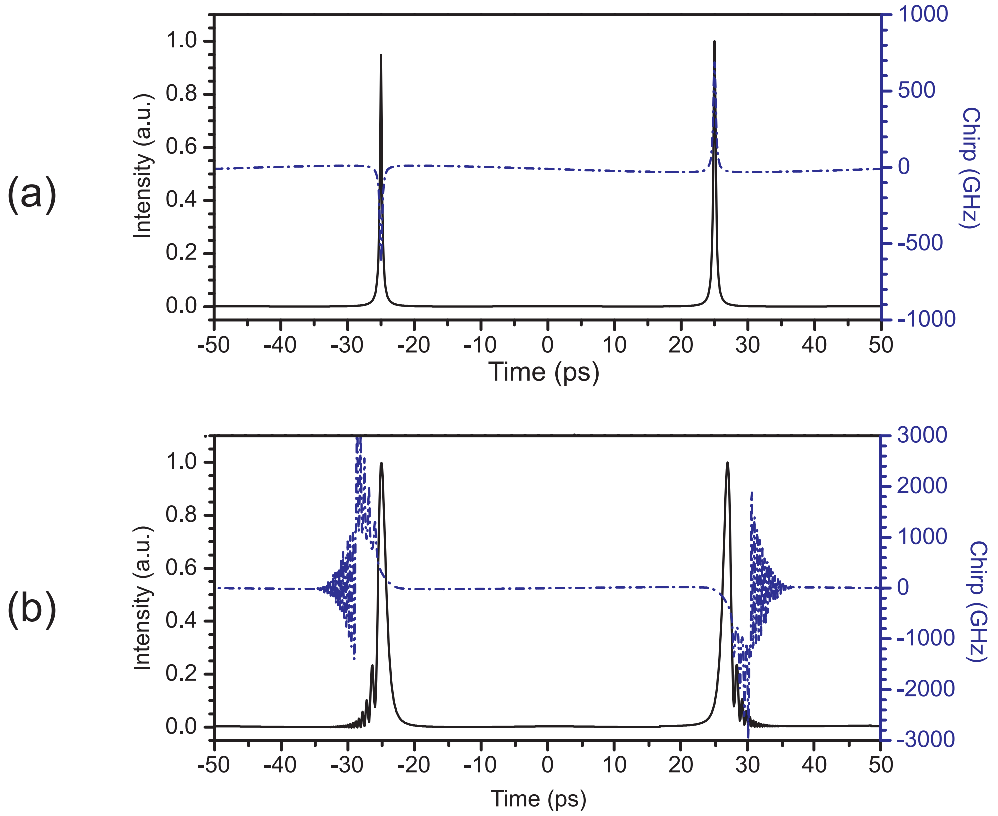

Figure 6.3: Theoretical temporal profile of the OFCG output with (a) no extra dispersion and (b) with dispersion.

6.1.1 Characterisation of the OFCG

We obtained an OFCG commercially from Optical Comb Inc. (LP-5011), which consisted of a high finesse, $LiNbO_3$ optical cavity as described previously, and driven at 10.0 GHz with an internal frequency source and could be fed with a CW input at any wavelength from 1530-1565 nm. On locking, the unit generated an exponentially decreasing spectrum with a base bandwidth of > 50 nm. Unfortunately, due to the high insertion loss of the device (30 dB) and the input damage threshold of the device, the output power was very low and the measurable spectrum was limited by the sensitivity of our optical spectrum analyzer. We were thus not able to measure the full extent of the OFC bandwidth. The spectrum we have measured is shown in Fig. 6.4(a) and its autocorrelation shown in Fig. 6.4(b). Note that this spectrum was measured without the use of an EDFA which would distort the shape of the comb. However, all other measurements we have taken of the OFC (including Fig. 6.4(b)) do use an EDFA to bring the low output power within the sensitivity of our diagnostics.

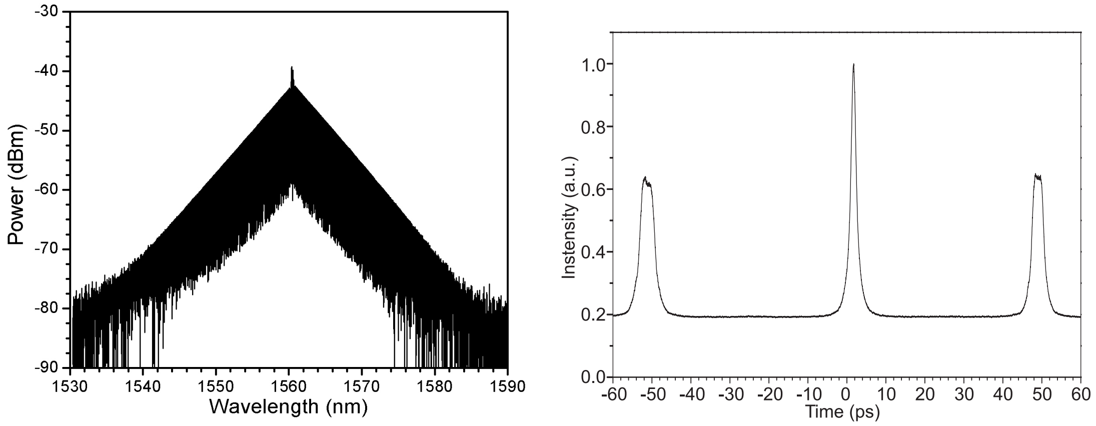

(a) (b)

Figure 6.4: (a) Measured spectrum of the OFC without amplification (b) Autocorrelation of the OFC

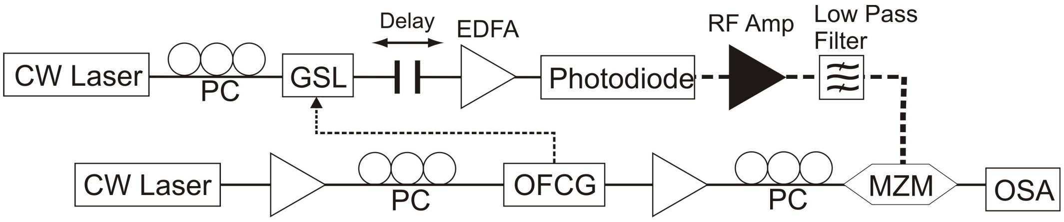

Figure 6.5: Setup to characterise the OFCG output.

Previous studies into the OFCG have focused mainly on the intensity profiles of their output pulses. We wanted to extend this by exploring also the phase characteristics of these pulses. To this end, we attempted to perform L-FROG measurements on the OFCG output. Fig. 6.5 shows the setup used to characterise the OFCG. Because we expected the OFCG to generate two pulses per period which are not identical, we require a gate pulse that only has *one* pulse per period. A GSL was driven at 10 GHz from the internal synthesizer of the OFCG to produce the gate we required. Fig. 6.6 shows the measured spectrogram of the OFCG output. This spectrogram very clearly shows the two pulses which are generated by the OFCG and their correlation with each half of the spectrum. It is interesting also how clearly defined this correlation is with each pulse being completely confined to its half of the spectrum.

After deconvolution, the retrieved output of the OFCG is shown in Fig. 6.7. In Fig. 6.7(a), the temporal profile shows two pulses per period spaced half a period apart from each other as expected. However, we see that the two pulses are not mirror images as expected and do not have opposing chirps. Instead, one of the pulses is asymmetric and chirped while the other is symmetric and unchirped. Fig. 6.7(b) shows the L-FROG

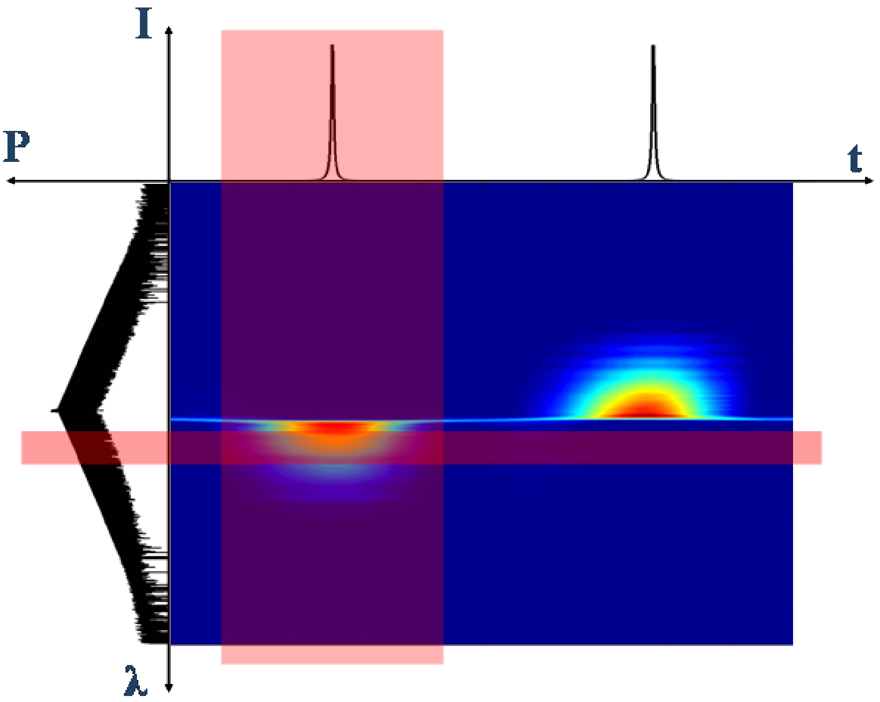

FIGURE 6.6: Spectrogram of the OFCG showing the pulses offset by T/2. It is possible to filter out just one of the pulses by filtering a portion from just one side of the spectrum only (red shading).

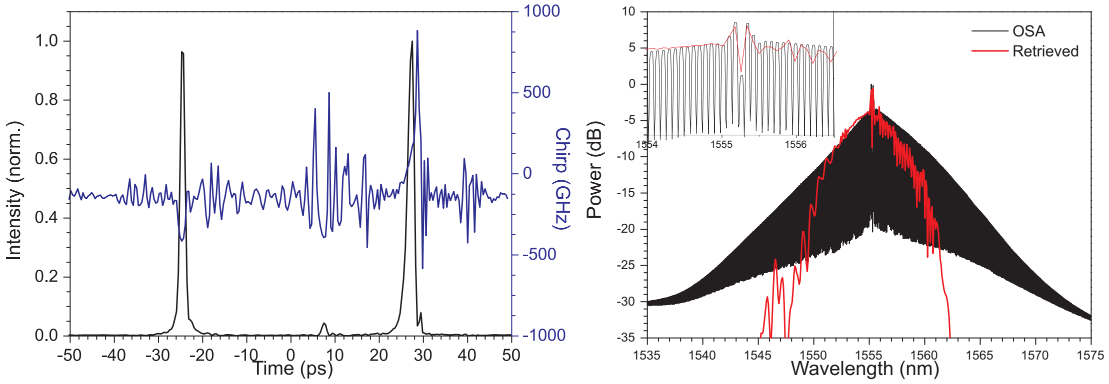

(a) (b)

FIGURE 6.7: (a) L-FROG retrieved profile of the OFCG output. (b) Spectrum of the OFCG output. The inset shows the matching between the OSA measured and the retrieved spectra in the central region.

retrieved and the OSA measured spectra. Although the spectra do not match very well, we do not believe this to be the reason for the unexpected temporal characteristics. Indeed, we investigated this by measuring each half of the spectrum separately. By reducing the spectrum by a half, the resolution of the L-FROG measurement can be greatly increased, thus improving its fidelity. The retrieved spectra are shown in Fig. 6.8

and their corresponding temporal profiles are shown in Fig. 6.9. The improved quality of the measurement can be seen by the smoother retrieved envelope and its improved matching to the OSA measurement. Although it can be seen that the limited dynamic range of the measurement has also limited the measurement of the spectral wings here, the discrepancy only begins ∼ 10 dB down from the peak and so should not significantly alter the major features of the measurement. Furthermore, it can be seen that the retrieved pulses are essentially the same as when they were measured together. That is, the measurements of Fig. 6.7 and Figs. 6.8-6.9 both measure the output of the OFCG, but in different ways to enhance the resolution of the measurement. The similarity of the results from both sets of measurements indicate that the asymmetrical temporal phase profile observed is real and not due to any inadequacy in the measurements.

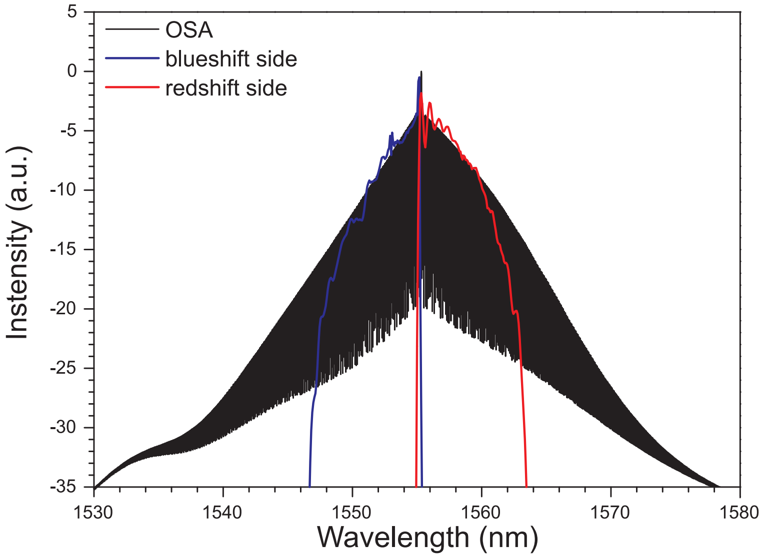

FIGURE 6.8: Retrieved spectra of the two OFC pulses. The spectra are compared to the OSA measured spectrum.

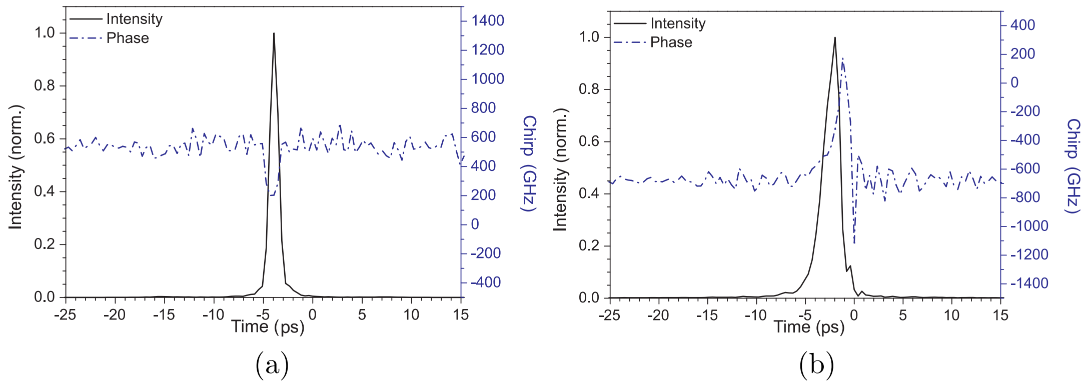

(a) (b)

FIGURE 6.9: L-FROG retrieved profiles of the pulses on the (a) red side and (b) blue side of the spectrum respectively.

On closer inspection, Fig. 6.8 presents us another possible explanation for the chirp discrepancy between the two pulses. Note that since an EDFA was required in these measurements, there has been some change to the spectral shape arising from the non-flat gain spectrum of the EDFA. More specifically, we note that the rate of decay of the spectrum is now different on the two different sides. As we have seen in the theory and the simulation of the pulses in Fig. 6.3, this directly affects the chirp of the pulses breaking the symmetry between them. Once the pulses no longer have perfectly opposing chirps, it is possible that dispersion in the measurement system could cause compensation of the dispersion in one pulse but leaves the other incompletely compensated.

6.2 Variable Pulse Generator using a Tunable Flat Top Filter

In this section we use a tuneable filter to add pulse tuneability to the OFCG. The dependence of the output pulse characteristics on the bandwidth of the spectral slice was investigated by passing the OFC through different filter bandwidths. It is shown that the combination of a OFCG with a filter which is tunable both in wavelength and bandwidth gives rise to a high quality short pulse source with adjustable pulse characteristics.

6.2.1 The Tuneable Flat-Top Filter

The filter we used was a Santec flat-top tunable filter (OTF-950) which we were able to continuously and independently tune in bandwidth and wavelength across the C-band. Fig. 6.10(a) shows a diagram of the operation of the filter [8]. The input to the filter is first incident upon a diffraction grating formed from a reflecting wedge. The spectrally spread beam is then reflected off one slice of a movable triangular mirror. Because the beam is only incident on one slice of the mirror at any given time, moving the mirror perpendicular to the incident beam will change the width of the reflected portion. This concept is more clearly shown in Fig. 6.10(b). Recompression of the filtered beam off the initial grating couples the light back out into the original input fibre. Finally a circulator redirects the output to a separate port from the input. The wavelength tunability of the filter is achieved by varying the tilt of the mirror constructing the bottom edge of the wedge grating. As shown in Fig. 6.10(c), changing the angle of the wedge will cause a different portion of the spectrum to be directed to the bandwidth selecting mirror, thus selecting a different centre wavelength.

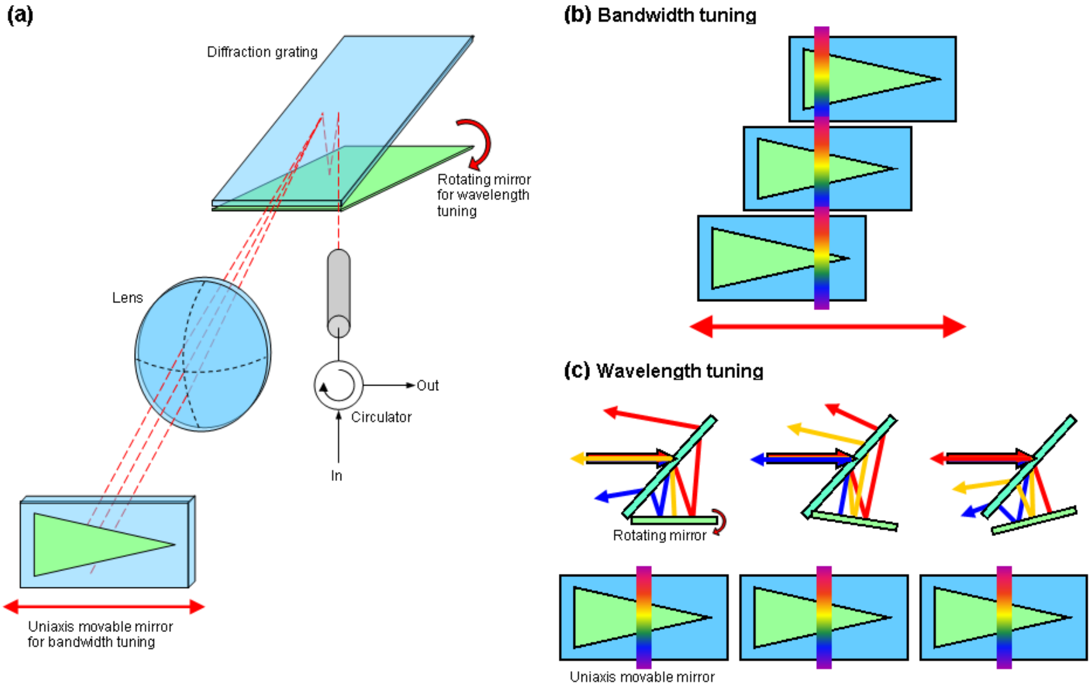

FIGURE 6.10: (a) Schematic of the Santec tunable filter (b) Bandwidth tuning is obtained in the filter by moving the triangular mirror perpendicular to the beam thus reflecting a slice of differing width. (c) Wavelength tuning is obtained in the filter by changing the tilt angle of the mirror in the wedge reflector, thus changing the portion of the spectrum reflected off the triangular mirror. (Edited from figure in [8])

6.2.2 Experimental Setup

The experimental setup we used is shown in Fig. 6.11. A 1560 nm CW signal was amplified up to 15 dBm which was the maximum specified input to the OFCG without damaging it. Since the LiNbO$_3$ modulator is polarisation sensitive, a polarisation controller was used just before the OFCG to maximise the output power from the device. At the output of the OFCG the signal had been reduced to -15 dBm and had to be amplified again to bring it within the sensitivity of our characterisation devices. This second

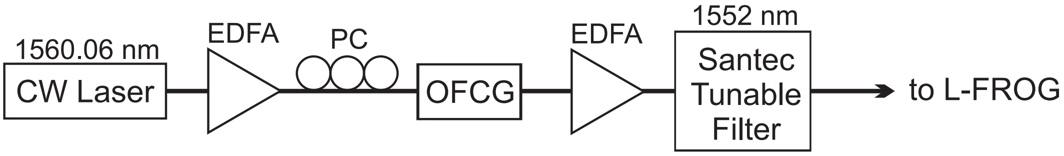

FIGURE 6.11: Setup of the variable pulse generator

amplifier was also important since we anticipated that more optical power would be lost in the Santec filter when most of the OFC spectrum was rejected. The filter was centred around 1552 nm, in a region as close as possible to the central wavelength to maximise the power, but far enough away to ensure that the second half of the spectrum was fully rejected. In addition, the wavelengths of the CW laser and the filter were chosen such that the part to be filtered experienced a flat gain across its bandwidth as it passed through the EDFA, and the shape of the OFC spectrum was preserved. Pulses were measured with filter bandwidths ranging from 0.5 nm to 6 nm on the short wavelength side of the OFC spectrum allowing us to pick out one component of the pulse pair. We analysed the filtered output on the L-FROG measurement setup, and the measured pulses are shown along with simulations in Fig. 6.12.

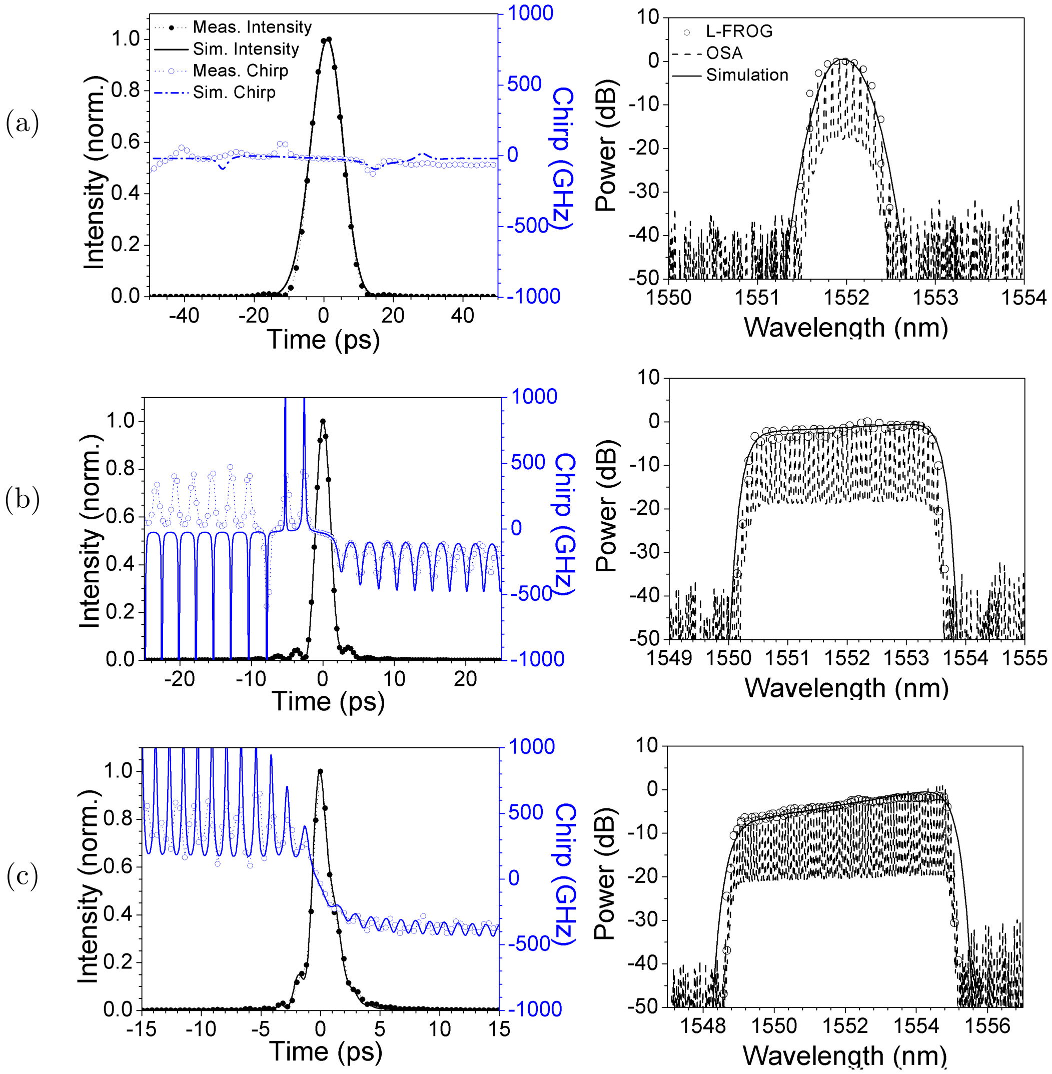

FIGURE 6.12: Filtered output pulse profiles and corresponding spectra for bandwidths of (a) 0.5 nm, (b) 3 nm and (c) 6nm

6.2.3 Results and Discussion

Fig. 6.12 shows the output pulses resulting from 0.5 nm, 3 nm, and 6 nm filter bandwidths respectively. Both the measured pulse intensities and phases (dots) can be seen to match very well with the theory (lines). Their corresponding spectra are shown next to them. The filtered pulses can be seen to be of high quality and very short, with pulse widths of 10.5 ps, 2.3 ps and 1.6 ps respectively. Note that the linear chirp observed on the pulses is not intrinsically due to the OFC generation technique, but rather to other dispersions in and following the system as was shown in Fig. 6.3. Sources of this extra dispersion include the $LiNbO_3$ crystal itself, the dispersion within the Santec tunable filter and the SMF fibre between the OFCG output and the L-FROG. The simulations take this into account by applying a consistent dispersion across all three pulses, which was fitted by eye to a value of 1.02 ps/nm. The corresponding simulation of our filtered pulses with only the intrinsic chirp of the comb generation technique and without the extra dispersion is shown in Fig. 6.13. The very small intrinsic chirp of these undispersed pulses can be seen to be < 100 GHz across the full pulse-width in all cases examined.

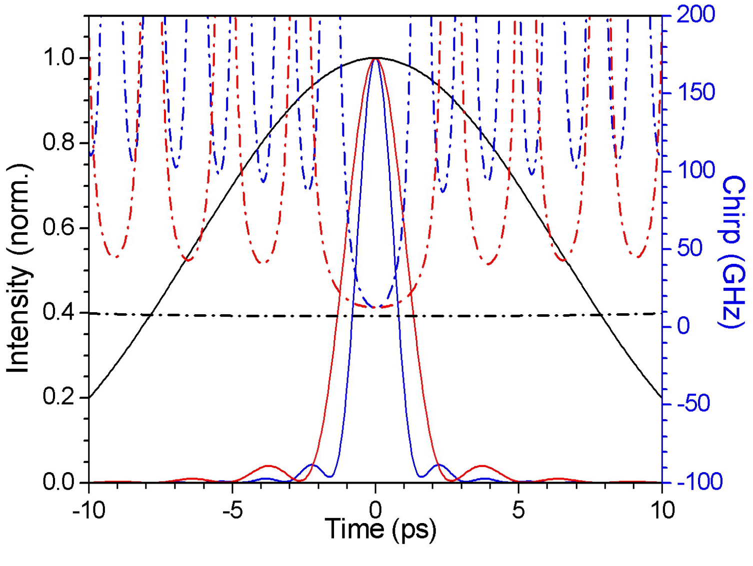

FIGURE 6.13: Simulated OFCG output without any additional dispersion.

The side lobes which can be observed on all the pulses are due to the super-Gaussian shape of the tunable filter. Indeed, we see that the side lobes are reduced for the 0.5 nm filter which has a more rounded spectrum. In order to improve the quality of the filtered pulse for a given bandwidth, it is possible to design an (amplitude-only) filter to apodize the spectrum and correct for the spectral slope which gives rise to the chirp. Fig. 6.14 shows that a filter which combines compensation of the spectral slope with a sech^2 shape can give a much improved output pulse. The simulated output shown in Fig. 6.14(b) is chirp free, smooth and exhibits no evidence of side lobes down to the -30 dB level. Note however, that such designs still require some form of truncation or apodisation to completely reject the second half of the spectrum. In this example, a 6 nm 6^{th} order super-Gaussian was used to apodize the design. Unfortunately, the Santec tunable filter used in these experiments is not able to provide such a filter design. However, these designs are possible to implement using SSFBG, or better yet, more highly configurable filters as will be presented in the next section.

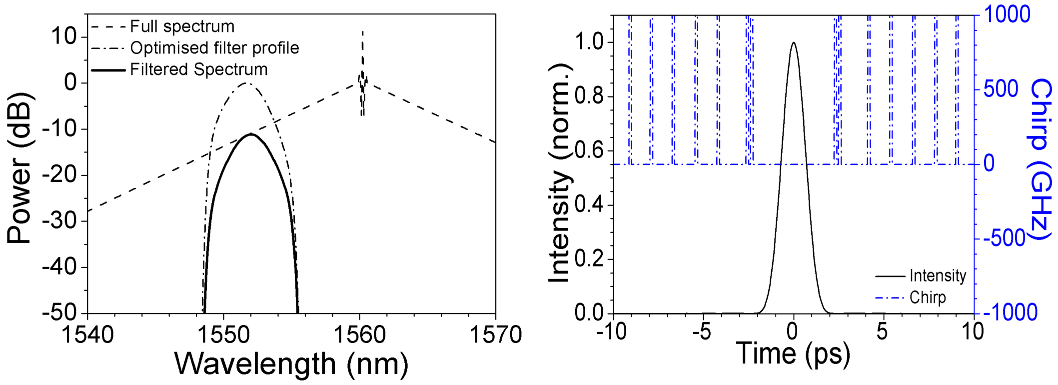

(a) (b)

FIGURE 6.14: (a) Spectral profile of a filter that provides apodised pulses, and the corresponding filtered output; (b) Output pulses from the compensating filter.

6.3 Configurable Spectral Filtering for Creating Multiple Pulse Sources

In this section we extend the pulse shaping work of the last section with the use of a more sophisticated filter. The combination of the wide bandwidth OFC and this new configurable filter allows for almost-arbitrary pulse shaping of picosecond-scale pulses.

6.3.1 The Configurable Filter

The filter in question is a WaveShaper (WS 4000E) from Finisar. Fig. 6.15 shows the configuration of the WaveShaper [9]. A spread input beam is reflected off a Liquid Crystal on Silicon (LCoS) element composing of *nxn* liquid crystal pixels. The liquid crystal pixels can each be electronically aligned to induce a phase shift to the light passing through it. The LCoS is thus able to impart a spectral phase profile onto the signal. After reflection, the beam retraces its input path and is coupled into an output fibre.

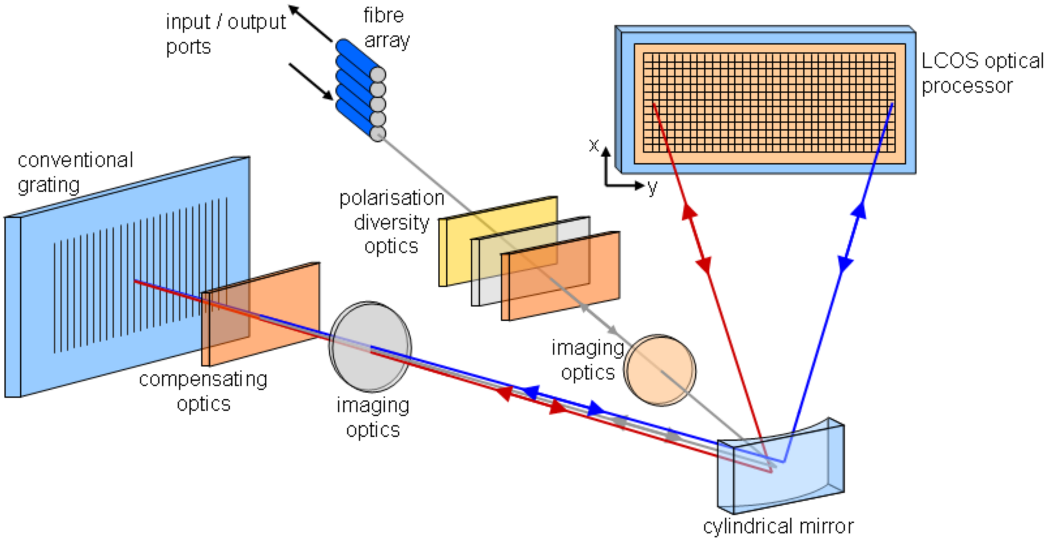

FIGURE 6.15: Schematic of the WS 4000E.(Edited from figure in [9])

Spectral filtering in the WaveShaper is achieved by setting a phase ramp across all the pixels in one line of the LCoS. The liquid crystal line can then steer the incident light spatially in the same way that refraction at an interface bends light. The redirection of the light causes a misalignment between the reflected light and its output fibre thus effectively attenuating it. Since each line of the LCoS pixels affect a different slice of the incident spectrum, wavelength dependent attenuation is achieved, that is, spectral shaping. In the WaveShaper, each individual line of the LCoS can be user configured with a desired phase and attenuation up to a maximum *configurable* attenuation of 34 dB and down to a 0.2 nm resolution. However, the lines are also grouped into 'channels' of 100 GHz width to coincide with telecommunications standards. These 'channels' can be turned "off" to obtain complete suppression (> 50 dB extinction) which is useful for completely blocking wavelengths outside the region of interest. It can also be seen that by redirecting the light in the y-dimension instead of the x, the output can be coupled to different output fibres giving switching functionality. We utilize all these features of the WaveShaper to obtain the pulse carving we demonstrate in the following section.

6.3.2 Pulse Shaping

To improve the quality of our TOFTs, we wanted to use the OFCG as a source from which to shape new parabolic pulses. The parabolic pulses would ideally be 25 ps at the base (bit slot duration of 40 Gb/s data), chirp free and of course exhibit a good parabolic shape. Furthermore, we wanted to obtain a *dark* parabolic shape instead of the bright parabolics we have previously used in Chapters 4 and 5. This was because dark parabolics suffer from less SPM than bright parabolics which was important for our experiment [10]. Further discussion on our choice of dark parabolics is given in the following chapter. The first parabolic design attempted is shown in Fig. 6.16 in blue. A dark parabolic was chosen with edges that decayed parabolically, thus representing the neighbouring bit slots, as shown in Fig. 6.16(a). In Fig. 6.16(b) we show the required spectrum to achieve this. Note that some of the features of the spectrum are quite fine and that it decays steeply. This posed a problem with the 0.2 nm resolution and 34 dB maximum attenuation of the WaveShaper. Although contradictory to most pulse shaping designs, the solution to this was to increase the pulse bandwidth by creating a sharper drop from the upper edge of the dark parabolic to zero. As well as widening the spectral features, this served to bring more of the spectral lobes above the -34 dB attenuation limit, thus giving a better parabolic shape. The resulting design is shown in Fig. 6.16 in red. However, it is not possible to simply apply the design in Fig. 6.16(b) to the WaveShaper as there are other design considerations we have not yet taken into

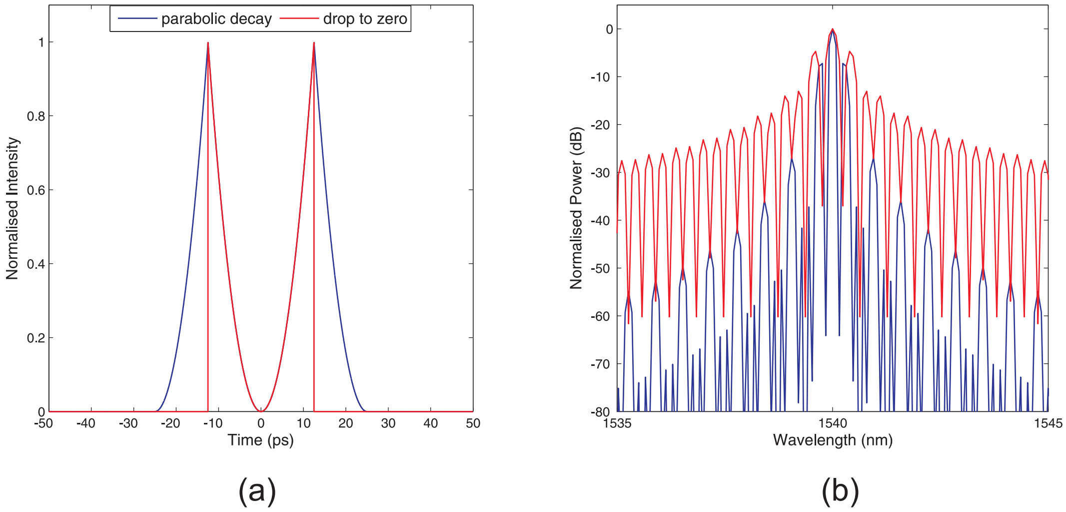

Figure 6.16: Dark parabolic pulse designs with parabolic and abrupt truncated sides. (a) Temporal (b) Spectral

account. The greatest of these is the spectral extent of the pulse. It can be seen from Fig. 6.16(b) that the desired spectrum exhibits infinite side lobes. Because of the attenuation limit of the WaveShaper, we must limit the number of side lobes to those that we can define well in the filter. We decided to include in the spectrum five lobes on each side on the central lobe. However, simply truncating the rest of the lobes will result in distortions in the parabola as shown in Fig. 6.17. This can be mitigated to some degree by also apodizing the remaining lobes. Figure 6.17(b) shows that the apodized parabolic matches fairly well with the non-truncated one. However on close observation it can be seen that the spectrally limited dark parabolic offers a slightly narrower parabolic window and slightly deviates from the perfect parabolic shape in the centre of the pulse. The effects of these imperfections are evaluated in Section 7.2.2.

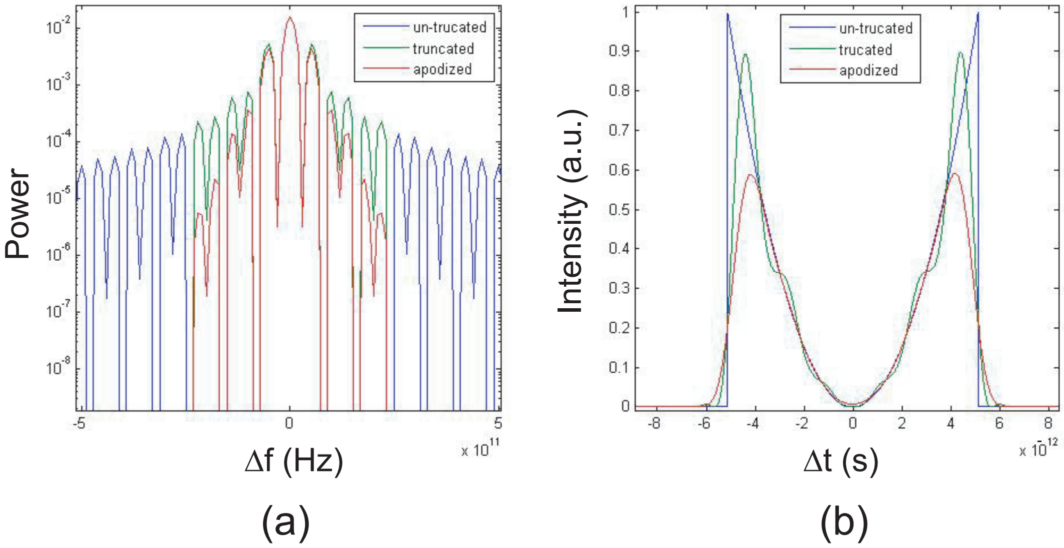

Figure 6.17: The (a) spectral and (b) temporal effects of truncating the parabolic pulse spectrum. Spectral apodization is shown to smooth out the temporal ripples from the truncation.

To help us achieve this filter design we used an external 0.65 nm filter to enhance the reach of the WaveShaper attenuation. Fig. 6.18 shows the application of the external filter (blue line) to the OFC and how the spectrum of the dark parabolic (red line) would fit inside it. The steep sides of the filter shape indicate the edges of the "on" channels used. Note in particular that the lower lobes of the pump spectrum lie >34 dB below the original comb, but only $\sim$ 15 dB below the externally filtered shape showing the extended shaping ability that the external filter offered us. Lastly, we wanted to fully characterise the externally filtered portion in power and phase in order to accurately

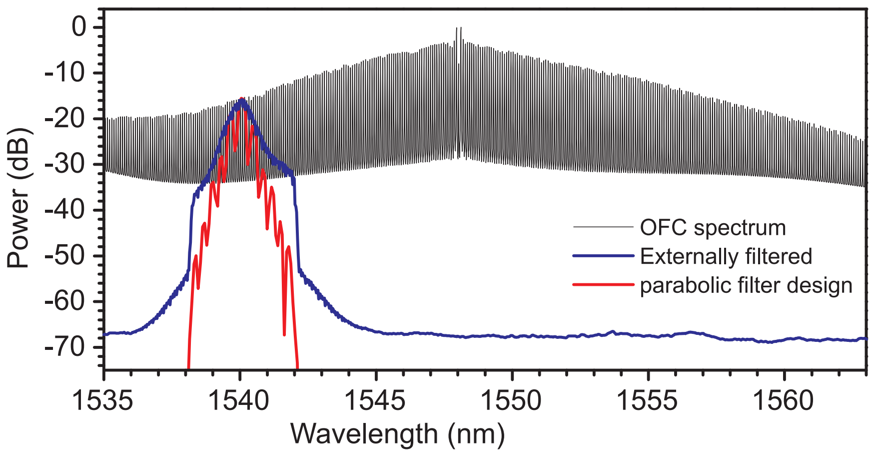

FIGURE 6.18: The OFC spectrum before filtering (black) and after the pump port is passed through the external filter (blue). The parabolic spectrum design is shown in red.

determine the base our parabolic pulses would be carved from including any phase effects in the filtering system. Fig. 6.19 shows the attenuation and phase of the filter used to shape the parabolic pulses. Although the desired phase profile for the dark parabolic pulse requires adjacent lobes to be exactly π out of phase, the configured phase profile can be seen to have some finer features and curving. This extra phase shift was required to compensate for residual phase on the filtering system corresponding to the spectrum shown in Fig. 6.18(blue). The adjustment was small but necessary to ensure a good resulting parabolic.

Note that we have so far wasted the other half of our OFC. The multiple output ports available on the WaveShaper meant that we were able to use the other half of the spectrum to generate a signal pulse thus obtaining both signal and pump from the same source. This arrangement equipped us with a second short pulse source at 10 Gb/s which is automatically synchronised to the first source and which would otherwise be unavailable to us. That is, we were able to direct the channels used for the pump spectrum out of one port on the WaveShaper, and another set of channels shaped for use as the signal out of a separate port. This also had the benefit of giving two highly configurable signals with minimal drift between them, thus increasing the stability of the experiment. The Gaussian shaping applied to the second half of the OFC spectrum to generate the signal can also be seen in Fig. 6.19. The small pedestals that can be observed on the signal and pump filter profiles indicate the attenuation discrepancy between the 34 dB configurable attenuation and the full suppression at the edge of the channels. The resulting parabolic and Gaussian pulses are shown in Figs. 6.20 and 6.21 respectively. The parabolic region matches well to the shown ideal parabolic. It can also be seen to be 20 ps wide, significantly wider than we were able to achieve by the other methods. The signal pulse is shown compared to an ideal Gaussian. The Gaussian pulse is nearly transform limited as shown by the nearly zero chirp of the measured profile and has a pulse width of 2.4 ps.

Lastly, the flexibility of the setup allowed us to generate more interesting shapes with which to test our TOFT device. For example, we were able to use a slope compensation profile to generate a 1.6 ps sinc pulse with a square spectrum. The characterisation of the sinc pulse is shown in Fig. 6.22. The double pulse carving configuration and the pulses shown will all be used in the next chapter. There they will be applied to a new TOFT experiment.

6.4 Conclusions

We have theoretically and experimentally investigated the intensity and phase characteristics of pulses generated in a commercial OFCG. The OFCG generates a pair of oppositely chirped pulses per period, each associated with one half of the spectrum. The large tunability and wide bandwidth of the OFC are exploited in the latter parts of the chapter where it is coupled with tuneable filters to create a tuneable pulse source. The wavelength and bandwidth tuneable filter used in Section 6.2 is shown to be suitable for converting the OFCG into a tunable short pulse source offering high quality pulses with pulse widths tunable from 1.6 to 10.5 ps. However, side lobes on the pulses were observed due to the steep edges of the filter. Improved filter designs compensating for the slope of the OFC spectrum and with apodized edges could yield even more improved pulse characteristics. To achieve this, Section 6.3 used a more configurable filter to obtain precise pulse shaping. The multiport filter enabled two separate shaped pulses to be simultaneously created from the OFCG. These pulses were optimised for use in a TOFT setup and will be the pump and signal used in our next experiment in the following chapter.

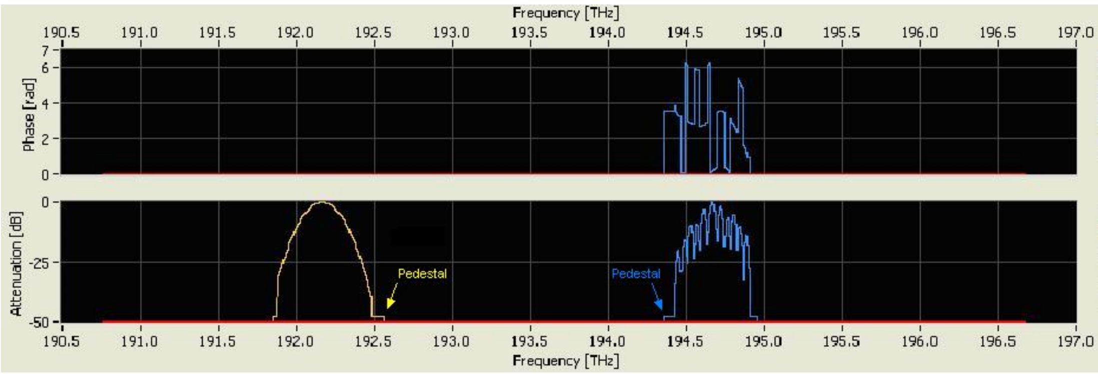

FIGURE 6.19: Attenuation and phase profiles configured on the WaveShaper. The different colours of the pump and signal indicate that they are set to exit from separate ports.

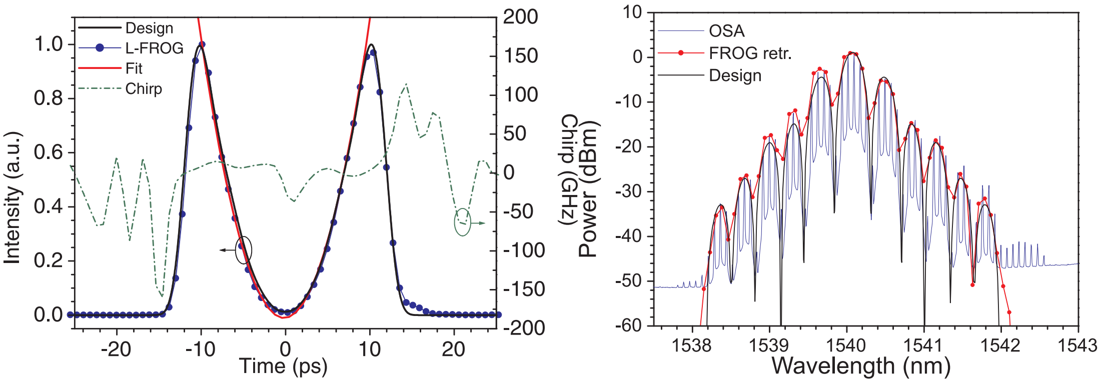

(a) (b)

FIGURE 6.20: (a) Temporal and (b) Spectral profiles of the dark parabolic pulses characterised with the L-FROG and compared to the design.

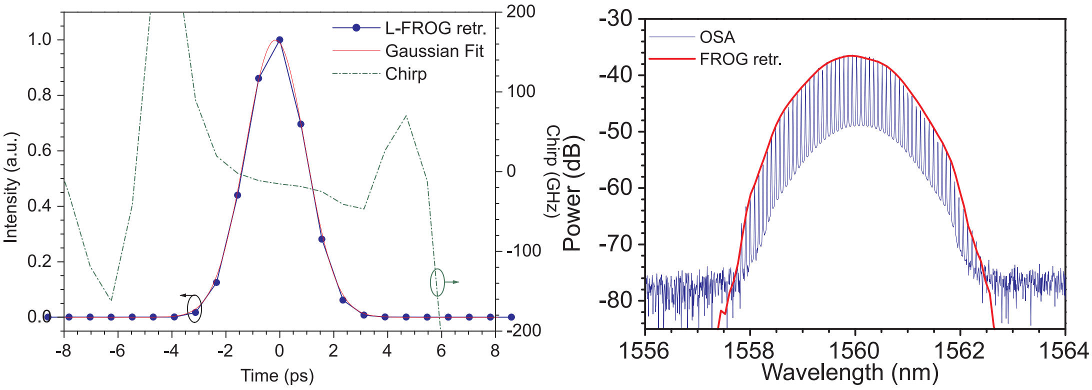

(a) (b)

FIGURE 6.21: (a) Temporal and (b) Spectral profiles of the Gaussian signal pulses characterised with the L-FROG and compared to the design.

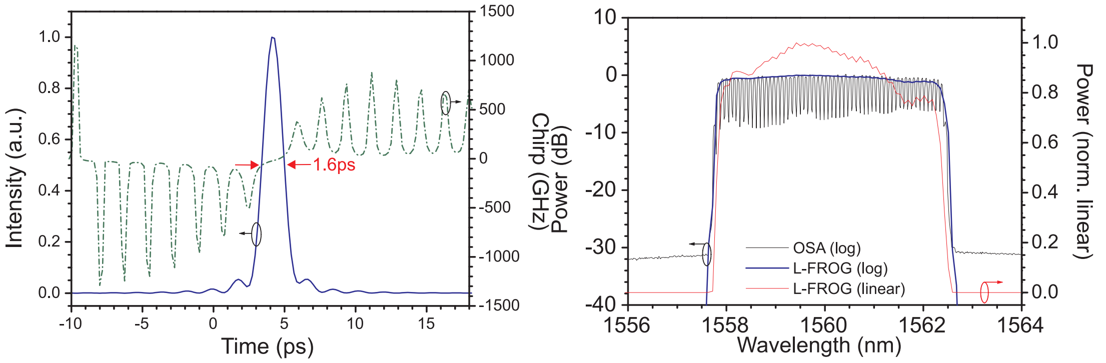

(a) (b)

FIGURE 6.22: (a) Temporal and (b) Spectral profiles of the square spectrum pulses generated by compensating for the OFCG spectral slope and characterised with the L-FROG.

Bibliography

[1] N. C. Wong. Optical frequency counting from the UV to the near IR. *Optics Letters*, 17(16):1155–1157, 1992.

[2] T. Bajraszewski, M. Wojtkowski, M. Szkulmowski, A. Szkulmowska, R. Huber, and A. Kowalczyk. Improved spectral optical coherence tomography using optical frequency comb. *Optics Express*, 16(6):4163–4176, 2008.

[3] G. M. Macfarlane, A. S. Bell, E. Riis, and A. I. Ferguson. Optical comb generator as an efficient short-pulse source. *Optics Letters*, 21(7):534–536, 1996.

[4] E. I. Gordon and J. D. Rigden. The Fabry-Perot Electro-Optic Modulator. *Bell System Technical Journal*, 42:155–72, 1963.

[5] T. Kobayashi, T. Sueta, Y. Cho, and Y. Matsuo. High-repetition-rate optical pulse generator using a Fabry-Perot electro-optic modulator. *Applied Physics Letters*, 21 (8):341–343, 1972.

[6] M. Kourogi, K. Nakagawa, and M. Ohtsu. Wide-span optical frequency comb generator for accurate optical frequency difference measurement. *IEEE Journal of Quantum Electronics*, 29(10):2693–2701, 1993.

[7] Z. Jiang, D. E. Leaird, C. B. Huang, H. X. Miao, M. Kourogi, K. Imai, and A. M. Weiner. Spectral line-by-line pulse shaping on an optical frequency comb generator. *IEEE Journal of Quantum Electronics*, 43(11-12):1163–1174, 2007.

[8] SANTEC. Programmable Optical Tunable Filter OTF-920. *http://www.santec.com/jp/wp-content/uploads/OTF-950-C-E-v150901.pdf.*

[9] M. A. F. Roelens, S. Frisken, J. A. Bolger, D. Abakoumov, G. Baxter, S. Poole, and B. J. Eggleton. Dispersion trimming in a reconfigurable wavelength selective switch. *Journal Of Lightwave Technology*, 26(1):73–78, 2008.

[10] M. Nakazawa. New frontiers in optical communication: Ultrahigh-speed transmission and coherent transmission. In *3rd International Symposium on Ultrafast Photonic Technologies*, pages 3–6, Cambridge, USA, 2007.

Chapter 7

Complete TOFTs using Dark Parabolic Pulses

> "A TOFT causes the temporal and spectral envelopes of a signal to swap such that its spectral profile is transferred to the temporal domain and vice versa."

At the beginning of this thesis, we set out to perform temporal optical Fourier transforms which was defined as quoted above. To achieve this goal, we have so far analytically derived the occurrence of TOFT behaviour through time lensing (Chapter 2) and its experimental implementation using parabolic pulses generated in two different ways (Chapters 4 and 5). We can even say that we have obtained TOFTs in Chapters 4 and 5, having demonstrated the transfer of a signal's spectral profile into the time domain for signal regeneration. However, something is missing. In these experiments, we observed spectra that were not as we expected and do not comply with the TOFT we originally defined. That is, we have so far not observed the correct transformation of a signal's temporal profile into the spectral domain.

In this chapter we work to resolve this discrepancy and demonstrate a TOFT complete in both the time and frequency domains. We do this by revisiting the TOFT theory derived in Chapter 2 and extend it to considering the signal's input phase separately. The phase dynamics surrounding TOFT behaviour is further investigated through the use of dispersion maps. These maps plot the effect of perturbations on the TOFT system and the balance between the chirp induced by the time lenses and the dispersion surrounding it. In the experimental portion of this chapter we redesign our TOFT experiment using the new dark parabolic time lenses we generated in Chapter 6. With these time lenses we were able to verify the new theory and use it to perform a new improved and complete TOFT.

7.1 Theory Revisited

From Section 2.4 we considered the passage of an arbitrary pulse $A_{in}(T)$, in a time frame shifted by $T = t - \beta_2 z$, through a time lens function defined as

$$H(T) = \exp\left[i\frac{\omega_0 T^2}{2f_T}\right] = \exp\left[-i\left(\frac{K}{2}\right)T^2\right]$$

where ω_0 is the central frequency, f_T is the focal time and $K = -\frac{\omega_0}{f_T}$ is the chirp rate. To explicitly consider the chirp of the input pulse, we can redefine the input pulse to have both arbitrary intensity and phase as $A_{in}(T)\exp[i\phi_s(T)]$. As before, the target pulse is propagated through the time lens $H(T)$ and viewed after some dispersion

$$G(\omega) = \exp\left[i\frac{\xi}{2}\omega^2\right]$$

where $\xi = \beta_2 z$ is the dispersion. The output pulse after propagation can then be described by applying the $H(T)$ and $G(\omega)$ operators to give

$$A_{out}(\omega) = F\{F^{-1}\{A_{in}(\omega)\exp[i\phi_s(\omega)]\}H(T)\}.G(\omega)$$

which using the convolution theorem [1] reduces to

$$A_{out}(\omega) = \frac{1}{2\pi}\left[(A_{in}(\omega)\exp[i\phi_s(\omega)]) * H(\omega)).G(\omega)\right]$$

where $H(\omega)$ is the Fourier transform of $H(T)$ given by

$$H(\omega) = \frac{1}{\sqrt{iK}}\exp\left[\frac{i\omega^2}{2K}\right]$$

we can now express the output spectrum as

$$\begin{aligned} A_{out}(\omega) &= \frac{1}{2\pi\sqrt{iK}}\exp\left[\frac{i}{2}\left(\xi + \frac{1}{K}\right)\omega^2\right] \\ &\quad \times \int A_{in}(w')\exp\left[i\left(\phi_s(\omega') + \frac{\omega'^2}{2K}\right)\right]\exp\left[i\left(\frac{\omega}{K}\right)\omega'\right]d\omega' \end{aligned} \tag{7.1}$$

It can be seen that for the conversion $T = \omega/K$ the integral above resembles a Fourier transform of a pulse with input spectral phase, $\phi_s(\omega') + \omega'^2/2K$, which is inconsistent with the actual input phase $\phi_s(\omega)$. Therefore the input pulse into the time lens requires an extra phase shift, $\Delta\phi$, such that the total phase is $\Delta\phi + \phi_s(\omega') + \omega'^2/2K = \phi_s(\omega')$. That is, we require

$$\Delta\phi = -\omega'^2/2K. \tag{7.2}$$

to obtain a Fourier transform in the spectral domain. Correspondingly the phase term outside the integral, will cancel out to ensure there is no residual phase if

$$\xi + 1/K = 0. \tag{7.3}$$

Note that this is the same relation obtained in Eqn 2.20 and is required to preserve the transformation in the time domain. Combining equations 7.2 and 7.3 we see that to obtain a complete Fourier transform in both domains and for the input phase to be preserved in the transformation we also require

$$\Delta\phi = -\frac{\omega'^2}{2K} = \frac{\xi}{2}\omega'^2. \tag{7.4}$$

That is, the extra phase shift $\Delta\phi$ can also be implemented by the chromatic dispersion operator $H(\omega) = \exp\left[i\frac{\xi}{2}\omega^2\right]$. This would add a pre-dispersion before the time lens equal to the post-dispersion and produce the output spectrum

$$A_{out}(\omega) = \frac{1}{2\pi\sqrt{iK}} \int A_{in}(\omega')\exp\left[i\phi_s(\omega')\right] \exp\left[i\left(\frac{\omega}{K}\right)\omega'\right] d\omega' \tag{7.5}$$

which gives a true scaled Fourier transform of the input spectrum $A_{in}(\omega)\exp\left[i\phi_S(\omega)\right]$.

The analysis above has shown that a true OFT can only be obtained when the dispersion surrounding the time lens satisfies equation 7.4. However, to further understand the relationship between the chirp rate of the time lens and dispersion, we must also consider perturbations to this matching condition. Figure 7.1 explores the dispersion space in the region around the $\xi_0 = -1/K$ matching condition. The dispersion map plots the output temporal pulse width of a Gaussian signal pulse as a function of the pre- and post-dispersions ξ_1 and ξ_2 respectively. In an experiment, these can simply be implemented by suitable lengths of fibre preceding and following the time lens. Note that the chirp rate, $K = 1/t_0^2$, is chosen to obtain a unity transform of a 2.55 ps (FWHM) transform limited input pulse. Also, ξ_1 and ξ_2 are normalized using

$$\xi_1 = \frac{\beta_2 z_1}{\xi_0} \qquad\qquad \xi_2 = \frac{\beta_2 z_2}{\xi_0}$$

where β_2 is assumed to be the same for both fibres, and z_1 and z_2 are the lengths of fibre preceding and following the time lens respectively. Figure 7.1(b) shows the dispersion map with contours of the output spectral width. There are several features of the dispersion-chirp rate relationship that these two dispersion maps highlight. For instance, if we consider the line $\xi_2 = 1$ on Fig. 7.1(a) we see that the temporal width remains constant. This is the behaviour expected from a frequency-to-time transformation as we have seen in the previous chapters. Since ξ_1 does not change the input spectrum of the signal, the temporal output after the OFT must be constant. The preservation of the temporal pulse width along this line regardless of the input dispersion confirms its suitability for dispersion compensation in agreement with the theory in Section 2.4. The same line $\xi_2 = 1$ in Fig. 7.1(b) shows a different spectral behaviour. Instead of remaining constant, the spectral width increases away from the $\xi_1 = 1$ point. If $\xi_2 = 1$ was the only condition required to obtain a complete TOFT, the spectral width of the output signal would be expected to broaden as ξ_1 increases because an increase in ξ_1 is equivalent to an input pulse which has already suffered GVD and is thus temporally broadened. After a true TOFT, this temporal broadening should be transformed through the TOFT as a spectral broadening of the output. Instead, we see that the minimum of the spectral width is offset to $\xi_1 = 1$ supporting the theory that a pre-dispersion equivalent to $\xi_1 = 1$ would compensate for the offset. In this case, GVD already suffered by the input pulse would become a perturbation *away* from $\xi = 1$ and result in the consistent spectral broadening expected. Due to the symmetry of Fourier transform behaviour, we notice that the converse occurs along the line $\xi_1 = 1$. Along this line the spectral width remains unaffected by ξ_2, but the temporal width reaches a minimum at $\xi_2 = 1$ where all internal phase terms are cancelled out.

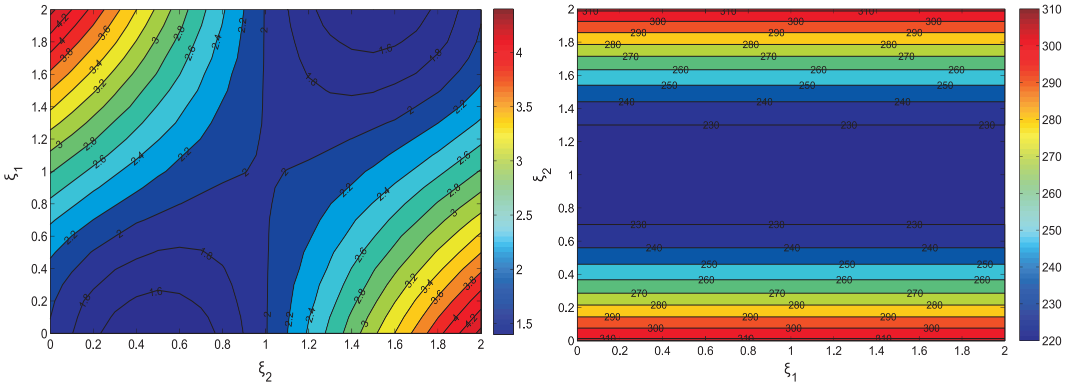

FIGURE 7.1: Dispersion maps of the (a) temporal widths in ps and (b) 3-dB spectral widths in GHz of the output, as a function of perturbations in ξ_1 and ξ_2 around the ideal TOFT condition. The simulated input pulses were transform limited and had an input width of 2 ps.

7.2 Practical Limitations

The theory has shown that a TOFT can be obtained using a quadratic phase shift as a time lens, and that the time lens needs to be preceded and followed with dispersions equal to $\xi = 1/K$ to be complete. This section explores numerically and without the complications of experiment, the limitations of using XPM with a parabolic pulse as the method of imposing the required quadratic phase shift.

7.2.1 Dispersion Map Analysis

Fig. 7.1 showed how the dispersion map should look for an ideal time lens. That is, when a perfect quadratic phase shift is imparted to the entirety of the test signal. In practice, obtaining a quadratic phase shift through XPM between the pump and signal pulses simultaneously subjects the pulses to other linear and nonlinear effects in the medium such as SPM and dispersion, which will also affect the signal's phase. We can seek to minimise dispersion by an appropriate choice of fibre and operating wavelength, but since SPM uses the same χ^3 nonlinearity as XPM, limiting this mechanism would not serve our cause. Even if the pump pulse evolution due to these effects is quite small, the most significant consequence of SPM is spectral broadening of the pump which can lead to spectral overlap with the signal. When this occurs, the signal and pump cannot be fully extracted from each other after XPM and a residual portion of the pump is filtered along with the signal. This residual portion lends an additional phase to the signal which would not be compensated for in the TOFT. Fig. 7.2(a) shows the dispersion map generated by using a split-step Fourier routine to simulate the XPM between a 2.55 ps Gaussian signal and 25 ps bright parabolic pulses. It is clear that the line of constant pulse width in this map is offset from $\xi_2 = 1$ and that it is slightly skewed. Observation of the spectrum after XPM (shown beside the map) reveals the cause of the offset. The large amount of SPM induced spectral broadening suffered by the strong pump has caused its spectrum to overlap with the signal's. This is confirmed in Fig. 7.2(b) where the wavelength separation has been increased to 100 nm and as a consequence, the offset is seen to return to $\xi_2 = 1$. Note that we wanted to ensure the signal and pump pulses were experiencing the same dispersion and SPM when separated by 100 nm as they were when they were separated by 20 nm. The dispersion slope of the fibre was therefore reduced to one fifth of its normal value in the simulation where they are 100 nm apart. Being

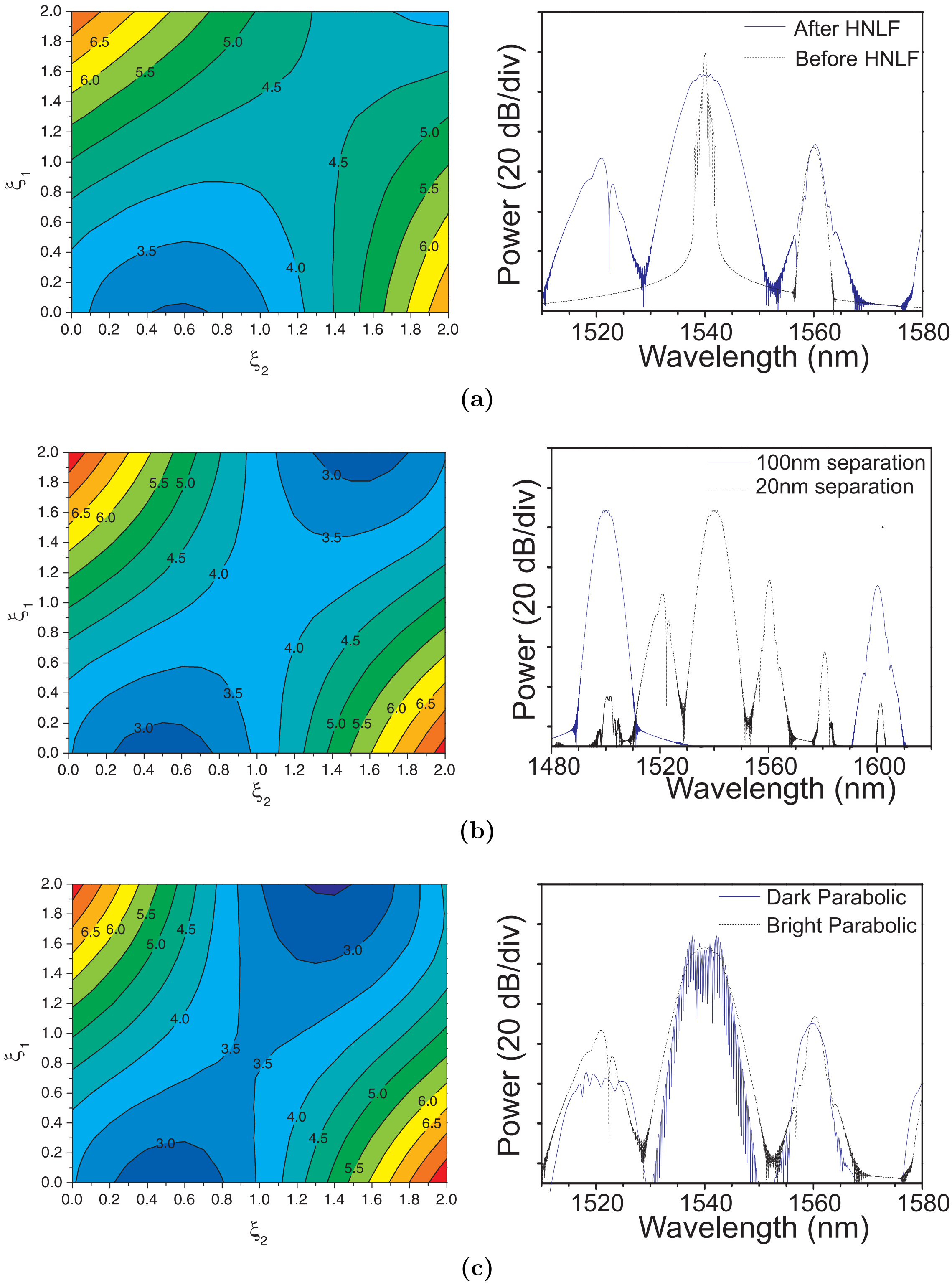

FIGURE 7.2: Dispersion maps and spectra simulating XPM between the signal and (a) a bright parabolic pump with 20 nm separation, (b) a bright parabolic pump with 100 nm separation and (c) a dark parabolic pulse with 20 nm separation.

unable to increase the wavelength separation to this extent in practice, we need to find a way to reduce the SPM instead. Although detrimental to the XPM process, the simplest way to reduce SPM is to reduce the pump power. There are thus several trade-offs that must be considered in designing the TOFT. The spectral broadening due to SPM can be reduced by reducing the peak power of the pump which in turn can only be achieved by reducing the time lensing window or decreasing K. Decreasing K may be a suitable sacrifice if the application does not require the output pulse to be scaled to a particular width. Even so, there is a catch since both options increase the risk of the signal being broader than and 'leaking' beyond the extent of the time lensing window. It is obvious that there will be more leakage if the time lensing window is reduced, however it may be less obvious that by decreasing K we must necessarily increase ξ_0, thus increasing leakage through the need for a larger pre-dispersion.

These compromises can be alleviated to some degree by using a dark parabolic pulse instead of a bright one [2]. Fig. 7.2(c) shows the dispersion map and related spectral broadening using a 25 ps dark parabolic pulse. It can be seen that the dark parabolic pulse has undergone less SPM than the bright one, thus reducing the spectral overlap between the pump and the signal. This in turn reduces the offset in the dispersion map of Fig. 7.2(c) and indicating the dark parabolic pulses would be a better choice of pump for our XPM-based TOFT.

7.2.2 Pulse Profile Analysis

We are interested to find if spectral broadening is the only side effect of using XPM with parabolic pulses as a means to implement a time lens. To analyse this and to clearly show the quality our simulated TOFT processes, we chose a square spectrum (10^{th} order super-Gaussian) to transform, as it would be particularly sensitive to imperfect transforms lacking in definition. We begin by following the theory conditions exactly and impose the time lens onto the signal with a perfect and infinite quadratic phase shift eliminating any interference from nonlinear effects. If we do this, a perfect transform is obtained as predicted (Fig. 7.3). However temporal phase shifts cannot stretch to infinity and at the very least are limited to the period of the signal in question. If the signal in question has a very low duty cycle then this is not a problem and the phase shift is more likely to be limited in magnitude. When using XPM, this is limited by the peak power of the parabolic pump pulse. Since K determines the scaling of the

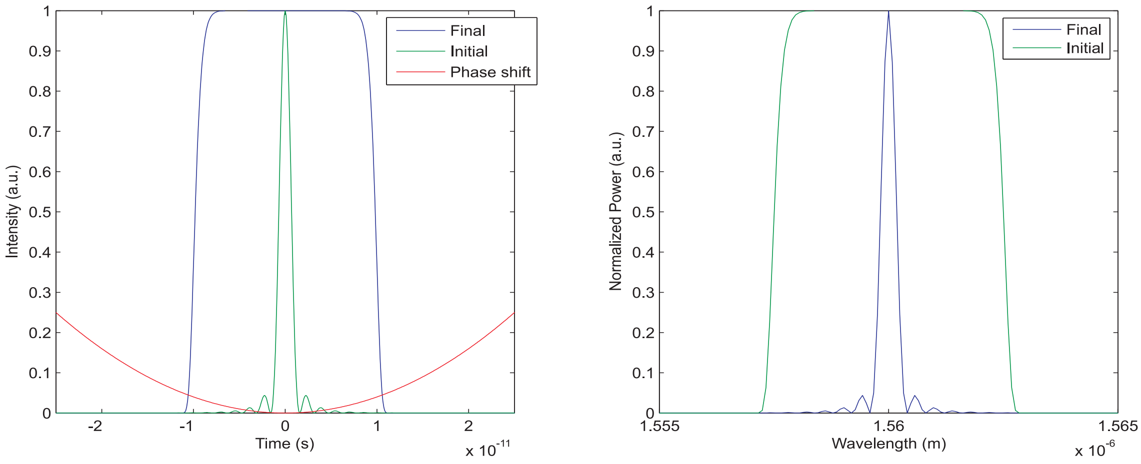

FIGURE 7.3: In the ideal case, a quadratic phase shift is applied across the whole signal resulting in a perfect transform.

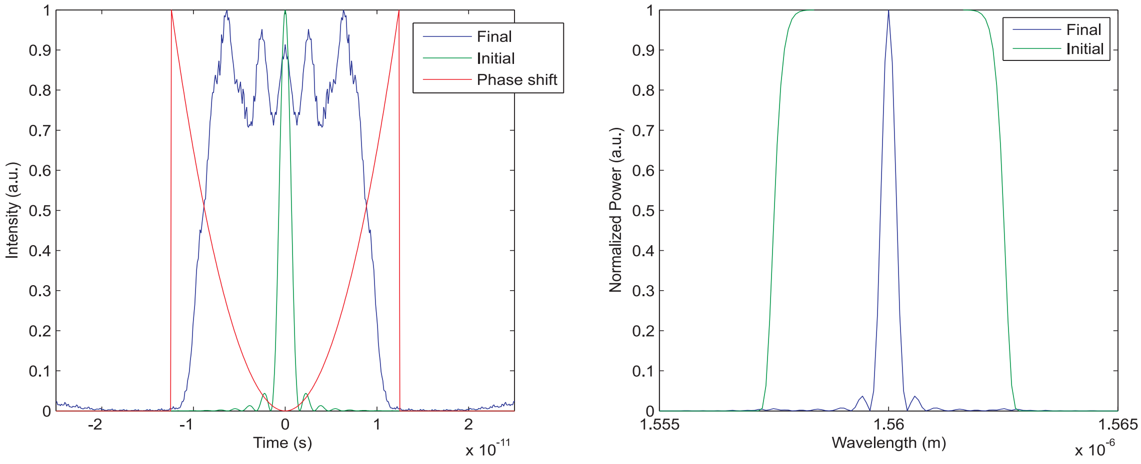

FIGURE 7.4: Truncation of the parabolic reduces the transform window. This in turn leads to ripples along the top edge of the transformed square.

transformed waveforms, this value frequently cannot be chosen and an increase in K will result in a reduction in the transform window for any system with a maximum applicable phase shift. This gives rise to the first and probably the most important limitation of TOFTs. The issue of leakage was previously mentioned in Chapter 4 and its effect can be seen in Fig. 7.4 where the quadratic phase shift has been temporally truncated and the transform window is now limited. Note that our choice of an abrupt truncation rather than a slow decay was discussed in Section 6.3.2. We can see the top edge of the output pulse in Fig. 7.4 now exhibits ripples instead of being flat as it should if the square shape was correctly transferred from the spectral domain. These ripples come from the effective truncation of the sinc pulse's infinite side lobes at the edge of the parabolic phase. The risk of leakage is even greater now with the use of a pre-dispersion.

In most cases the pre-dispersion will broaden the signal pulse, pushing more of the pulse outside the parabolic window where it does not experience the quadratic phase shift. In fact, this is demonstrated even more clearly if we choose a signal pulse that is initially very well contained in the parabolic window as is the case if we flip the current example around. That is, we can choose for the signal pulse to be square (super-Gaussian) with the many lobed sinc shape residing in the spectrum. Fig. 7.5 shows the input and output profiles of such a pulse when the quadratic phase shift is infinite (coloured) and when it is truncated (black). It is clear that although the 6 ps (FWHM) square is much shorter than the 25 ps parabolic, the square transformed from the time to the spectral domain still has significant ripples along the top edge. These ripples arise not because I have used a high order super-Gaussian instead of a true square, but rather from the pre-dispersion of the square dispersing it into a many lobed pulse extending beyond the the parabolic window. Figure 7.6(a) shows the pre-dispersed square on a log scale as compared to the extent of the parabolic window. Furthermore, we see that if we increase the transform window without increasing the chirp as shown by the green trace, the oscillations of the output pulse after TOFT will be reduced since more of the signal lobes are included within the parabolic window.

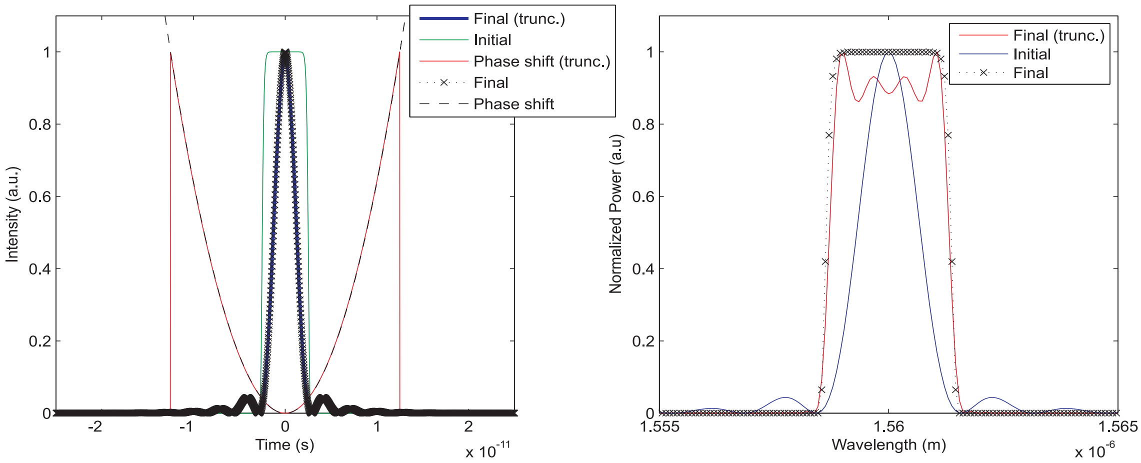

Figure 7.5: The square pulse is completely confined within the parabolic. However, there are still ripples in the transformed profile.

The quality of the TOFT in Fig. 7.5, although not perfect is still very good and the main structure convincing. The next limitation is in the spectral content of the pump. We described in Section 6.3.2 the effect that spectral limitations have on a dark parabolic shape, and the means taken to produce the best possible (and practical) dark parabolic of a useful width. If we use that practically designed dark parabolic now, it can be

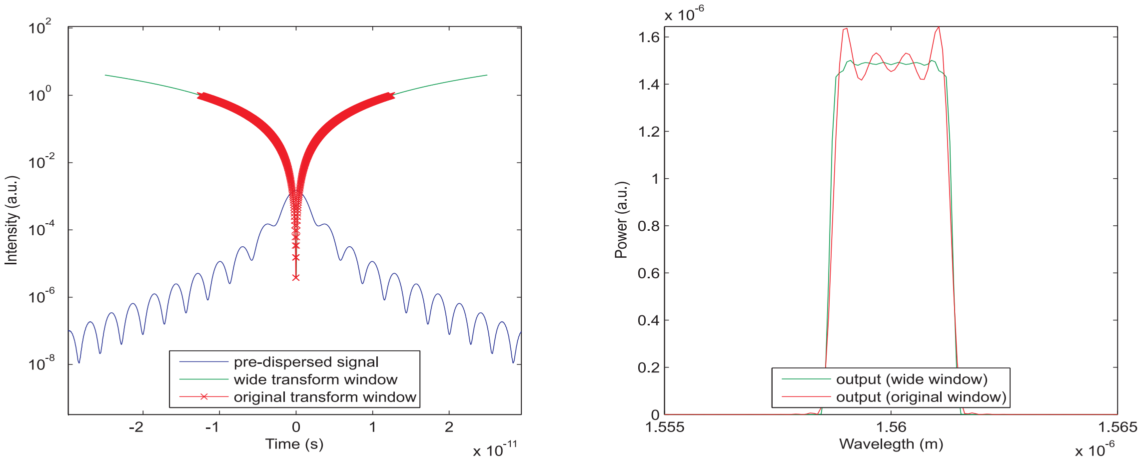

FIGURE 7.6: The pre-dispersion causes the square pulse to leak out of the parabolic window causing the ripples in the transform. A wider window reduces the ripples significantly.

seen that it offers a slightly narrower parabolic window than a non-spectrally limited parabolic, and also that it slightly deviates from the perfect parabolic shape in the centre of the pulse. The effect of the further narrowing is shown in Fig. 7.7, with the distortions along the top edge of the square increasing as we would expect. Of greater effect however is the seemingly small deviation at the centre of the pump profile from an ideal parabolic. Fig. 7.7 shows the quality of the TOFT that can be achieved with a pump imposing a phase shift of this shape. Clearly, there is now a distortion in the middle of the transform. Also shown, in Fig. 7.7(b) is the change in the gradient of the truncated and apodized parabolic. Using the same $\omega = TK$ scaling factor for the pump gradient as is applicable to the signal, the correspondence between where the phase shift changes and the location of the signal distortion is clear. Finally we must consider that the simulations so far have assumed a perfect transfer of the pump profile to a signal phase shift equivalent to $2\gamma P(t)L$. As discussed earlier, other nonlinear effects that accompany the desired XPM, such as SPM, can also be detrimental to the time lensing process. Furthermore, we have seen here that seemingly small disturbances to the time lensing whether they be from leakage or an imperfect parabolic, can cause significant disturbances in the final transform.

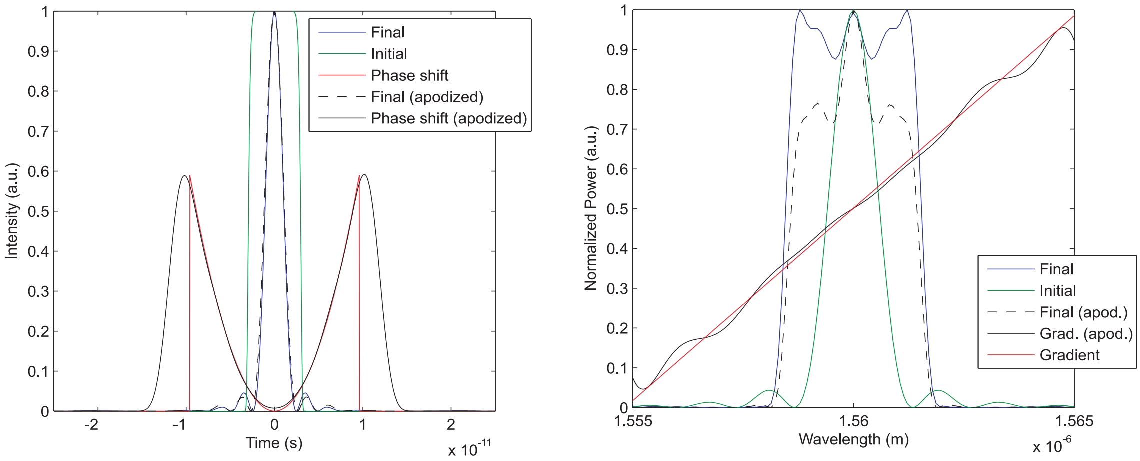

FIGURE 7.7: The realistic, spectrally limited dark parabolic deviates from the ideal in the centre. The change in chirp in the centre of the window gives a corresponding distortion in the centre of the transformed pulse.

7.3 Experimental Verification

7.3.1 Experimental Setup

Now aware of the practical limitations, we sought to experimentally verify the complete TOFT theory with the best possible setup. Compared to the TOFT setups used in previous chapters, we are now using both a pre- and post-dispersion. Other improvements to the TOFT setup have also been made which can be seen in the experimental setup in Fig. 7.8. The most significant change is in the time lens which is now implemented through XPM between the signal and a dark parabolic pump pulse instead of a bright one. The dark parabolic pulses and the target signal were simultaneously generated through spectral shaping of the broadband OFC. Spectral carving of the two stable, synchronized and accurately shaped signal and pump sources was facilitated by the WaveShaper 4000E. The spectrum of the 10 GHz frequency comb was carved at 1540 and 1560 nm, and shaped to form 14 ps dark parabolic pump pulses and 2.4 ps Gaussian signal pulses respectively (see Fig. 7.9). The full description of the design and implementation of the dual pulse carving can be found in Section 6.3.2. As well as requiring only one source instead of two, generating the pump and signal pulses this way had many advantages with regards to this experiment. Firstly, the parabolic generation was simplified allowing greater power, width and shape tunability than the nonlinear methods as well as greater wavelength tunability than using a SSFBG. Furthermore, its simplicity of operation and the reconfigurability of the filter made real time adjustments

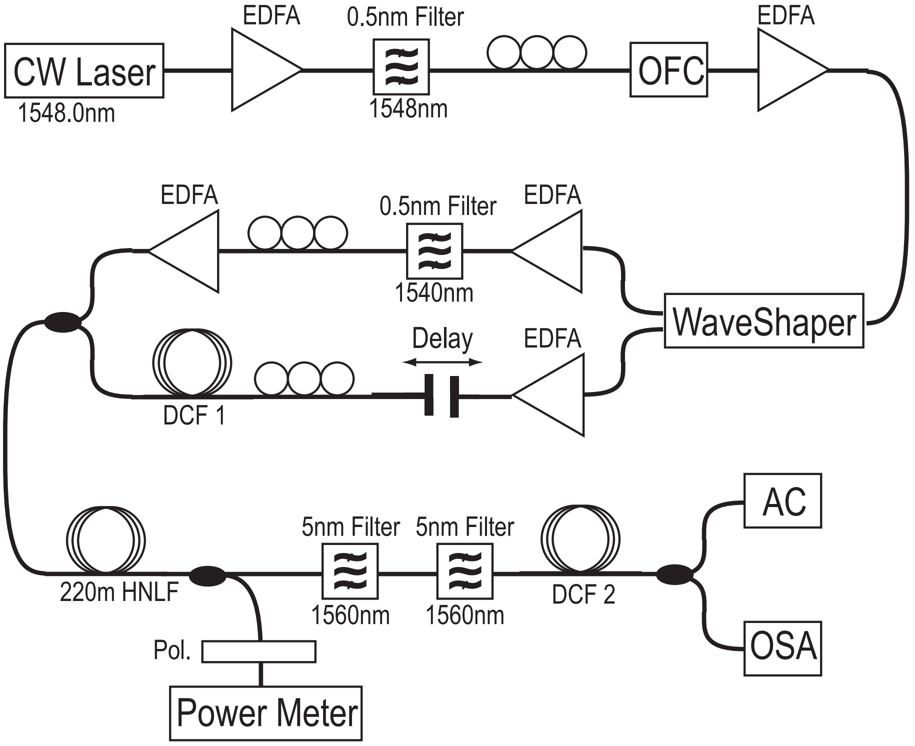

Figure 7.8: Experimental setup to study complete TOFTs.

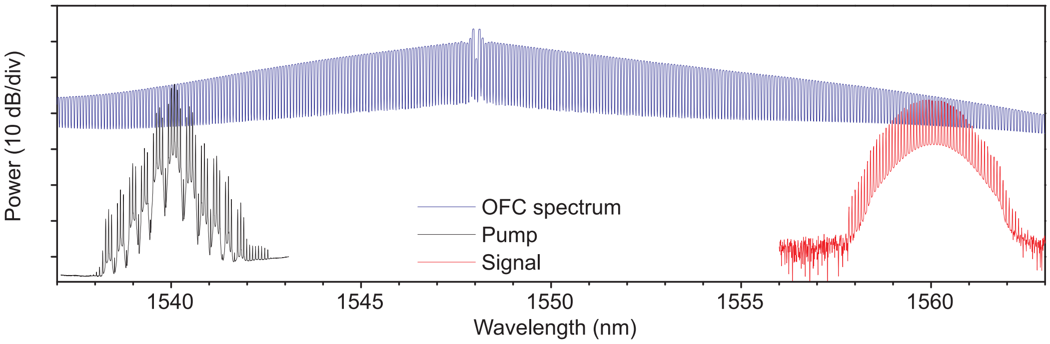

Figure 7.9: The dark parabolic pump and Gaussian signal were both carved out of the same optical frequency comb.

possible for optimized pulse shaping. Although the requirements are less stringent, all these arguments apply to the signal also. Together, the wide wavelength span and wavelength tunability of the OFCG critically allowed us to have two sources at a wide wavelength separation thus reducing spectral overlap. Finally, the use of one source instead of two eliminated the need to synchronise two separate sources, reducing the temporal drift between the pump and signal and thus greatly increasing the stability of the experiment.

After carving, the two portions of the comb were directed out of two separate ports in the WaveShaper. The pump was strongly amplified and further filtered with a 0.65 nm (3-dB width) Gaussian filter to improve its extinction. The width of these pulses were chosen for optimal OFT conditions but would be ultimately limited by the spectral resolution of the configurable filter.

The profile of the dark parabolic pump pulses and the Gaussian signal pulses as measured by the L-FROG were shown previously in Figs. 6.20(a) and Fig. 6.21(a) respectively. They are shown here again in Fig. 7.10, compared to each other and showing the confinement of the signal within the parabolic window. Also shown is the signal pulse after $\beta_2 z = 4.8$ ps^2 of pre-dispersion was added (in simulation). This was the maximum pre-dispersion we applied in this experiment and we can see that although the confinement is generally still quite good, some leakage of the pulse wings is now expected.

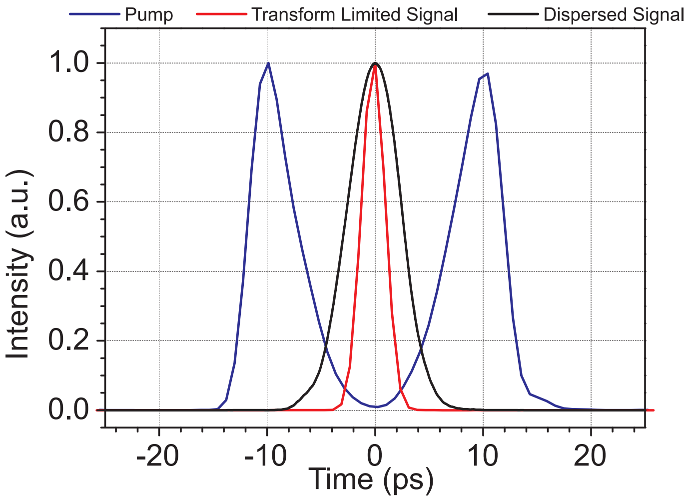

FIGURE 7.10: Profile of the input signal pulse compared to the dark parabolic pump with and without the maximum applied pre-dispersion (4.8 ps^2).

The use of a dark parabolic pulse instead of a bright one means that a negative chirp is imposed on the signal and the dispersive element must be normal or $\xi_0 > 0$. So the target signals were pre-dispersed (ξ_1) in an initial length of DCF before being coupled with the amplified dark parabolic pulses to undergo XPM in a 220 m length of low dispersion, highly nonlinear fibre. The fibre parameters are given in Table 4.1. Following XPM, the pump pulses were filtered out to prevent any further XPM and the signal passed through a second length of DCF (ξ_2). To obtain a unity transform of the 2.4 ps Gaussian signal we can use Eqn. 2.19 to find that we require $\xi_0 = 2.08$ ps^2. The closest dispersive amount we had in the experiments was a 15 m length of DCF with D=-1.8 ps/nm ($\xi_0 = 2.3$ ps^2).

7.3.2 Verification of the TOFT Operational Point

In the same way that we verified the TOFT matching in Chapter 5, we can verify the pump power we need to match this dispersion by measuring the output pulse width for increasing pump power. The TOFT point will be at the pump power where the signal pulses have the same width regardless of their input dispersion (and therefore input temporal width). The measured output pulse widths versus average pump power are shown in Fig. 7.11 for input dispersions of D = 0, -1.8 and -3.6 ps/nm.

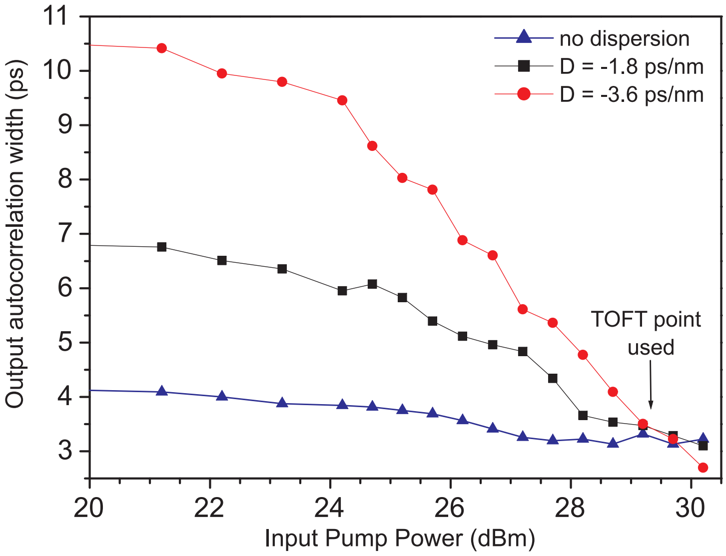

FIGURE 7.11: Plot of output signal pulse width versus average pump power for three input dispersions. The TOFT point can be found at the power where the output pulse widths all match.

We can find the power setting for the operational point for the TOFT at the point where the three lines meet. This can be seen to be at ~ 29.3 dBm. This value however, does not take into consideration any losses or nonlinearities between the amplifier and the HNLF or in the HNLF itself. A better indication of the nonlinearity induced by the pump, is the amount of SPM it has experienced in the HNLF. Fig. 7.12 shows the measured and simulated spectral broadening when the L-FROG retrieved pump pulse is numerically propagated through the HNLF with a peak power of 3.75 W ($P_{ave} = 26.2$ dBm). The match is seen to be very good, with slight differences in the simulated and measured

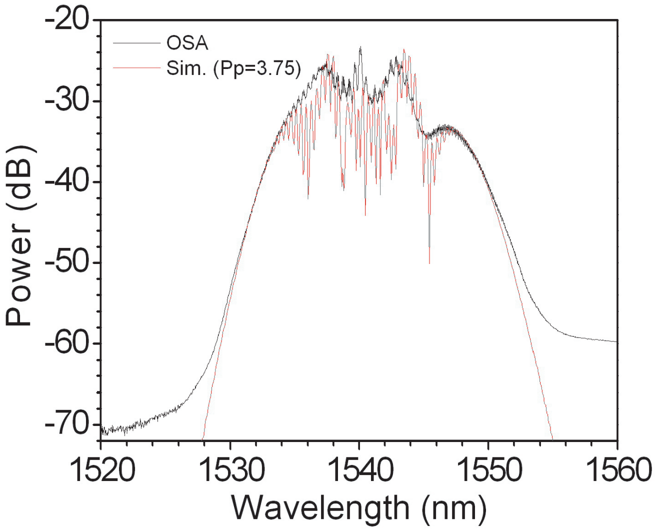

Figure 7.12: Comparison of measured pump SPM compared with simulated SPM using a peak power of 3.75 W.

spectra most likely to be due to the gain spectrum of the amplifier used. This indicates that using this power accurately represents the amount of nonlinearity our pump is experiencing. Note however, that the XPM imposed by the pump on the target signal would also be affected by the exact temporal and polarisation alignment between the pump and the signal in the HNLF, an effect which introduces small uncertainties into the simulation. Fig. 7.13 shows the L-FROG measurements of the pump and signal

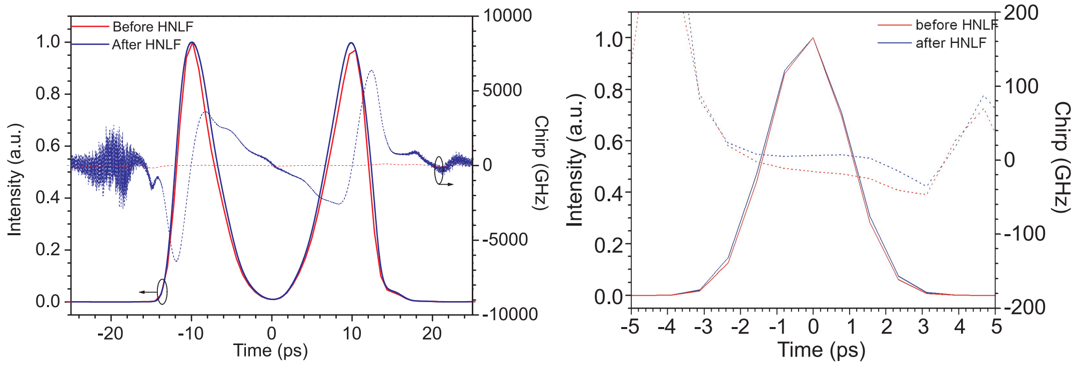

(a) (b)

Figure 7.13: (a) Pump and (b) Signal profiles before and after SPM.

pulses individually after propagation through the HNLF. This gives a measurement of the SPM suffered by the individual pulses. Although the pump pulse was shown to have experienced significant SPM in Fig. 7.12, we can see in Fig. 7.13(a) that the spectral broadening is only temporally evident in the chirp of the pump and has not been very detrimental to the pump's temporal profile. As such, we expect the time lens to still be good throughout the HNLF. Fig. 7.13(b) shows the signal as having experienced very little SPM indeed due to its low input power.

7.3.3 Verification of the Dispersion Map

We have so far established the TOFT operational point for our system. Now we also want to verify the characteristics of the dispersion map around this point. Fig. 7.14 shows the dispersion map simulated by propagating a simulated 2.4 ps Gaussian signal pulse with a peak power of 1.8 mW through the TOFT setup with varying values of pre- and post-dispersion. A chromatic pre-dispersion is applied to the spectrum of the input pulse before it is combined with the pump pulse and propagated through a split-step Fourier routine to simulate the XPM. The pump pulse used in the split-step Fourier routine was obtained from the retrieval of the L-FROG measurement (see Fig. 6.20) and scaled to a peak power of 3.75 W. The signal spectrum is then filtered out with a 5 nm (FWHM) 2^{nd} order super-Gaussian filter centred at 1560 nm to reject the pump pulse as was done in the experiment. The post-dispersion is then applied to the filtered spectrum, and a numerical autocorrelation taken of its temporal profile. The red dots plotted on top of the simulated dispersion map indicate the points on the map that were verified experimentally. Using different lengths of DCF to vary the pre- and post-dispersion, we measured the temporal and spectral profiles of the output pulse along the principle lines on the dispersion map, namely $\xi_1 = 0$, $\xi_1 = 1$, $\xi_2 = 0$ and $\xi_2 = 1$. The measured autocorrelation widths (FWHM) and 3-dB spectral widths are shown next to the corresponding points in ps and nm respectively. A fair match can be seen between the measured and the simulated widths, especially for the lower values of dispersion. Figure 7.15 shows the measured traces along $\xi_1 = 1$ and $\xi_2 = 1$. The measurements show the expected trend on the dispersion map with the temporal pulse widths along the horizontal line $\xi_1 = 1$ reaching a minimum at the point $\xi_1 = \xi_2 = 1$, and remaining fairly constant along the vertical line $\xi_2 = 1$.

The spectral widths are plotted in nanometers as circles on the simulation trace in Fig. 7.16. A full dispersion map was not neccessary in this case since the post-dispersion does not affect the spectral width. Again, we can see that there is a fair match between the simulated and measured values, especially around the complete TOFT operational point, $\xi_1 = 1$. Fig. 7.17 shows the measured output spectral along $\xi_1 = 1$ and $\xi_2 = 1$.

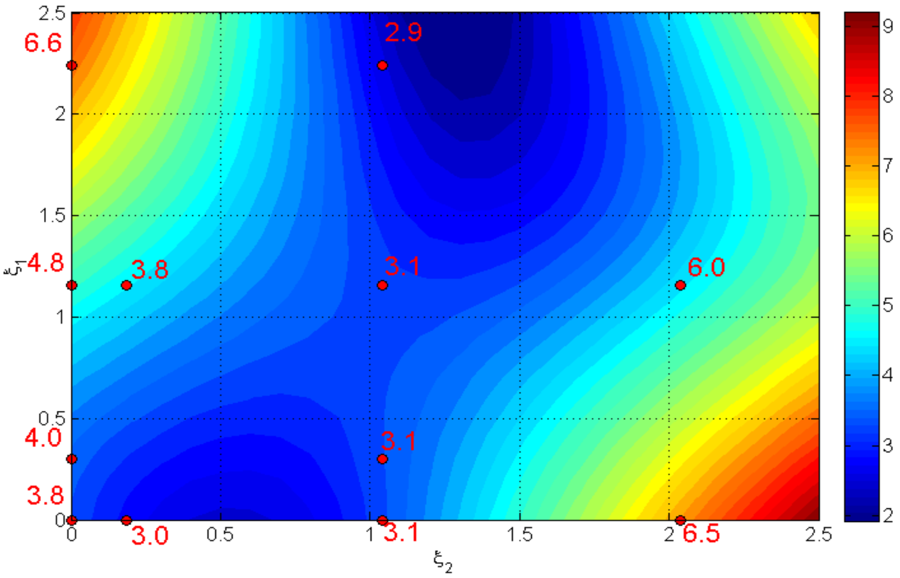

FIGURE 7.14: The simulated dispersion map of autocorrelation values. The red dots and numbers indicate the temporal autocorrelation width of our measurements in ps.

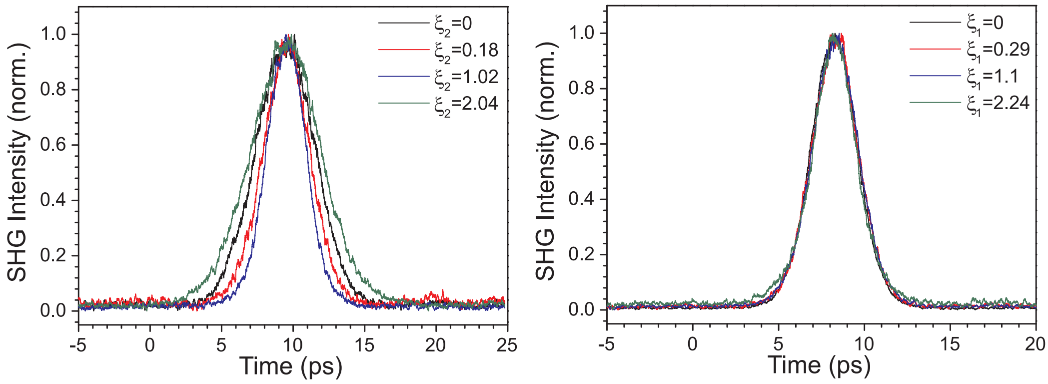

(a) **(b)**

FIGURE 7.15: Autocorrelations of output pulses along the lines (a) $\xi_1 = 1$ and (b) $\xi_2 = 1$.

Note that only the spectral envelopes are shown here to enable easier comparison between them. The spectra can be seen to follow the expected trend, remaining almost constant along the horizontal line $\xi_1 = 1$, and reaching a minimum on the vertical line $\xi_2 = 1$ near the point $\xi_1 = \xi_2 = 1$.

7.3.4 TOFT of a Square Spectrum

We have shown strong evidence that our system was behaving as we expected and would produce a true TOFT at $\xi_1 = \xi_2 = 1$. The final test is to demonstrate a TOFT of an interesting shape and see that the spectral and temporal profiles do indeed swap

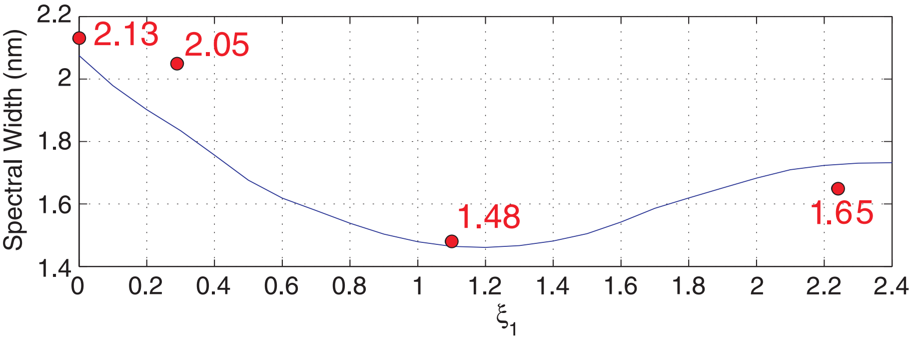

FIGURE 7.16: Spectral width variation.

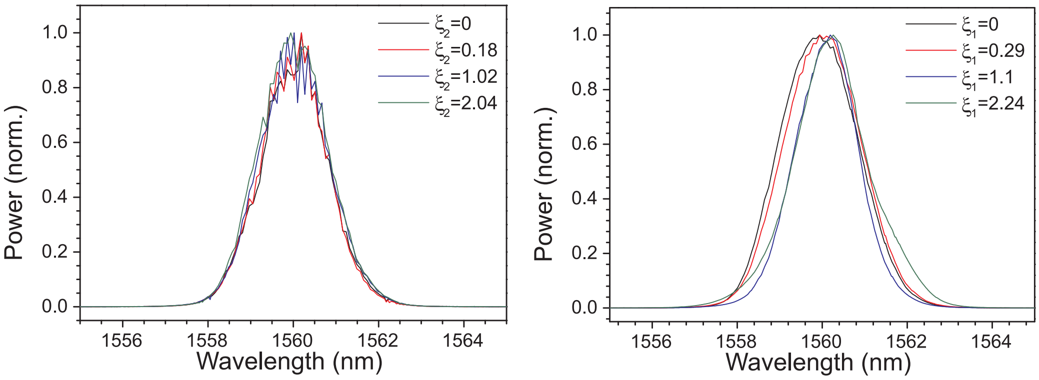

(a) **(b)**

FIGURE 7.17: Spectral envelopes the of output pulses along the lines (a) $\xi_1 = 1$ and (b) $\xi_2 = 1$.

domains as is our aim. The shape we chose to transform is a square spectrum as analysed previously in Section 7.2.2, which has a sinc profile in the time domain. These pulses were produced by adjusting the spectral filter profile such that the slope of the OFCG was compensated at 1560 nm and truncated at 5 nm width to form a square. The characterization of the input signal was previously shown in Fig. 6.22. This shape was chosen for its distinctive shape in the two domains and also the easily identifiable autocorrelation shape of a square pulse which is a triangle. The autocorrelation and spectral traces of the signal pulse before and after the TOFT are shown in Fig. 7.18 below. The solid lines show the actual measurement and the dashed lines are the pulses from the simulation. In the 'before' case, the dashed lines are obtained from the L-FROG retrieval which was used as the input signal pulse in the simulation. We see first that the L-FROG measurement of the input matches those of the autocorrelator and the OSA quite well with the variation on the top edge of the square spectrum being only ~ 0.5 dB. However the matching of the pulses after the TOFT shows some discrepancies,

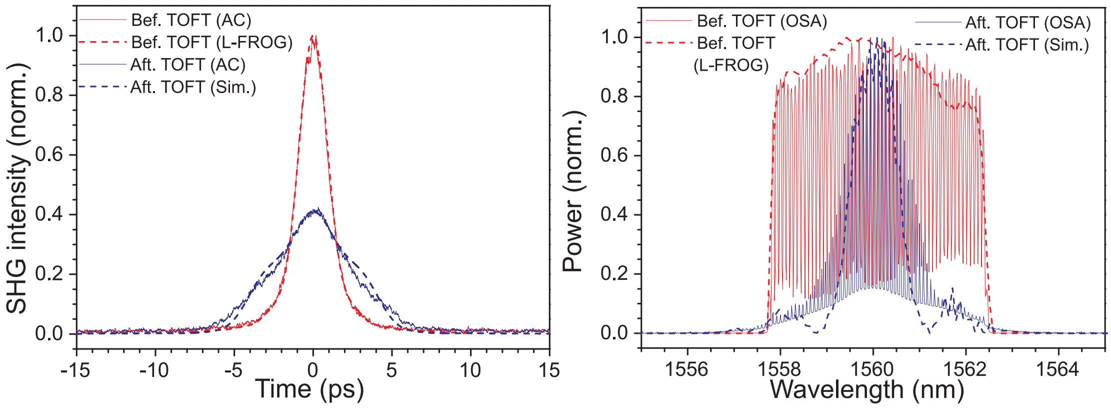

(a) **(b)**

FIGURE 7.18: (a) Autocorrelation and (b) spectral traces of the test signal before (red) and after (blue) TOFT. The simulated traces are shown with dotted lines.

especially in the spectrum where the simulated trace is narrower than the measured one and the side lobes of the sinc shape are more prominent in the simulated spectrum than the measured one.

This may seem to challenge our claim that only by adding a pre-dispersion can a complete and true OFT be obtained. However, Fig. 7.19 shows that *without* the pre-dispersion the residual phase term leaves the signal spectrum relatively square in shape, very unlike its Fourier transform and much more like the original input spectrum. By contrast, although the signal spectrum obtained when a pre-dispersion is used is lacking in some definition, it is distinctively sinc-like in shape with evidence of side lobes. In the time domain, a triangular autocorrelation is obtained in both cases since the accurate transformation in this domain is determined by the post-dispersion which is unchanged.

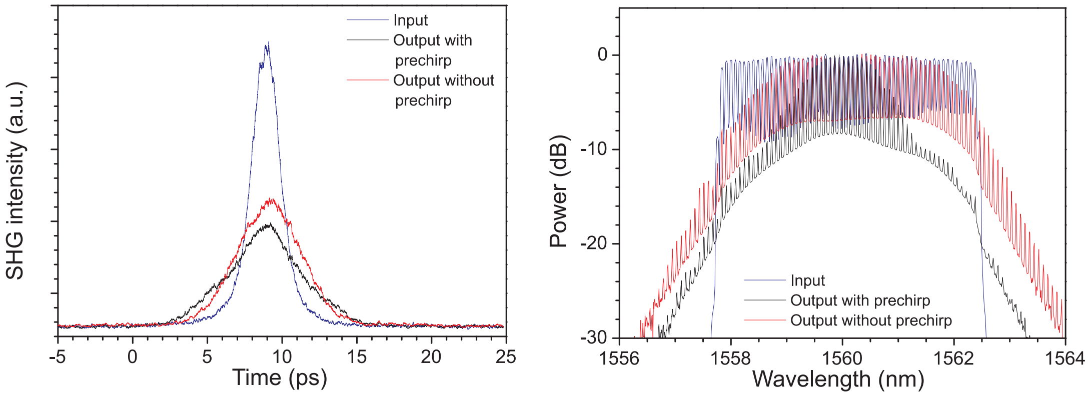

(a) **(b)**

FIGURE 7.19: The (a) autocorrelation and (b) spectral traces of the sinc pulse before the OFT (blue), after the OFT when there is no pre-dispersion used (red) and after the OFT when the pre-dispersion equals the post-dispersion (black)

7.4 Discussion and Conclusions

In this chapter we have re-evaluated the TOFTs we were trying to perform in the previous chapters and sought to understand their shortcomings. The most significant outcome of our investigations was to find that the extra phase term originally noted in Eqn. 2.22, is too large to be neglected by increasing K. Instead this term can be completely negated through the use of a pre-dispersion satisfying the condition $\xi_0 = 1/K$.

In addition, we have identified through numerical simulation the limitations and drawbacks of using XPM with parabolic pulses generally, as a method of implementing a time lens. The two main issues we identified related to the generation of high fidelity parabolic pulses and the nonlinear side effects associated with using XPM. In order to reduce side effects such as SPM of the pump, dark parabolic pulses were used with which we experienced difficulties in generation. However, high fidelity dark parabolic pulses which utilize the entire bit slot have been successfully generated by Hirooka *et al.* by employing line-by-line spectral shaping [3]. Furthermore, these dark parabolic pulses have recently been demonstrated in a TOD compensating TOFT setup which did *not* use a pre-dispersion or consider the spectral domain [4]. Nevertheless, these reports indicate that achievement of the complete TOFT could be potentially improved and demonstrated to even higher fidelity with the use of high resolution spectral shapers.

Despite the limitations, we have demonstrated experimentally that a complete TOFT between the temporal and spectral domains can be achieved by using the matching dispersions around the time lens. Further, the matching condition has been verified in simulation and experimentally by studying the behaviour of the pulses when there is a dispersive offset.

Bibliography

[1] E. Kreyszig. *Advanced Engineering Mathematics.* John Wiley and Sons, 8th edition, 1999.

[2] M. Nakazawa. New frontiers in optical communication: Ultrahigh-speed transmission and coherent transmission. In *3rd International Symposium on Ultrafast Photonic Technologies*, pages 3–6, Cambridge, USA, 2007.

[3] T. Hirooka, M. Nakazawa, and K. Okamoto. Bright and dark 40 GHz parabolic pulse generation using a picosecond optical pulse train and arrayed waveguide grating. *Optics Letters*, 33(10):1102–1104, 2008.

[4] T. Hirooka and M. Nakazawa. All-Optical 40-GHz Time-Domain Fourier Transformation Using XPM With a Dark Parabolic Pulse. *IEEE Photonics Technology Letters*, 20(22):1869–1871, 2008.

Chapter 8

Conclusions and Future Work

This thesis has explored the connections between the temporal and spectral profiles of optical telecommunications signals. In particular, it has focussed on using TOFTs to transfer signal profiles between the temporal and spectral domains, which has potential applications in all-optical signal processing. The work presented in this thesis has contributed to the development of the TOFTs by both increasing the understanding of the conditions enabling TOFT and exploring new methods of obtaining TOFTs in practice.

We started the investigation by reviewing the concept of space-time duality on which our understanding of TOFTs is based. The application of a quadratic phase shift and a matched dispersion is shown to produce a scaled Fourier transform of the signal waveform with an additional phase term. The many ways that a TOFT and more specifically a time lens could be implemented were reviewed leading to a description of our intended method of time lensing. This work has been novel in using XPM with a parabolic pulse to induce the quadratic phase shift needed for time lensing and we have described and demonstrated many ways in which this can be achieved.

To aid our understanding of the domain transformations and of the many irregular signals we have encountered in the course of the thesis, Chapter 3 presented some different techniques to obtain full pulse characterisations. The L-FROG technique in particular was described which has been the most important diagnostic tool in this thesis. The capabilities of the L-FROG technique were demonstrated in the characterisation of pulses from two sample experiments. In the first experiment, pulses were compressed by using SPM to increase their bandwidth and then compressed using matched dispersion. The 402 fs output pulse and its wide bandwidth demonstrated the advantages of using a

Mach-Zehnder modulator as the gating element in the L-FROG as opposed to the narrower bandwidth electro-absorption modulator. In the second experiment, the L-FROG was demonstrated to be suitable for characterising responses of active devices such as an SOA-based wavelength converter. Measuring the output of a CW probe into the device, the L-FROG showed that it could be flexibly configured to measuring the dark pulses carved into the CW probe.

Having established the theory and our diagnostic tools, we designed the first TOFT experiment. In this experiment we generated parabolic pulses by taking advantage of their natural evolution in normally dispersive fibre. With the correct balance of input power, nonlinearity and dispersion, we were able to propagate Gaussian pulses in DCF and extract them at a point when they had evolved into a parabolic shape. In a second stage, the parabolic pulses were simultaneously maintained and underwent XPM with signal pulses to impart a quadratic phase shift onto them, thus achieving time lensing. The TOFT achieved in this experiment was applied to the compensation of timing jitter on a 4x10 Gb/s test signal and demonstrated that it significantly improved the jitter of the channel on which it was applied.

In a second experiment, we addressed the practical difficulties of using nonlinear effects to both generate parabolic pulses and use them for time lensing by employing SSFBGs. A SSFBG designed to spectrally filter 2 ps sech^2 pulses into 10 ps parabolic pulses was used to linearly obtain the required pump. This enabled greater control of the pump power and thus the TOFT conditions. The SSFBG-carved parabolic pulses successfully demonstrated time lensing in a TOFT setup applied to the compensation of second and third order dispersion.

Despite the success of the first two experiments in achieving compensation, it was noted that the pulses were not transforming as we initially expected in the spectral domain. This was addressed by re-analyzing the governing TOFT equations. We found that an additional length of dispersion was required before the time lens to ensure correct transformation in the spectral domain also. This improved theory was analyzed by simulating the effect of perturbations to the ideal amount of dispersion before and after the time lens. We sought to further verify the improved theory through a final TOFT experiment.

With the final experiment we used not only an improved theory, but also an improved implementation of the TOFT. A new pulse source was used which exhibited an extremely wide and stable frequency comb, particularly suitable for spectral carving. Employed in conjunction with reconfigurable filters, we were able to simultaneously generate both a dark parabolic pump pulse and a test signal from the same source. Using wide dark parabolic pulses which exhibit less SPM than bright parabolics and high quality short Gaussian signals, we vastly improved the confinement and quality of the TOFT experiment. We successfully verified the improved theory and demonstrated the improvement by performing a TOFT of a square spectrum.

Having explored and developed several ways of achieving TOFTs using XPM with parabolic pulses, we should consider the applicability of the technique to real systems. First, we note that the setup must neccessrily be altered from the proof-of-principle configuration presented in this thesis, to one which is able to process separately generated incoming signals. Without the close control we've had on the signals in experiment, a real configuration would require clock recovery to enable synchronisation of the signal with a local pump source and demultiplexing of WDM signals (since this is a single channel technique).

Improved parabolic generation encasing the entirety of the signal bit slot (as demonstrated in [1]) would also be neccessary in a real system if demultiplexing of OTDM signals is to be avoided. Even if a full bit slot parabolic could be used, the TOFT technique is ultimately limited by its time domain implementation. We have seen throughout the thesis that leakage of the signal beyond the time lensing window leadds to distortions and side lobes in the output signal. While this fundamentally limits the attainment of an ideal TOFT, it is yet to be determined the extent of which this would limit its use for telecoms signal regeneration. In fact, Okazaki *et al.* have already demonstrated that a perfect TOFT is not required for the technique to achieve significant BER improvement to signals in a real transmissions link [2]. Furthermore, they have shown that even with a sinusoidal phase modulator (signal was temporally demultiplexed), advanced phase modulation formats such as DPSK can also benefit from TOFT regeneration [3, 4].

Consequently, it is likely that for signal regeneration in future telecommunications networks, the greater fidelity of complete TOFTs using XPM would be outweighed by the lower cost and simplicity of TOFT schemes using phase modulators. Instead, XPM-based complete TOFT schemes could prove more valuable in other applications such as signal characterisation or signal pre-conditioning processes (e.g. packet compression) where the preservation of signal phase is important.

Future Work

Implementation of time lenses

The method of implementation of time lenses is critical to the quality of a TOFT device. The work presented in this thesis was novel in its use of XPM with parabolic pulses as a time lens. However, the parabolic pulses presented here were not wide or sharp enough to extend across an entire bit slot, thus limiting the potential transform window of the device. Dark parabolic pulses which occupy entire bit slots have been presented in [1] and demonstrated to achieve TOD compensation in a TOFT configuration in [5]. The use of these pulses with our improved theory would yield further improvement in TOFTs.

We should not forget that there are many other implementations of time lenses which do not use XPM. The FWM implementation described in Section 2.3.3 is particularly interesting since it requires relatively low powers thus reducing nonlinear effects such as SPM which have caused significant challenges with the XPM method. The main drawback of the FWM method was the strongly chirped Gaussian pump it used which reduced the duty cycle of the transform window. This could be potentially alleviated by using the WaveShaper (presented in Chapter 6) to create a pump which is still strongly chirped, but has a flatter intensity profile thus increasing its potential transform window.

Regeneration of Telecommunications Signals

Beyond the development of a XPM based TOFT device, the original aim of this body of work was to create a signal regenerator suitable for use in telecommunications. In Chapters 4 and 5 we demonstrated the ability of our TOFT device to compensate for timing jitter, second and third order dispersions respectively. While we were able to artificially introduce the impairments and observe their compensation using a range of diagnostics, the true test of a regenerator would be to test it in a transmission experiment. That is, the signal would be allowed to develop impairments naturally through propagation in a real fibre link or a recirculating loop. Regeneration by the TOFT and subsequent bit-error-rate testing after various transmission lengths would then highlight the true capability of the device.

An extension to transmissions testing would be the performance of the TOFT device under leakage conditions. That is, when the level of distortion in the temporal signal is large enough to cause it to extend beyond the transform window. We have so far stated that the technique is only applicable to signal impairments confined within the transform window, since other portions of the pulse extending beyond this would not be correctly transformed. There does exist the possibility however, that a small amount of leakage outside the transform window would translate to amplitude jitter while still allowing the majority of the pulse to be regenerated. Further investigations into the amount of tolerable leakage would determine the point at which the introduced jitter outweighs the regenerating action. In addition, it is possible that the combination of a TOFT compensator with an all-optical step-function regenerator (such as the one presented in [6]) could enable the compensation of signals suffering severe inter-symbol interference.

Bibliography

[1] T. Hirooka, M. Nakazawa, and K. Okamoto. Bright and dark 40 GHz parabolic pulse generation using a picosecond optical pulse train and arrayed waveguide grating. *Optics Letters*, 33(10):1102–1104, 2008.

[2] M. Okazaki, Guan Pengyu, T. Hirooka, M. Nakazawa, and T. Miyazaki. 160-Gb/s 200-km Field Transmission Experiment With Large PMD Using a Time-Domain Optical Fourier Transformation Technique. *Photonics Technology Letters, IEEE*, 20 (24):2192–2194, 2008.

[3] T. Hirooka, M. Okazaki, and M. Nakazawa. A Straight-Line 160-Gb/s DPSK Transmission Over 1000 km With Time-Domain Optical Fourier Transformation. *IEEE Photonics Technology Letters*, 20(13):1094–1096, 2008.

[4] T. Hirooka, M. Okazaki, P. Guan, and M. Nakazawa. 320-Gb/s Single-Polarization DPSK Transmission Over 525 km Using Time-Domain Optical Fourier Transformation. *IEEE Photonics Technology Letters*, 20(22):1872–1874, 2008.

[5] T. Hirooka and M. Nakazawa. All-Optical 40-GHz Time-Domain Fourier Transformation Using XPM With a Dark Parabolic Pulse. *IEEE Photonics Technology Letters*, 20(22):1869–1871, 2008.

[6] E. Ciaramella and S. Trillo. All-optical signal rechaping via four-wave mixing in optical fibres. *IEEE Photonics Technology Letters*, 12(7):849–851, 2000.

Appendix A

The DFB Gain-Switched Laser

Gain switched lasers (GSL) have been used in many parts of this thesis as picosecond pulse sources. The main laser diode modules we used were KELD(1552)SSC distributed feedback (DFB) semiconductor lasers available from NEL at a series of wavelengths across the C-band. This appendix describes the basic operation of these useful and compact sources.

The semiconductor laser is initially biased just below threshold giving a low photon density as shown in Fig. A.1 [1]. When a high current is then applied to the device, the carrier density increases and exceeds the lasing threshold level. Through stimulated emission, a large number of photons are generated. During this process, the carrier density is rapidly depleted. The lasing is halted when the carrier density falls back to below threshold. If the injection current is reduced to a low level before threshold is reached again, thus preventing the relaxation oscillations from inducing further lasing, this process produces a single pulse which is much shorter than the electrical driving pulse.

Due to the random nature of spontaneous emission, from which the pulse develops, the timing jitter between the pulses can be very high. However, when the pulse is forced to develop in a stimulated way, e.g. by seeding it with a continuous wave source, such as a CW laser, with better defined optical phase properties, this timing jitter can be reduced by about 60% [2]. This process is called external seeding. The external seed can be injected into the DFB laser, using an optical circulator. Varying the seeding power and polarisation affects the pulse length and the suppression of side modes, as does the wavelength separation between the centre wavelength of the diode and the seed wavelength. There is trade off between obtaining short pulses and reducing the side modes which is influenced by these parameters, such that pulse widths were limited to ~ 7 ps for good quality Gaussians from our GSLs.

Direct intensity modulation of semiconductor lasers is also accompanied by phase modulation, due to changes in the carrier densities and resultant changes in the refractive index of the cavity. This means that the pulses generated by gain switching a semiconductor laser carry a considerable amount of chirp. The down-chirp (i.e. the instantaneous frequency of the pulse reduces over time) observed on gain switched laser pulses is close to linear, with the carrier density quickly reducing at the moment of pulse generation. Linear chirp can be compensated through propagation in dispersive fibre, or with linearly chirped gratings. In the experiments presented in this thesis, suitable lengths of DCF have been used to provide the compensation of this linear chirp. Confirmation of the most optimal DCF length for correct compensation was frequently confirmed with L-FROG measurements.

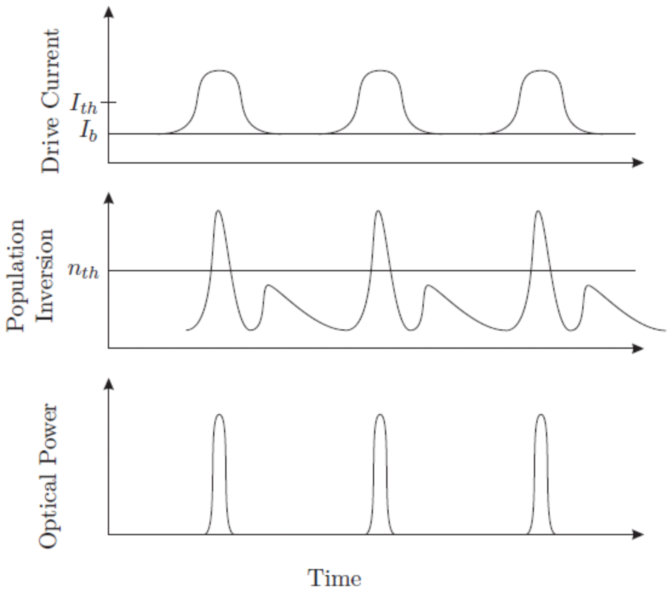

FIGURE A.1: Gain switching laser time characteristics (from [1]).

Bibliography

[1] M. A. F. Roelens. *Precise Intensity and Phase Characterisation of Optical Telecommunication Signals.* PhD thesis, 2006.

[2] D.-S Seo, H.-F. Liu, D. Y. Kim, and D. D. Sampson. Injection power and wavelength dependence of an externally seeded gain-switched Fabry-Perot laser. *Applied Physics Letters*, 67(11):1503–1505, 1995.

List of Publications

Journal papers

- A. Perez, **T.T. Ng**, P. Petropoulos, S. Sales, D.J. Richardson, "Analysis of the dynamic responses of SOA wavelength converters using linear frequency resolved gating technique," IEEE Photonics Technology Letters 20, 1079-1081 (2008).
- **T.T. Ng**, F. Parmigiani, M. Ibsen, Z. Zhang, P. Petropoulos, D.J. Richardson, "Compensation of linear distortions by using XPM with parabolic pulses as a time lens," IEEE Photonics Technology Letters 20, 1097-1099 (2008).
- F. Parmigiani, M. Ibsen, **T.T. Ng**, L. Provost, P. Petropoulos, D.J. Richardson, "An efficient wavelength converter exploiting a grating based saw-tooth pulse shaper," IEEE Photonics Technology Letters 20, 1461-1463 (2008).
- F. Parmigiani, **T.T. Ng**, M. Ibsen, P. Petropoulos and D.J. Richardson, "Timing jitter tolerant all-optical TDM demultiplexing using a saw-tooth pulse shaper," IEEE Photonics Technology Letters 20,1992-1994 (2008)
- N.G.R Broderick and **T.T. Ng**, "Theoretical Study of Noise Reduction of NRZ Signals Using Nonlinear Broken Microcoil Resonators," IEEE Photonics Technology Letters 21, 444-446 (2009)

Conference papers

- P. Petropoulos, F. Parmigiani, **T. Ng**, D.J. Richardson, "Linear signal distortion correction using an optical Fourier transform," e-Photon/ONe Workshop, Athens Greece September (2006).
- **T.T. Ng**, F. Parmigiani, M. Ibsen, Z. Zhang, P. Petropoulos and D.J. Richardson, "Linear-Distortion Compensation Using XPM with Parabolic Pulses," Optical Fiber Communication Conference (OFC), JWA58, Anaheim USA (2007).

- S. Asimakis, **T. Ng**, M.A.F. Roelens, P. Petropoulos, D.J. Richardson, G. Meloni, A. Bogoni and L. Poti, "Performance evaluation of a compact 10-GHz pulse compressor based on a highly nonlinear bismuth-oxide fibre," Conference on Lasers and Electro-optics (CLEO Europe), CI6-4, Munich Germany (2007).
- **T.T. Ng**, A. Perez, S. Sales, D.J. Richardson and P. Petropoulos, "Characterization of XGM and XPM in a SOA-MZI using a linear frequency resolved gating technique," Lasers and Electro-Optics Society (LEOS) Annual Meeting, Florida USA (2007).
- D.J. Richardson, P. Petropoulos, F. Parmigiani, P.J. Almeida, C. Tian, **T.T. Ng**, Z. Zhang and M. Ibsen, "Advances in fibre based pulse shaping technology and its applications in optical communications" Invited paper, International Conference on Transparent Optical Networks (ICTON), We.B2.5, Rome Italy (2007)
- **T.T. Ng**, S. Liu, P. Petropoulos, D.J. Richardson, "A filtered optical frequency comb generator as a stable and tunable short pulse source," European Conference on Optical Communications (ECOC), Tu.3.D.2, Brussels Belgium (2008).
- F. Parmigiani, **T.T. Ng**, M. Ibsen, P. Petropoulos, D.J. Richardson, "Timing jitter tolerant OTDM demultiplexing using a saw-tooth pulse shaper," European Conference on Optical Communications (ECOC), Tu.4.B.5, Brussels Belgium (2008).
- F. Parmigiani, P. Petropoulos, M. Ibsen, **T.T. Ng**, D.J. Richardson, "OTDM add-drop multiplexer using a saw-tooth pulse shaper," Postdeadline paper, European Conference on Optical Communications (ECOC), Th.3.C.4, Brussels Belgium (2008).
- A. van Brakel, C.M. Jauregui, **T.T. Ng**, P. Petropoulos, J.P. Dakin, C. Grivas, M.N. Petrovich and D.J. Richardson, "Cavity ring-down in a photonic bandgap fiber gas cell," Conference on Lasers and Electro-optics (CLEO), CThEE4, San Jose USA (2008).
- F. Parmigiani, M. Ibsen, **T.T. Ng**, L. Provost, P. Petropoulos, D.J. Richardson, "Efficient wavelength conversion using triangular pulses generated using a superstructured fiber Bragg grating," Optical Fiber Communication Conference (OFC), OMP3, San Diego USA (2008)

- P. Petropoulos, F. Parmigiani, **T.T. Ng**, M. Ibsen, D.J. Richardson, ”Advanced optical processing systems combining linear pulse shapers and fibre-based nonlinear switches,” Invited paper, Photonics in Switching, D-03-2, Sapporo Japan (2008)
- P. Petropoulos, F. Parmigiani, **T.T. Ng**, M. Ibsen, D.J. Richardson, ”Applications of superstructured fibre Bragg gratings in optical switching devices,” Invited paper, International Conference on Transparent Optical Networks (ICTON), Tu.D1.4, Athens Greece (2008)
- S. Liu, **T.T. Ng**, D.J. Richardson and P. Petropoulos, ”An optical frequency comb generator as a broadband pulse source,” Optical Fiber Communication Conference (OFC), OThG7, San Diego USA (2009)
- **T.T. Ng**, P. Petropoulos, F. Parmigiani and D.J. Richardson, ”Complete Temporal Optical Fourier Transformations Using Dark Parabolic Pulses,”European Conference on Optical Communications (ECOC), Vienna Austria (2009)